Measurement of muon antineutrino disappearance in the T2K Experiment

by

Jordan William Myslik
Honours Bachelor of Science, University of Toronto, 2008

A Dissertation Submitted in Partial Fulfillment of the
Requirements for the Degree of

DOCTOR OF PHILOSOPHY

in the Department of Physics and Astronomy

Measurement of muon antineutrino disappearance in the T2K Experiment

by

Jordan William Myslik
Honours Bachelor of Science, University of Toronto, 2008

Supervisory Committee

Dr. Dean Karlen, Supervisor
(Department of Physics and Astronomy)

Dr. J. Michael Roney, Departmental Member
(Department of Physics and Astronomy)

Dr. Henning Struchtrup, Outside Member
(Department of Mechanical Engineering)

Supervisory Committee

Dr. Dean Karlen, Supervisor
(Department of Physics and Astronomy)

Dr. J. Michael Roney, Departmental Member
(Department of Physics and Astronomy)

Dr. Henning Struchtrup, Outside Member
(Department of Mechanical Engineering)

ABSTRACT

The T2K ("Tokai-to-Kamioka") Experiment is a long-baseline neutrino oscillation experiment. A beam of primarily muon neutrinos (in neutrino beam mode) or antineutrinos (in antineutrino beam mode) is produced at the J-PARC ("Japan Proton Accelerator Research Complex") facility. The near detector (ND280), located 280 m from the proton beam target, measures a large event rate of neutrino interactions in the unoscillated beam, while the far detector, Super-Kamiokande, 295 km away, searches for the signatures of neutrino oscillation. This dissertation describes the analyses of data at ND280 and Super-Kamiokande leading to T2K's first results from running in antineutrino beam mode: a measurement of muon antineutrino disappearance. The measured values of the antineutrino oscillation parameters (Normal Hierarchy) are $(\sin^2(\bar{\theta}_{23}), |\Delta\bar{m}^2_{32}|) = (0.450, 2.518 \times 10^{-3}\ \mathrm{eV}^2/\mathrm{c}^4)$, with 90% 1D confidence intervals $0.327 < \sin^2(\bar{\theta}_{23}) < 0.692$ and $2.03 \times 10^{-3}\ \mathrm{eV}^2/\mathrm{c}^4 < |\Delta\bar{m}^2_{32}| < 2.92 \times 10^{-3}\ \mathrm{eV}^2/\mathrm{c}^4$. These results are consistent with past measurements of these parameters by other experiments, and with T2K's past measurements of muon neutrinos.

Contents

List of Tables

List of Figures

CONTRIBUTIONS

My studies began with work on the Gas Handling System for the Time Projection Chambers (TPCs) at TRIUMF. I made code and wiring contributions to the control system in relation to the Mass Flow Controllers and Meters, and helped with the testing of the Gas Handling System as a whole prior to shipping it to Japan. Once in Japan, I contributed to the installation and testing of the Gas Handling System, ultimately taking overall responsibility for ensuring stable day-to-day operations. This included making hardware and software changes to any part of the system as needed, recommissioning the system after shutdown periods, writing documentation, providing training to collaborators, and keeping watch remotely. I retained this responsibility for most of my studies.

My physics analysis work was centred around ND280. It began with the assessment of the systematic uncertainty due to pion reinteractions at ND280. This included the extraction of cross sections for the various interaction processes from Geant4, as well as developing and testing the method for identifying these interactions and reweighting events according to the differences between external data and the simulation, and on the uncertainty in the external data. This is described in Section 5.4.16. I documented this approach in multiple technical notes, contributed the code necessary to evaluate this systematic uncertainty to the analysis software package used at ND280, and updated it as needs changed.

From there I moved on to work on using ND280 data in neutrino oscillation analyses. This is done through measuring flux and cross section model parameters relevant to Super-Kamiokande using ND280. I built off of the existing purpose-built code base for the previous analysis to develop a more modular framework that was flexible enough to use for my analysis and be easily adapted to future analyses. I optimized the resulting software package in processor and memory use. It is with this software package that I performed the first analysis of ND280 data from both beam modes, measuring neutrino beam flux and neutrino cross section model parameters. This analysis is described in Chapter 6. Its results were used in T2K's first oscillation analyses using antineutrino beam mode data. One oscillation analysis using the results of my analysis was a muon antineutrino disappearance analysis. Although not performed by me, it is reported here for completeness. It is described in Chapter 7.

ACKNOWLEDGEMENTS

Over the course of my graduate studies, it has been a privilege to perform my research at TRIUMF, the University of Victoria, and J-PARC. At each of these institutions, the many forms of support provided by their people helps to create an environment for great physics, which I deeply appreciate. My research was performed in the greater context of the T2K collaboration. It was truly a pleasure to contribute to the greater goals of the collaboration, and I am indebted to my collaborators for their contributions, which made my work possible. In all of the above, I am grateful to have had the chance to work with and befriend so many highly skilled, passionate, and supportive people. They helped to shape me both professionally and personally, and to all of them I give my heartfelt thanks.

In particular, I would like to thank my supervisor Dean Karlen for his patient guidance and support. Our conversations at critical times provided me with helpful new perspectives, and guided me away from any misconceptions and towards a better understanding. He has also driven an appreciation for the importance of precision in communication. He provided a supportive environment and encouraged me to act independently, and I am very grateful for how I have grown as a result.

When I first arrived at the University of Victoria, the T2K group also contained fellow graduate students Casey Bojechko and André Gaudin. The journey beginning with their warm welcome later evolved into many months as roommates in Minouchi B1, and subsequently some time as officemates back in Victoria. I greatly valued their support and friendship as we navigated through our respective hardware, software, and analysis tasks, and cherish the memories of our time together.

Also at the University of Victoria was T2K postdoc Anthony Hillairet. His wealth of practical experience and his infectious enthusiasm were both very helpful in propelling my work forward. I especially appreciated our regular conversations, which provided many opportunities to discuss directions to explore, and to vent frustrations.

The Gas Handling System was the product of the work of many people. I very much enjoyed my time working with and learning from them, and am grateful for how their skill and attention to detail produced such a robust result. In particular, I would like to thank Dave Morris for getting me started in Trailer Gg and supporting my work with the PLC code for the Mass Flow Controllers/Meters and their wiring. I also worked closely with Mike Le Ross, who taught me much of what I know about coding, wiring, and troubleshooting the PLC and the EPICS interface to it, and

provided support as needed. Finally, I would like to thank Robert Openshaw, the designer of the Gas Handling System. His deep knowledge and passion made for an excellent introduction to this system, and ultimately rubbed off on me. His willingness to explain the system and his reasoning behind it as many times as needed truly made this complex system accessible. I really enjoyed working with him in the later phases of design, through testing and commissioning in Japan. I learned a lot from him, and I am especially thankful that as time went on, Robert continued to provide his expertise, guidance, and mentorship. He struck the perfect balance between ensuring that the Gas Handling System functioned as he intended, and giving me the opportunity to learn, contribute, and take the reins, ensuring that I developed into an expert who could act independently with confidence.

Once installed and running in Japan, fulfilling my Gas Handling System responsibilities was made much easier through the help of multiple people. I am grateful for the work of Kenji Hamano and Toshifumi Tsukamoto in interfacing with various suppliers and contractors in Japan. Their involvement ensured that a language barrier was not a concern, making it much easier to manage operations. When the experiment's schedule meant that staffing in Tokai was at a minimum, I am glad that I could always count on Nick Hastings to take care of matters, ranging from routine manipulations to more involved interventions. Finally, Yevgeniy Petrov's diligent efforts to learn about the Gas Handling System and contribute to its operation and documentation were much appreciated, and gave me confidence that the Gas Handling System was in good hands as I moved on.

My work on the pion reinteraction systematic benefitted greatly from the past work on pion interactions done by Kei Ieki and Patrick de Perio. Their experience proved helpful in enabling my work, and having the world knowledge on the relevant pion interactions readily available made it much easier for my work to proceed. As my work was underway, the guidance and support of Mike Wilking helped me to develop along with this work, and his provision of celebratory Salty Dogs was always appreciated.

To perform my analysis of ND280 data, I began by building off of the prior work of Mark Hartz. His deep expertise and patient guidance and support were instrumental in ensuring the completion of my analysis to the satisfaction of the T2K collaboration, and that I learned a lot in the process. In addition to Mark Hartz, I would like to thank my remaining fellow BANFF group members, Mark Scott, Asher Kaboth, and Christine Nielsen. Whether they were working hard on the inputs I needed, delving

into debugging, taking on tasks in communicating this analysis, or providing guidance and support, I greatly appreciated all of their contributions, and enjoyed working with them.

I am deeply grateful for the mentorship provided by Kendall Mahn in all of my work. Throughout working together on Gas Handling System procedures in the Gas Shack, getting me out of the Gas Shack and into pion reinteractions, and progressing into analysis of ND280 data, Kendall's constant support and guidance pushed me to continue progressing, and taught me much about how to be an effective experimental particle physicist. Her help navigating life in Japan always made for an enjoyable time there, and on that note, I particularly appreciated her valiant effort in ensuring my belongings made it to the airport at the end of my long term stay.

Much of my work was carried out in my office in the basement of the Elliott Building at the University of Victoria. I therefore am thankful for the friendship and support of my officemates Alex Beaulieu, Sam de Jong, and Masaki Uchida, whose bright presence more than made up for our office's lack of window. Venturing above ground, I also found support in the occasional conversation with Alison Elliot and Tony Kwan. I am grateful that all of these friendships (and those with many others in the department) extended outside the office as well, often providing a welcome escape from work and enriching my life in general.

On that note, I must also acknowledge my friend Cuong Le. Whether in person or remotely, one-on-one or through his group gatherings, I have valued his support while I was focussing on work, and his impact on making life outside of work more fun (and filled with delicious food!). And last but not least, my friends outside Victoria, Ben Merotto and Patrick Robinson. Although distance rendered our friendships mostly text-based, I always appreciated having them as sounding boards, and valued the perspectives they provided as friends who knew me in a different context.

This research was enabled in part by support provided by WestGrid (www.westgrid.ca) and Compute Canada Calcul Canada (www.computecanada.ca).

Computations were performed on the GPC supercomputer at the SciNet HPC Consortium [74]. SciNet is funded by: the Canadian Foundation for Innovation under the auspices of Compute Canada; the Government of Ontario; Ontario Research Fund - Research Excellence; and the University of Toronto.

DEDICATION

To my family, friends, and collaborators, whose many different forms of support made this work possible.

Chapter 1

Introduction

The measurement of muon antineutrino disappearance in the T2K ("Tokai-to-Kamioka") Experiment is built upon a long history of research into the neutrino, spanning much of the development of our current understanding of particle physics. In Chapter 2, an overview of this history is given, including the observed anomalies that were the first experimental indications of neutrino oscillation. Subsequently, the interaction of neutrinos with matter is discussed in more detail, the Quantum Mechanical formalism behind neutrino oscillation is introduced, and the current status of the field is summarized.

In Chapter 3, the experimental apparatus of T2K is described, including the proton accelerators of J-PARC and the neutrino beamline, the near detector ND280, and the far detector Super-Kamiokande. This is followed by a more detailed discussion in Chapter 4 of the operating principles and subsystems of the TPCs (Time Projection Chambers), a crucial subdetector of ND280.

With the experimental apparatus sufficiently well described, Chapter 5 details the selection of neutrino and antineutrino interactions for study at ND280. It also describes the sources of systematic uncertainty in the model of the detector, and how they are modelled. How this ND280 data is used to measure neutrino beam flux and cross section model parameters will be discussed in Chapter 6, and how these model parameters are combined with Super-Kamiokande data to perform the measurement of muon antineutrino disappearance will be discussed in Chapter 7. This dissertation concludes in Chapter 8.

There is a quick note to make on terminology. Neutrinos and antineutrinos are often referred to collectively as neutrinos. This dissertation uses this convention, making a distinction between neutrinos and antineutrinos as needed.

Chapter 2

Neutrino Physics

From their first postulation to explain a dramatic difference between theory and experimental observations, neutrinos have provided many mysteries for experimentalists to probe. This chapter reviews the history of neutrinos and neutrino oscillation to present day, along with the mathematical formalism describing it. It also describes the interactions of neutrinos with matter, and the various complications that arise in nuclei with more than one nucleon.

2.1 A brief history of neutrinos

2.1.1 How do you solve a problem like β-decay?

The earliest measurements in particle physics studied radioactivity. One of the radioactive processes was termed "β-decay", due to the outgoing "β-ray" (which we now know as the electron.) Circa 1930, in this process a nucleus A was understood to decay into another nucleus B, as shown in Equation 2.1.

$$\mathrm{A} \rightarrow \mathrm{B} + e^{-} \tag{2.1}$$

However, this theoretical understanding of β-decay had a problem. Conservation of momentum and conservation of energy, two of the basic laws of physics to this day, require that the energy of the outgoing electron be a constant value determined by the masses of A, B, and the electron, as shown in Equation 2.2 [60].

$$E = \left(\frac{m_A^2 - m_B^2 + m_e^2}{2m_A} \right) c^2 \tag{2.2}$$

Instead, the experimental observations of the electron energy provided a broad spectrum of lower energies, as depicted in Figure 2.1. The laws of conservation of momentum and energy had apparently been broken. In 1930, Wolfgang Pauli pro-

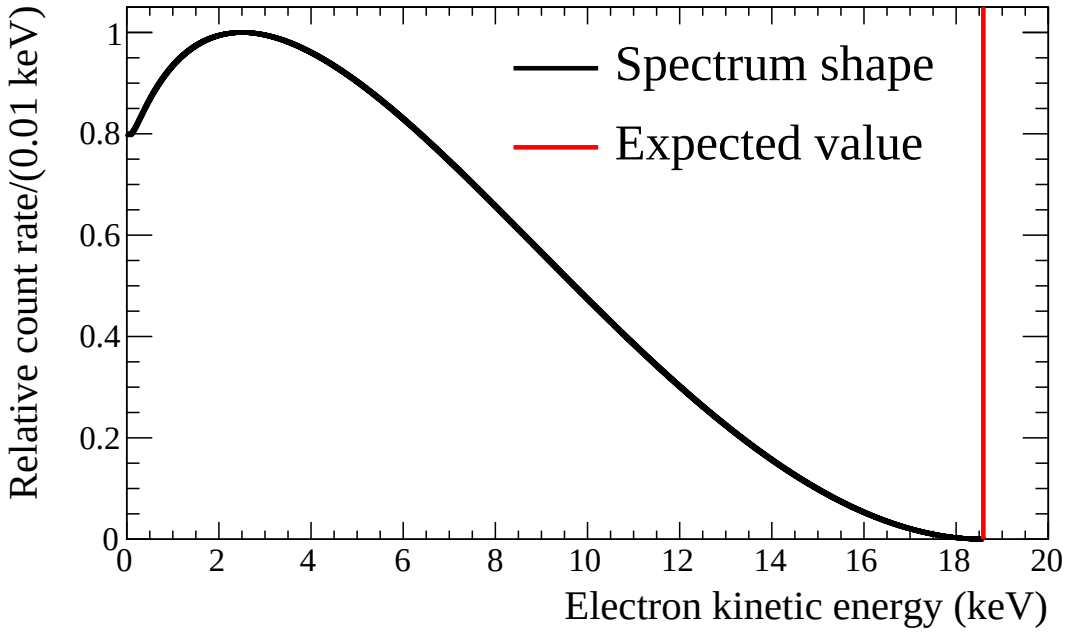

Figure 2.1: The shape of the energy spectrum for the electron from β-decay of tritium ($^3_1$H), compared to the constant value expected for a two-body β-decay as described by Equation 2.1. This plot was generated using equations and information from [72], and information from [83] and [79].

posed that if a light neutral particle were also produced in β-decay, then the observed electron energy spectrum would be consistent with the conservation of momentum and energy. He called this particle the "neutron." The particle we know today as the neutron was discovered in 1932 by Chadwick, and is too massive to be the particle proposed by Pauli. However, in 1933 Enrico Fermi presented a new theory of β-decay, successfully incorporating Pauli's neutral particle. Its name is originally attributed to Edoardo Amaldi, during a humourous conversation at the Istituto di Via Panisperna in relation to Pauli's "light neutron". Amaldi made a funny and grammatically incorrect contraction of "little neutron" (*neutronino*) to devise the term "neutrino", which Fermi went on to popularize internationally (see note 277 of [19]). Fermi's theory with the neutrino, denoted by the Greek letter ν, gave the description of β-decay shown in Equation 2.3, (where the neutron n is confined in the nucleus A, and the proton p is

confined in the nucleus B) which is close to our current understanding of the process (though further advances in particle physics change the picture somewhat, as will be described later in this section.)

$$n \rightarrow p + e^{-} + \nu \tag{2.3}$$

2.1.2 More evidence from cosmic rays

An additional source of radioactivity that made up some of the earliest particle physics measurements are cosmic rays. Today, cosmic rays are understood to be high energy charged particles, originating in astrophysical processes outside the solar system. These can range from protons (the most common) to larger ions. The cosmic rays interact with molecules in the upper atmosphere, producing showers of secondary particles. Some of these particles (or their decay products) make it down to produce the studied source of radioactivity at ground level, with more radioactivity observed at higher altitudes.

Since cosmic ray muons can reach ground-level, the muon had been well-studied. As in β-decay, its decay did not produce a monoenergetic electron, so more than one additional neutral particle had to be involved in the decay. Muon decay was therefore thought to proceed by the process shown in Equation 2.4.

$$\mu \rightarrow e + 2\nu \tag{2.4}$$

In the late 1940s, C.F. Powell performed an experiment on a mountaintop, using photographic emulsion to observe the tracks produced by charged particles involved in cosmic ray processes. The ionization produced by the charged particle would expose the emulsion along the particle's track. By observing the tracks of the particles, how they interacted in the emulsion, and how they decayed, the nature of cosmic rays could be studied. These observations showed clear evidence for another secondary cosmic ray particle (which we now know as the pion, π), which decays into a muon. Conservation of momentum required that another particle be produced in this decay, which had to be neutral since it did not leave a track in the emulsion. It was thus natural to postulate the π decay given in Equation 2.5.

$$\pi \rightarrow \mu + \nu \tag{2.5}$$

Therefore, by the end of the 1940s, there was increasing theoretical motivation for a ghostly light neutral particle to be produced in decays, be they of the muon, pion, or unstable nuclei. However, in order for the neutrino to be anything more than an interesting idea, it would need to be observed.

2.1.3 Neutrinos, antineutrinos, and the first observation

In 1953, Konopinski and Mahmoud [71] introduced the concept behind what would later be called *lepton number*. Subsequently, the electron, muon, and neutrino were assigned a lepton number of $+1$, and the positron, positive muon, and antineutrino were assigned a lepton number of -1. The requirement that lepton number be conserved in particle interactions meant that the "neutrino" of β-decay was in fact an antineutrino, denoted $\bar{\nu}$. Thus moving the understanding of the β-decay process (Equation 2.3) to that shown in Equation 2.6, which is closer to today's understanding of the process.

$$n \rightarrow p + e^- + \bar{\nu} \tag{2.6}$$

By the 1950s, the neutrino was understood to have a low probability of interaction with matter (a small *cross section*). Therefore, a large detector or an intense source of neutrinos or antineutrinos was required in order to make a statistically significant observation in a timely fashion. At this time, nuclear reactors were available, and were predicted by theorists to be the most intense sources of antineutrinos available. Particle theory also allowed a process called "inverse beta decay", shown in Equation 2.7.

$$\bar{\nu} + p \rightarrow e^+ + n \tag{2.7}$$

Given this information, Reines and Cowan built a detector near the Savannah River nuclear reactor in South Carolina, which provided an antineutrino flux at the detector of $1.2 \times 10^{13}/\mathrm{cm}^2/\mathrm{sec}$ [85]. This detector contained water doped with $CdCl_2$, which was instrumented with scintillator coupled to photomultiplier tubes. (Scintillator and photomultiplier tubes are described in the context of their inclusion in the T2K apparatus in Chapter 3). This experimental setup made them sensitive to light produced inside their detector volume. A neutrino interaction would produce light in their detector in two ways:

1. The positron produced in the neutrino interaction would quickly annihilate with an electron in the water, producing light via $e^+ + e^- \rightarrow 2\gamma$.

2. The neutron produced in the neutrino interaction would capture on a cadmium nucleus, producing an excited state that would decay down through emission of a photon. Using one of the relatively abundant naturally occurring cadmium isotopes as an example, $n + {}^{113}\mathrm{Cd} \rightarrow {}^{114}\mathrm{Cd}^{*} \rightarrow {}^{114}\mathrm{Cd} + \gamma$.

Since neutron capture is a slower process than positron annihilation, this produces a characteristic delayed coincidence signal that the experiment looked for. They ultimately observed 2-3 events per hour when the reactor was running, thus confirming the existence of the neutrino in 1956 [46, 86].

2.1.4 More neutrinos, and detection of the muon and tau neutrinos

Subdivision of lepton number

Alas, the theory of lepton number conservation posed a problem. The reigning idea in particle physics at the time, attributed to Murray Gell-Mann (discussed in the footnote of his 1956 paper [58] on p. 859), was that "anything that is not compulsory is forbidden." Namely, if a process is not observed to occur, it should be forbidden by a conservation law. So although the theory of lepton number explained the observed muon decay of $\mu \rightarrow e + \nu + \bar{\nu}$, it also allowed the decay $\mu \rightarrow e + \gamma$, which has never been observed. The latter process therefore appeared to be forbidden by nature, but was not forbidden by the existing theory of lepton number.

In the late 1950s and early 1960s, the solution to this problem was proposed: to subdivide lepton number amongst the lepton flavours. In this scheme, the electron had a corresponding electron neutrino (both of electron number +1) and the muon had a corresponding muon neutrino (both of muon number +1), with corresponding antimatter particles with opposite sign lepton numbers. Under this theory, $\mu \rightarrow e + \gamma$ is forbidden, as it does not preserve electron number and muon number. Conservation of lepton number gives the observed muon decays of Equation 2.9 and Equation 2.8.

$$\mu^{-} \rightarrow e^{-} + \nu_{\mu} + \bar{\nu}_{e} \tag{2.8}$$

$$\mu^{+} \rightarrow e^{+} + \bar{\nu}_{\mu} + \nu_{e} \tag{2.9}$$

In addition, the pion decays became as shown in Equation 2.10, and Equation 2.11.

$$\pi^+ \rightarrow \mu^+ + \nu_\mu \tag{2.10}$$

$$\pi^- \rightarrow \mu^- + \bar{\nu}_\mu \tag{2.11}$$

Similarly, this brings us to our current understanding of β-decay, shown in Equation 2.12.

$$n \rightarrow p + e^- + \bar{\nu}_e \tag{2.12}$$

Experimental attentions therefore were directed towards testing this theory by determining whether there is in fact a muon neutrino that is different from the electron neutrino, by observing how they interact.

Discovery of the muon neutrino

As discussed in Section 2.1.2, nature already provides a source of muon neutrinos and muon antineutrinos, produced from cosmic rays. However, theoretical predictions and the experience of Reines and Cowan with $\bar{\nu}_e$ established that neutrino cross sections are small. Relying on naturally produced neutrinos for a definitive observation would therefore require a very large detector or a long time period of data collection. In addition, cosmic ray neutrinos would be a mixture of ν_μ, ν_e, $\bar{\nu}_\mu$ and $\bar{\nu}_e$, due to the muon decays, making it difficult to definitively discern whether the neutrinos produced in pion decays are in fact different from the neutrinos observed by Reines and Cowan. Thankfully, cosmic rays could be useful instead as inspiration for producing muon neutrinos and antineutrinos artificially in the lab. By bringing protons up to a sufficient energy in a particle accelerator and colliding them with a target, the lab would contain a situation similar to that in the upper atmosphere with cosmic rays, producing pions that decay into muons and muon neutrinos or antineutrinos.

Lederman, Schwartz, and Steinberger leveraged this technique at Brookhaven National Laboratory. The protons were accelerated up to 15 GeV, and collided with a beryllium target. This produced many $\pi^\pm$, which decayed into muons and muon neutrinos and antineutrinos travelling generally in the beam direction. A further 21 m from the target there was a 13.5 m thick iron shield wall, which would stop the muons, preventing them from traversing the detector. Neutrinos produced in the decays of these stopped muons would not be focussed in the beam direction, therefore resulting in a much lower ν_e and $\bar{\nu}_e$ background compared to cosmic ray neutrinos.

On the other side of the shield wall they used a detector technology called a *spark chamber*. Their design consisted of an array of 10 1 ton modules, each containing 9 parallel aluminum plates, with a large voltage drop between them, separated by a gas. When a charged particle passes through the gas, it ionizes the gas along its track, allowing electricity to flow through along this track, producing a visible spark. A muon could be identified by its ability to travel through several aluminum plates without interacting, while an electron would not. Using this method, the observed neutrino interactions were consistent with the neutrinos produced in pion decays only interacting to produce muons (and not electrons). Therefore, these neutrinos are of a different flavour than those observed by Reines and Cowan. The Lederman, Schwartz, and Steinberger measurement of 1962 thus established the existence of the muon neutrino [49].

Discovery of the tau neutrino

In 1975, Martin Lewis Perl and the SLAC-LBL group discovered [80] a new lepton, the tau, denoted τ. As had been firmly established by this point with the electron and the muon, this created a need for a corresponding tau neutrino, ν_τ.

To observe the ν_τ, the DONUT (Direct Observation of the NU Tau) experiment directed the 800 GeV proton beam of the Tevatron at Fermilab towards a meter long tungsten beam dump, from April to September 1997. This produced tau neutrinos through the production of D_S mesons, which decay via $D_S^+ \rightarrow \tau^+ + \nu_\tau$. A detector was placed 36 m downstream of the beam dump, and was capable of discriminating between taus, muons, and electrons. In their result published in 2001 [70], they analyzed 203 neutrino interactions, and found 4 ν_τ events, with an expected background of 0.34 ± 0.05 events, thus establishing the existence of the tau neutrino.

2.1.5 The picture today

Today, our understanding of particle physics is codified in the *Standard Model*, which describes the set of fundamental particles, and the interactions between them. Up to this point we have introduced the leptons, which are fermions (spin $\frac{1}{2}$) that exist in three flavours: electron (e), muon (μ), and tau (τ), in matter and antimatter, with a charged particle (negative for matter, positive for antimatter) and an associated neutrino (matter) or antineutrino (antimatter). This gives us three neutrinos (ν_e, ν_μ, and ν_τ), and three antineutrinos ($\bar{\nu}_e$, $\bar{\nu}_\mu$, and $\bar{\nu}_\tau$).

In addition, there are the quarks, also fermions, which also exist in 3 generations. The up (u), charm (c), and top (t) quarks have a charge of $+\frac{2}{3}$, while the down (d), strange (s), and bottom (b) quarks have a charge of $-\frac{1}{3}$. The antimatter versions of each of these quarks has the opposite signed charge as its matter counterpart. The up quark (u) and the down quark (d) are of particular importance, as they make up protons (uud) and neutrons (udd), and thus the matter that one encounters in day to day life (and most importantly to the work discussed in this dissertation, in detectors in neutrino oscillation experiments.)

Also important are the gauge bosons, which are vector bosons (spin 1). These act as "force carriers" in the Standard Model. The photon (γ) is responsible for the electromagnetic force (e.g. the force exerted between two electrically charged objects). The strong force (which holds quarks together, forming protons and neutrons for example) is mediated by the gluon, g. The weak force, through which neutrinos interact, is mediated by the $W^{\pm}$ and the Z^0, both of which are described in more detail in Section 2.2.

Finally, there is the Higgs Boson, a scalar boson (spin 0), which is an excitation of the field that gives mass to particles. It has been the subject of considerable experimental activity as of late. With the recent discovery of the Higgs Boson, all of the fundamental particles of the Standard Model have been observed.

There are also three symmetries that are important to consider in relation to Standard Model processes, which are relevant to the study of neutrinos.

1. Charge (C): A process conserves Charge symmetry if swapping matter with antimatter (and vice versa) results in an equivalent process, with identical cross section. The electromagnetic and strong interactions both conserve C.

2. Parity (P): A process conserves Parity symmetry if the transformation $(x, y, z) \rightarrow (-x, -y, -z)$ results in an equivalent process, with identical cross section. The electromagnetic and strong interactions both conserve P.

3. Time (T): An interaction conserves Time symmetry if the reverse process (i.e. backwards in time) also occurs with identical cross section. The electromagnetic and strong interactions both conserve T.

Notably absent from the list of interactions that conserve each of the above symmetries is the weak interaction. For both C and P, the most stark example of their violation is the π^+ decay, $\pi^+ \rightarrow \mu^+ + \nu_\mu$, and the π^- decay, $\pi^- \rightarrow \mu^- + \bar{\nu}_\mu$. An

application of the Charge operator as defined above would appear to convert one to the other, but in fact it misses one important detail: the spin of the neutrino relative to its direction (in the rest frame of the pion). The muon and the neutrino are both spin $\frac{1}{2}$ particles, giving them two possible spin values, $\pm\frac{1}{2}$, or "spin up" and "spin down", where the axis defining "up" and "down" can be chosen arbitarily. However, the pion is a spin 0 particle, thereby constraining the muon and the neutrino to have opposite spins, in order to conserve spin. In addition, the muon and the neutrino must be emitted travelling in opposite directions in the pion's rest frame, in order to conserve momentum. It is therefore natural to define the axis of the spin as the direction each particle is travelling in. If the spin is oriented "up" (in the same direction as the particle is travelling), it is said to be "right-handed", and if the spin is oriented "down" (in the opposite direction as the particle is travelling) it is said to be "left-handed". Should Parity be a conserved symmetry of this interaction, one would expect the neutrino to be left-handed and right-handed an equal amount of the time. However, experiments (e.g. [28, 31]) measuring this property (*helicity*) show a shocking departure from this expectation: the μ^+ (and therefore the ν_μ) is always left-handed, and the μ^- (and therefore the $\bar{\nu}_\mu$) is always right-handed. Since a Charge operation would convert the π^+ decay into a π^- decay with a left-handed $\bar{\nu}_\mu$ (which these results indicate does not to exist), Charge symmetry is also not conserved by this interaction.

With this in mind, one can see, however, that the pion decay does indeed conserve the combined symmetry of C and P, denoted CP. However, CP violation in the weak interaction has been observed (e.g. by [34]), and whether it occurs in neutrino oscillations is currently an open question, as discussed in Section 2.3. CP violation is a way in which nature could prefer matter over antimatter, possibly providing an explanation for the observed matter-antimatter asymmetry of the universe.

A final combined symmetry to consider is that of Charge, Parity, and Time, denoted CPT. The CPT Theorem states that CPT must always be conserved. The requirement that CPT be conserved is fundamental to all of modern physics, to the point where a prominent theorist noted that if a departure is ever found, "all hell breaks loose"(p. 135 of [60]). This is therefore a topic of interest to experimentalists (for example, in [27] and [17]), and the study of neutrino oscillation also provides an opportunity to test the CPT Theorem, as discussed in Section 2.3.

2.2 Neutrino interactions

In the Standard Model of particle physics, neutrinos only interact with matter through the weak force. A weak interaction is mediated by one of two particles:

1. The Z boson: Denoted Z^0, it is a neutral particle with mass 91.1876 ± 0.0021 GeV/c^2 [79]. Interactions mediated by the Z boson are referred to as *Neutral Current* (NC) interactions.

2. The W boson: Is a charged particle, denoted W^+ or W^- depending on its charge, and has mass 80.385 ± 0.015 GeV/c^2 [79]. Interactions mediated by the W boson are referred to as *Charged Current* (CC) interactions.

In Neutral Current interactions, a neutrino or antineutrino of any flavour transfers energy and momentum to a quark or lepton of any flavour via a Z^0, and the original neutrino continues to exist.

Charged Current interactions for neutrinos and antineutrinos in normal matter (i.e. u and d quarks and electrons) at the level of quarks and leptons are shown in Table 2.1.

Neutrinos	Antineutrinos
$\nu_e + e \to \nu_e + e$	$\bar{\nu}_e + e \to \bar{\nu}_e + e$
$\nu_\ell + d \to \ell^- + u$	$\bar{\nu}_\ell + u \to \ell^+ + d$

Table 2.1: Charged Current interactions of neutrinos and antineutrinos with electrons and u and d quarks. ℓ denotes an e, μ, or τ lepton.

Although these are the fundamental interactions allowed by the Standard Model, in reality quarks are not free particles, but are bound in nucleons: the proton (uud) and the neutron (udd). As a result, neutrino and antineutrino interactions with matter are classified into multiple categories. In addition, experiments typically involve nuclei with more than one nucleon. This opens up additional processes, where a neutrino interacts with multiple nucleons, or even the entire nucleus. The interactions relevant to this dissertation are shown in Table 2.2.

Of particular interest is the process called "Charged Current Quasi-Elastic" ("CCQE"). As a Charged Current process, there is an outgoing charged lepton that can be detected and identified in order to determine the neutrino flavour. Even more importantly, the energy of the neutrino that interacted can be calculated (using Equa-

Name	Abbreviation	Neutrinos	Antineutrinos
CC Quasi-Elastic	CCQE	$\nu_\ell + n \to \ell^- + p$	$\bar{\nu}_\ell + p \to \ell^+ + n$
CC 2 particle 2 hole	CC 2p-2h	$\nu_\ell + np \to \ell^- + p + p$	$\bar{\nu}_\ell + np \to \ell^+ + n + n$
CC Resonant Pion Production	CCRES	$\nu_\ell + p \to \ell^- + \Delta^{++} \to \ell^- + p + \pi^+$ $\nu_\ell + n \to \ell^- + \Delta^+ \to \ell^- + p + \pi^0$ $\nu_\ell + n \to \ell^- + \Delta^+ \to \ell^- + n + \pi^+$	$\bar{\nu}_\ell + n \to \ell^+ + \Delta^- \to \ell^+ + n + \pi^-$ $\bar{\nu}_\ell + p \to \ell^+ + \Delta^0 \to \ell^+ + n + \pi^0$ $\bar{\nu}_\ell + p \to \ell^+ + \Delta^0 \to \ell^+ + p + \pi^-$
CC Coherent Pion Production	CCCOH	$\nu_\ell + A \to \ell^- + A + \pi^+$ (where A is a nucleus)	$\bar{\nu}_\ell + A \to \ell^+ + A + \pi^-$ (where A is a nucleus)
CC Other	CC OTHER	$\nu_\ell + (n \text{ or } p) \to \ell^- + (n \text{ or } p) + \text{pions}$	$\bar{\nu}_\ell + (n \text{ or } p) \to \ell^+ + (n \text{ or } p) + \text{pions}$
NC Resonant Pion Production	NCRES	$\nu_\ell + n \to \nu_\ell + \Delta^0 \to \nu_\ell + n + \pi^0$ $\nu_\ell + p \to \nu_\ell + \Delta^+ \to \nu_\ell + p + \pi^0$ $\nu_\ell + n \to \nu_\ell + \Delta^0 \to \nu_\ell + p + \pi^-$ $\nu_\ell + p \to \nu_\ell + \Delta^+ \to \nu_\ell + n + \pi^+$	$\bar{\nu}_\ell + n \to \bar{\nu}_\ell + \Delta^0 \to \bar{\nu}_\ell + n + \pi^0$ $\bar{\nu}_\ell + p \to \bar{\nu}_\ell + \Delta^+ \to \bar{\nu}_\ell + p + \pi^0$ $\bar{\nu}_\ell + n \to \bar{\nu}_\ell + \Delta^0 \to \bar{\nu}_\ell + p + \pi^-$ $\bar{\nu}_\ell + p \to \bar{\nu}_\ell + \Delta^+ \to \bar{\nu}_\ell + n + \pi^+$
NC Other	NC OTHER	$\nu_\ell + (n \text{ or } p) \to \nu_\ell + (n \text{ or } p) + \text{pions}$	$\bar{\nu}_\ell + (n \text{ or } p) \to \bar{\nu}_\ell + (n \text{ or } p) + \text{pions}$

Table 2.2: Interactions of neutrinos and antineutrinos most relevant to the work discussed in this dissertation. ℓ denotes an e, μ, or τ lepton. CC abbreviates "Charged Current" and NC abbreviates "Neutral Current". The "Other" category captures high energy neutrino interactions that produce multiple pions.

tion 2.13) from the momentum of the outgoing lepton, and the angle it made with the path of the neutrino (which for a neutrino beam, for example, is pretty well known.)

$$E_\nu = \frac{m_p^2 - m_n^2 - m_\ell^2 + 2m_n E_\ell}{2(m_n - E_\ell + p_\ell cos\theta_\ell)} \tag{2.13}$$

In addition to the interaction processes on multiple nucleons (CC 2p-2h) or entire nuclei (CCCOH) given in Table 2.2, neutrinos interacting with nucleons within a larger nucleus poses some additional experimental problems. Although outgoing leptons tend to easily escape nuclei without interacting, other particles (protons, neutrons, and pions) may interact inside the nucleus, in a process called a *Final State Interaction* (abbreviated "FSI"). Therefore, the particles leaving the nucleus (i.e. those that an experiment could actually measure) may be different from those produced in the original neutrino interaction. This adds an additional level of difficulty to performing neutrino measurements, as, for example, a CCRES event could be mis-identified as CCQE due to the pion being absorbed in the nucleus. If Equation 2.13 were then used to reconstruct the neutrino energy, the resulting energy would be incorrect, and would distort the reconstructed neutrino energy spectrum. Also problematic is the CC 2p-2h interaction type, which is only distinguishable from CCQE by the kinemetics of the outgoing protons, which are both subject to FSI and not typically observed (sufficiently precisely or at all) at T2K at both ND280 and Super-Kamiokande. The neutrino interaction model therefore plays a crucial role in neutrino experiments, as will be discussed in Chapters 5, 6, and 7.

2.3 Neutrino oscillation

In neutrino oscillation, one flavour of neutrino changes into another flavour of neutrino. This could result in some of the neutrinos having changed to a flavour that an experiment's measurement methods were not sensitive to, and thus fewer neutrinos would be measured than expected (*disappearance*). Alternatively, given a source of one flavour, neutrinos of another flavour can be observed (*appearance*). In this section, the two main discrepancies that motivated neutrino oscillation as a theory are discussed, followed by the mathematical formalism, and finally, the current status of the field.

2.3.1 Motivation

As neutrinos from various sources continued to be studied, discrepancies emerged between the theoretical prediction and the experimentally observed number of neutrinos. The two main discrepancies, *The Solar Neutrino Problem* and *The Atmospheric Neutrino Anomaly* were ultimately explained by the theory of neutrino oscillation. It was for the discovery of neutrino oscillations (which shows that neutrinos have mass) that Takaaki Kajita of Super-Kamiokande and Arthur B. McDonald of the Sudbury Neutrino Observatory (SNO) were awarded the 2015 Nobel Prize in Physics.

The Solar Neutrino Problem

By the mid-1960s, models of the sun had taken shape, supported by experiments investigating the interaction processes expected to occur inside the sun. Since many of these processes involve the production of neutrinos in different energy ranges, studying these solar neutrinos would provide valuable information on the inner workings of the sun. Thus motivated, in 1965-1967 the Homestake solar neutrino experiment [44] was built.

The Homestake experiment was built 1478 m below the surface at the Homestake Gold Mine in Lead, South Dakota. This provided shielding from cosmic ray muons of 4200 ± 100 mwe (metres water equivalent). It consisted of a steel tank containing 615 tonnes of tetrachloroethylene (C_2Cl_4, commonly available as dry cleaning fluid). This design sought to detect neutrinos through the interaction shown in Equation 2.14.

$$\nu_e + {}^{37}\mathrm{Cl} \rightarrow {}^{37}\mathrm{Ar} + e^- \tag{2.14}$$

In order to determine that this interaction occurred, helium gas was bubbled through the tetrachloroethylene, which extracted the gaseous ^{37}Ar. This gas mixture was then passed through an absorber that absorbs the argon but not the helium. ^{37}Ar is radioactive, so the number of decays in the absorber could be counted, and therefore used to determine how many neutrino interactions had taken place in the detector.

In their early result published in 1968 [50], the Homestake experiment expected 2-7 events per day based on solar models, but set an upper limit of 0.5 events per day based on their observations. This was taken, at the time, to be indicative of a problem with the solar model, and a theoretical paper ([29], printed in the same journal issue immediately following the Homestake experimental result) argued that the models could be tweaked sufficiently to bring them into agreement with the Homestake observation.

In the years since the initial Homestake result, the solar model continued to be developed. The Homestake experiment continued to operate until 1994, measuring the flux of solar neutrinos with energies down to 0.814 MeV (the minimum neutrino energy required for the interaction given in Equation 2.14 to occur). By 1978, attempts to reconcile the theoretical solar model predictions with the observations were sufficiently frustrated to coin the term "The Solar Neutrino Problem".

Further experimentation with sensitivity to different neutrino energy regions served to deepen the problem. This came from the 2140 tonne *Water Cherenkov* detector, Kamiokande-II. As described in the description of its successor in Section 3.4, Water Cherenkov detectors instrument a large volume of water with sensitive light sensors, in order to detect light produced by particles travelling faster than light in water. The production of this light is known as the *Cherenkov Effect*. In 1990, Kamiokande-II, observed a neutrino flux that was $0.46 \pm 0.05(stat) \pm 0.06(syst)$ that predicted by the solar model [64]. This measurement was performed using the elastic scattering of electron neutrinos on electrons in the water molecule, shown in Equation 2.15

$$\nu_e + e^- \rightarrow \nu_e + e^- \tag{2.15}$$

This process can occur via both the W boson and the Z boson. It is also possible for the other neutrino flavours to undergo the Z boson mediated version of this process, but this process is dominated by the W boson mediated version, which is exclusive to electron neutrinos. The kinematics of this elastic scattering interaction, when combined with the ability of Kamiokande-II to reconstruct the electron's direction,

provided sufficient information about the direction of the neutrino to confirm that these neutrinos did in fact originate from the sun. The Kamiokande-II observation required that the outgoing electron have a total energy of at least 9.3 MeV in the first run period, and 7.5 MeV in the second (in both cases, primarily in order to distinguish signal from background). This left it only sensitive to solar neutrinos in the highest energy solar neutrino production channels (dominated by $^8\mathrm{B} \rightarrow \mathrm{Be}^* + e^+ + \nu_e$). Although the deficit observed by Kamiokande-II was a confirmation of the deficit observed by Homestake, its size conflicted with the deficit measured at Homestake, when considering the other solar neutrino production channels that Homestake was sensitive to.

Finally, another class of experiments in the early 1990s served to make the problem even more apparent. In order to probe even lower down into the solar neutrino energy spectrum, and be sensitive to the *pp* process ($p+p \rightarrow {}^2\mathrm{H}+e^++\nu_e$), these experiments searched for the inverse beta decay of gallium-71, which has an energy threshold of 0.233 MeV, and is shown in Equation 2.16

$$\nu_e + {}^{71}\mathrm{Ga} \rightarrow {}^{71}\mathrm{Ge} + e^- \tag{2.16}$$

Much like Homestake's observation of the resulting radioactive argon isotope, these experiments relied on counting the decays of the resulting radioactive germanium-71. In the early 1990s, the two main experiments using this technique were the Soviet-American-Gallium-Experiment (SAGE) [1] and the Gallium Experiment (GALLEX) [22]. SAGE was located underground at the Baksan Neutrino Observatory in the Caucasus Mountains of Russia, and GALLEX was located at the *Laboratori Nazionali del Gran Sasso* in Italy. SAGE took advantage of the low melting point of gallium (29.7646°C [88]) to have their detector volume contain 30 tons of liquid gallium, while GALLEX instead employed a concentrated solution of $GaCl_3$ and hydrochloric acid, containing a total of 30.3 t of gallium. Both the SAGE and GALLEX results were consistent with each other, and measured a significantly lower neutrino flux than the Standard Solar Model predicted, but the size of the deficit conflicted with the deficits measured by Kamiokande-II and Homestake when considering the different channels that these experiments were sensitive to.

So, by 1996 the Solar Neutrino Problem had come to a head. Three different experimental methods measuring solar neutrinos produced in different processes in the sun could not be reconciled with the Standard Solar Model and with each other.

The Solar Neutrino Problem was ultimately resolved by adding to the picture measurements by the Sudbury Neutrino Observatory (SNO) [67], a 1 ktonne Water Cherenkov detector, located underground at the 6800 foot level of Sudbury's Creighton Mine, which provided approximately 6000 meters water equivalent shielding from cosmic ray muons. As discussed earlier, Kamiokande-II (and Super-Kamiokande) were restricted to considering only the Elastic Scattering neutrino interaction channel. This was due to their design employing regular "light" water, H_2O. For an electron neutrino to interact via a Charged Current process, the presence of a neutron is required. Normal hydrogen nuclei contain none, ruling them out as a potential target, and although oxygen nuclei contain many neutrons, the interaction $^{16}\mathrm{O}+\nu_e \rightarrow {}^{16}\mathrm{F}+e^-$ has an energy threshold of 15.4 MeV (p. 193 of [82]). This is above the energy of most solar neutrinos, and would be suppressed due to its high energy requirement for the relatively small number of neutrinos above this energy. In addition, the expected maximum energy of solar neutrinos is 18.8 MeV [30]. Therefore, even the most energetic outgoing electrons would still be well below the 7.5 MeV threshold requirement for signal-background discrimination.

The innovative design employed by SNO was the use of Heavy Water, D_2O, where the hydrogen atoms have been replaced by deuterium (pn, denoted d below). This opened up the Charged Current interaction channel in Equation 2.17, and the Neutral Current interaction in Equation 2.18, which require neutrino energies of 1.44 MeV and 2.22 MeV to occur, respectively. However, like Kamiokande-II, SNO analyses also had higher energy thresholds for the reconstructed electron, ranging from 5 MeV to 6 MeV, in order to distinguish signal from background.

$$\nu_e + d \rightarrow p + p + e^- \tag{2.17}$$

$$\nu_x + d \rightarrow p + n + \nu_x \tag{2.18}$$

So, there were the following possible interactions in SNO:

- Elastic Scattering (ES): Shared with Kamiokande-II and later Super-Kamiokande, this interaction is dominated by electron neutrinos via the W boson, but would also contain some interactions from all three flavours via the Z boson, if the other flavours were there due to neutrino oscillation.

- Charged Current (CC): Exclusive to SNO due to the use of heavy water, and

only sensitive to electron neutrinos (as solar neutrinos have insufficient energy to produce the μ or τ required for another flavour to interact.)

- Neutral Current (NC): Also exclusive to SNO, and sensitive to all three flavours of neutrinos.

The first indication of the solution to the Solar Neutrino Problem came with a joint SNO and Super-Kamiokande measurement in 2001 [15]. SNO used the angular distribution of the outgoing electron for ES and CC interactions to separate the two interaction types. SNO had enough ν_e CC events to make a precise measurement of the solar ν_e flux. When combined with the precise Super-Kamiokande ES results (sensitive to all 3 flavours), this indicated that there was a flux of ν_μ and ν_τ as well, with the combined result within the Standard Solar Model prediction for the total neutrino flux.

However, SNO could further refine its measurements by looking for Neutral Current events. Measuring the Neutral Current interaction relied on observing the neutron produced in Equation 2.18, which is beyond the capabilities of a normal Water Cherenkov detector. In its three operational phases, SNO took three different approaches to doing so.

1. The neutron could capture on a deuteron, which causes the emission of a 6.25 MeV gamma ray. This gamma ray would Compton scatter in the detector, producing an electron which would be detected.

2. The neutron capture efficiency was improved by a factor of 3 by adding 2 tonnes of NaCl. This also increased the amount of Cherenkov light produced by a neutron capture, since ^{35}Cl emits multiple gamma rays on neutron capture.

3. The NaCl was removed from the water, and 40 Neutral Current Detectors (NCDs) were arranged vertically in an array inside the detector. The NCDs were each $\sim$5 cm diameter Nickel tubes, containing an 85:15 mixture of ^{3}He : CF_4, and a high voltage anode wire running down the centre. Neutron capture occurs via $n + {}^3\mathrm{He} \rightarrow p + {}^3\mathrm{H}$, with the resulting products ionizing the gas, producing charge that is collected by the anode wire. In this way, the presence of a neutron created an electronic signal that could be read out.

Using data from its first phase (ending in May 2001), SNO was able to independently confirm [16] the presence of other muon and tau neutrinos along with the

expected electron neutrinos in the solar neutrino flux. This was done by comparing the neutrino fluxes measured by each of the ES, CC, and NC processes. This result gave a total neutrino flux that was consistent with the Standard Solar Model. The Solar Neutrino Problem had therefore been solved with confirmation that solar electron neutrinos oscillate.

The Atmospheric Neutrino Anomaly

In the early 1980s, searching for proton decay became an area of experimental interest. Forbidden by conservation of baryon number in the Standard Model (the proton is the lightest particle with 3 quarks), many theories beyond the Standard Model include proton decay. Even in these theories, the half life of a proton is still very long, measurements therefore requiring a large detector (containing lots of protons) heavily shielded from external backgrounds. Although situating the detector underground effectively reduces the background of cosmic ray muons, the atmospheric neutrinos (discussed in Sections 2.1.2 and 2.1.4) would pass through this shielding with ease. It was therefore very important to making proton decay measurements that the atmospheric neutrino background be well understood.

Thankfully, theoretical models had much to say about the expected atmospheric neutrino flux at the time. The cosmic ray muon flux was well studied at the time, and given the known atmospheric neutrino production processes, provided predictive power as to the atmospheric neutrino flux. These known production processes also had predictive power as to the ratio of muon neutrino to electron neutrinos, as a function of energy. At lower energies, both the pion decays in Equations 2.10 and 2.11 and the muon decays in Equations 2.9 and 2.8 would occur in the atmosphere, leading to approximately a 2:1 ratio of $(\nu_\mu + \bar{\nu}_\mu) : (\nu_e + \bar{\nu}_e)$. As energies increase, the muon would be less and less likely to decay before reaching the Earth, resulting in fewer ν_e or $\bar{\nu}_e$, increasing this ratio.

Two of the proton decay experiments at the time, both Water Cherenkov detectors, looked into the atmospheric neutrino background in more detail. The Irvine-Michigan-Brookhaven (IMB) experiment was located in the Fairport salt mine in the United States, and the Kamioka Nucleon Decay Experiment (KamiokaNDE) in Japan (the predecessor to both Kamiokande-II and Super-Kamiokande). The detectors were both able to distinguish ν_μ or $\bar{\nu}_\mu$ interactions (μ-like events) from ν_e or $\bar{\nu}_e$ interactions (e-like events), the methodology for which is discussed in the context of

Super-Kamiokande and T2K in Section 3.4. They could therefore make measurements of the ratio of μ-like events to e-like events (R_{obs}), and compare them to the theory prediction (R_{theory}). Ultimately, the difference was quite profound, the IMB measurement giving an R_{obs}/R_{theory} of $0.54 \pm 0.05 \pm 0.11$ [69], and KamiokaNDE measuring an R_{obs}/R_{theory} of $0.60^{+0.07}_{-0.06}$(stat.)$\pm$0.05(syst.) [65]. There was therefore a deficit in the atmospheric muon neutrino flux at the detectors relative to the theoretical predictions.

This Atmospheric Neutrino Anomaly was ultimately solved by Super-Kamiokande in 1998 [56]. In addition to separating the μ-like and e-like events, the direction of the outgoing muon or electron provides information on the direction of the neutrino that interacted to produce it. When comparing this direction to the cosine of the zenith angle (angle made with the vertical), there is a clear angular dependence in the difference between the event rate expected in the model and the measured event rate.

This angular dependence is ultimately a proxy for how far the neutrino travelled: $\cos\theta = 1$ corresponding to only a few tens of kilometres from the upper atmosphere, and $\cos\theta = -1$ corresponding to thousands of kilometres through the Earth. As will be discussed in Section 2.3.2, in neutrino oscillation theory the probability of neutrino oscillation has a sinusoidal dependence on L/E, where L is the distance the neutrino travelled, and E its energy. Using the zenith angle to calculate L, and combining that with the reconstructed neutrino energy revealed an L/E dependence consistent with neutrino oscillation of $\nu_\mu \to \nu_\tau$. The Atmospheric Anomaly was therefore solved once neutrino oscillation was taken into account.

2.3.2 Neutrino oscillation formalism

The resolution of both the Solar Neutrino Problem and the Atmospheric Neutrino Anomaly was the determination that neutrinos oscillate, i.e. change from one flavour to another. In this section, the mechanism by which neutrino oscillation occurs in a vacuum is discussed, followed by how this is modified for neutrinos passing through matter.

Neutrino oscillation in a vacuum

As discussed earlier in this chapter, our understanding of neutrinos originates entirely in how they are produced and how they are detected, that is, how they participate in

the weak interaction. From this we have three flavours of neutrinos, ν_e, ν_μ, and ν_τ, one corresponding to each of the negatively charged leptons, along with antineutrinos $\bar{\nu}_e$, $\bar{\nu}_\mu$, and $\bar{\nu}_\tau$, corresponding to each of the positively charged leptons. In the Standard Model, neutrinos are massless, but the phenomenon of neutrino oscillation requires neutrinos to have mass in order for it to occur. Neutrino oscillation is therefore compelling evidence of physics beyond the Standard Model.

To see how neutrino masses give rise to neutrino oscillation, consider the three neutrino flavours as Quantum Mechanical states, $|\nu_e\rangle$, $|\nu_\mu\rangle$, and $|\nu_\tau\rangle$, referred to as the *flavour eigenstates*. In Quantum Mechanics, the Hamiltonian operator, H, gives the total energy of a state $|\psi\rangle$, with time evolution of the state according to the Schrödinger Equation, Equation 2.19.

$$i\hbar\frac{\partial}{\partial t}|\psi(t)\rangle = H|\psi(t)\rangle \tag{2.19}$$

If H is time independent, a solution takes the form given in Equation 2.20.

$$|\psi(t)\rangle = e^{-iHt/\hbar}|\psi(0)\rangle \tag{2.20}$$

If $|\psi(0)\rangle$ is expressed as a superposition of the orthonormal eigenstates of the Hamiltonian, $|\psi_j\rangle$, where E_j are the eigenvalues of the Hamiltonian, it evolves in time as shown in Equation 2.21.

$$|\psi(t)\rangle = \sum_j a_j e^{-iE_j t/\hbar}|\psi_j\rangle \tag{2.21}$$

Therefore, the time dependent phase applied to each eigenstate in the superposition is a function of the corresponding eigenvalue of the Hamiltonian. Since the probability of observing the state $|\psi(0)\rangle$ after a time t given by $|\langle\psi(0)|\psi(t)\rangle|^2$, these changes in phases between the eigenstate constituents produce real changes in the observed state.

For a massive neutrino not subject to any signficant potential field, its total energy E is a function of its momentum $\vec{p}$ and mass m as given in Equation 2.22.

$$E = \sqrt{|\vec{p}|^2c^2 + m^2c^4} \tag{2.22}$$

The Hamiltonian is therefore mass dependent. The eigenstates of the Hamiltonian are therefore referred to as the *mass eigenstates*, of which there are currently thought

to be three, denoted $|\nu_1\rangle$, $|\nu_2\rangle$, and $|\nu_3\rangle$. The relationship between the mass eigenstates and the flavour eigenstates is given by the PMNS (Pontecorvo-Maki-Nakagawa-Sakata) matrix , named after the theorists who formulated the theory of neutrino oscillation [75, 81]. The PMNS matrix parametrizes neutrino oscillation with three mixing angles (θ_{12}, θ_{23}, and θ_{13}) and a CP violating phase, δ_{CP}, and abbreviating $c_{ij} = \cos\theta_{ij}$, and $s_{ij} = \sin\theta_{ij}$ can be written as the product of three rotation matrices with a complex phase, shown in Equation 2.23.

$$\begin{pmatrix} U_{e1} & U_{e2} & U_{e3} \\ U_{\mu 1} & U_{\mu 2} & U_{\mu 3} \\ U_{\tau 1} & U_{\tau 2} & U_{\tau 3} \end{pmatrix} = \begin{pmatrix} c_{12} & s_{12} & 0 \\ -s_{12} & c_{12} & 0 \\ 0 & 0 & 1 \end{pmatrix} \begin{pmatrix} c_{13} & 0 & s_{13}e^{-i\delta_{CP}} \\ 0 & 1 & 0 \\ -s_{13}e^{i\delta_{CP}} & 0 & c_{13} \end{pmatrix} \begin{pmatrix} 1 & 0 & 0 \\ 0 & c_{23} & s_{23} \\ 0 & -s_{23} & c_{23} \end{pmatrix} \quad (2.23)$$

This can then be written in the form of Equation 2.24.

$$U = \begin{pmatrix} U_{e1} & U_{e2} & U_{e3} \\ U_{\mu 1} & U_{\mu 2} & U_{\mu 3} \\ U_{\tau 1} & U_{\tau 2} & U_{\tau 3} \end{pmatrix} = \begin{pmatrix} c_{12}c_{13} & c_{13}s_{12} & e^{-i\delta_{CP}}s_{13} \\ -s_{12}c_{23} - e^{i\delta_{CP}}c_{12}s_{13}s_{23} & c_{12}c_{23} - e^{i\delta_{CP}}s_{12}s_{13}s_{23} & c_{13}s_{23} \\ -e^{i\delta_{CP}}c_{12}s_{13}c_{23} + s_{12}s_{23} & -e^{i\delta_{CP}}s_{12}s_{13}c_{23} + c_{12}s_{23} & c_{13}c_{23} \end{pmatrix} \quad (2.24)$$

From the PMNS matrix comes the following correspondance between mass and flavour eigenstates for neutrinos (Equation 2.25) and antineutrinos (Equation 2.26).

$$|\nu_\ell\rangle = \sum_{j=1}^{3} U^*_{\ell j} |\nu_j\rangle \quad (2.25)$$

$$|\bar{\nu}_\ell\rangle = \sum_{j=1}^{3} U_{\ell j} |\bar{\nu}_j\rangle \quad (2.26)$$

With the correspondance between mass and flavour eigenstates parametrized, the time evolution of a flavour eigenstate can be computed, by determining the eigenvalues of the Hamiltonian for use in Equation 2.21. Derivations making minimal simplifying assumptions have been performed (see the discussion in "NEUTRINO MASS, MIXING, AND OSCILLATIONS" in [79]), but a simplified derivation (like that from [40]) provides a sufficiently accurate result. For such a derivation, consider Equation 2.22. Take the ultrarelativistic limit ($p >> mc$, which definitely holds for observable neutrinos, since given their very small mass, they travel at nearly c), and assume that all mass eigenstates travel at the same momentum, p, which in this limit

is approximately equal to E/c, where E is the neutrino energy. Then, the Taylor expansion gives the energy eigenstates shown in Equation 2.27.

$$E_j \approx E + \frac{m_j^2 c^4}{2E} \tag{2.27}$$

Furthermore, since the speed is approximately c, then $t \approx L/c$, so making that substitution results in the oscillation probabilities of Equation 2.28 for neutrinos, and Equation 2.29 for antineutrinos, where $\mathcal{R}^{kj}_{\alpha\beta} = \text{Re}\left[U^*_{\alpha k} U_{\beta k} U_{\alpha j} U^*_{\beta j}\right]$ and $\mathcal{J}^{kj}_{\alpha\beta} = \text{Im}\left[U^*_{\alpha k} U_{\beta k} U_{\alpha j} U^*_{\beta j}\right]$, $\Delta m_{kj} = m_k^2 - m_j^2$ is in eV, L is in km and E is in GeV.

$$P(\nu_\alpha \to \nu_\beta) = \delta_{\alpha\beta} - 4\sum_{k>j} \mathcal{R}^{kj}_{\alpha\beta} \sin^2\left(\frac{1.267\Delta m^2_{kj} L}{E}\right) + 2\sum_{k>j} \mathcal{J}^{kj}_{\alpha\beta} \sin\left(\frac{2.534\Delta m^2_{kj} L}{E}\right) \tag{2.28}$$

$$P(\bar{\nu}_\alpha \to \bar{\nu}_\beta) = \delta_{\alpha\beta} - 4\sum_{k>j} \mathcal{R}^{kj}_{\alpha\beta} \sin^2\left(\frac{1.267\Delta m^2_{kj} L}{E}\right) - 2\sum_{k>j} \mathcal{J}^{kj}_{\alpha\beta} \sin\left(\frac{2.534\Delta m^2_{kj} L}{E}\right) \tag{2.29}$$

The difference between these two oscillation probabilities is the sign of the third term, concerning the quantity $\mathcal{J}$. If α and β are the same flavour (i.e. like in an experimental search for disappearance of a certain flavour), this term is zero, and there is no difference in the oscillation probabilities, as one would expect under CPT conservation. In other words, measuring the disappearance of a neutrino flavour in a vacuum is insensitive to the complex phase δ_{CP}. However, if α and β are different flavours, if there is CP violation in neutrino oscillations (δ_{CP} is neither 0 nor $\pm\pi$), a difference between $P(\nu_\alpha \to \nu_\beta)$ and $P(\bar{\nu}_\alpha \to \bar{\nu}_\beta)$ would be present.

Neutrino oscillation in matter

Alas, neutrino experiments are not conducted entirely in a vacuum. The departure from a vacuum can range from as little as the Earth's atmosphere, to the roughly constant density material making up the Earth's crust and mantle, all the way to the body of the sun, including very high densities that decrease going out from its core. It is therefore important to consider the effect that travelling through matter has on neutrino oscillations. This is often referred to simply as *matter effects*, or the Mikheyev-Smirnov-Wolfenstein (MSW) Effect, after three theorists who developed

it [76, 77, 96].

In matter, there is a possibility for neutrinos to interact. Processes that have no neutrino in the final state (most Charged Current processes) are not relevant to the time evolution of neutrinos that actually make it to the detector, so don't have any effect (beyond a miniscule reduction in neutrino flux as a function of L). In addition, Neutral Current processes are independent of neutrino flavour, and therefore occur equally for all mass eigenstates. This leaves one type of interaction, W boson mediated Elastic Scattering off of electrons, or $\nu_e + e^- \rightarrow e^- + \nu_e$ for electron neutrinos, and $\bar{\nu}_e + e^- \rightarrow e^- + \bar{\nu}_e$ for electron antineutrinos. Only the electron flavour can participate in this W boson mediated interaction, so the effect is flavour dependent, and would therefore have an effect on neutrino oscillation.

To determine what the matter effects are, consider the vacuum treatment of the previous section, and in particular, the Hamiltonian. In a vacuum, the total energy of the neutrino is a combination of its kinetic energy and energy due to its mass. In matter, the ability of the electron neutrino and antineutrino to undergo W boson mediated Elastic Scattering adds an effective potential energy term to the Hamiltonian, dependent on the electron density and the distance travelled in the material. As a result, the matter Hamiltonian has different mass eigenstates than the vacuum Hamiltonian (i.e. the effective mass of each of the mass eigenstates is different in matter.) Neutrino oscillation in matter therefore proceeds relative to these matter mass eigenstates, and the PMNS matrix transformed to give the correspondance between the flavour eigenstates and the matter mass eigenstates. This produces complicated dependences on the various mixing parameters and mass squared splittings, which are discussed in detail in [55]. The MSW Effect can have important consequences for measurements of neutrino oscillation, as will be discussed in the next section.

2.3.3 Current status

The PMNS matrix (Equation 2.23) parametrizes neutrino oscillation with three mixing angles (θ_{12}, θ_{23}, and θ_{13}) and a CP violating phase, δ_{CP}. In addition, the mass squared splittings (Δm^2_{21}, Δm^2_{32}, and Δm^2_{31}) enter into the calculation of survival and disappearance probabilities for a flavour eigenstate. Through the combined efforts of neutrino oscillation experiments around the world, most of these parameters have been measured, but some mysteries still remain.

The world knowledge of these parameters as of the 2014 Particle Data Group's

Review of Particle Physics [79] is shown in Table 2.3.

Parameter	Value
θ_{12}	$33.4^\circ\ ^{+0.9^\circ}_{-0.8^\circ}$
Δm^2_{21}	$(7.53 \pm 0.18) \times 10^{-5}$ eV^2
θ_{23}	$45.8^\circ \pm 3.2^\circ$
$\lvert\Delta m^2_{32}\rvert$	$(2.44 \pm 0.06) \times 10^{-3}$ eV^2
θ_{13}	$8.9^\circ \pm 0.4^\circ$

Table 2.3: World knowledge of neutrino mixing parameters (Normal Hierarchy), taken directly or calculated from the listings of the 2014 Particle Data Group Review of Particle Physics [79].

This data comes from multiple different types of experiments:

- Solar neutrino experiments though electron neutrino disappearance are sensitive to θ_{12} and Δm^2_{21}.
- Reactor neutrino experiments through electron antineutrino disappearance are sensitive to θ_{12}, Δm^2_{21}, and θ_{13}.
- Atmospheric neutrino experiments through muon neutrino disappearance are sensitive to θ_{23} and $|\Delta m^2_{32}|$ or $|\Delta m^2_{31}|$.
- Accelerator neutrino experiments through muon neutrino disappearance are sensitive to θ_{23} and $|\Delta m^2_{32}|$ or $|\Delta m^2_{31}|$, and through electron neutrino appearance are sensitive to θ_{13} and δ_{CP}.

The most recent mystery to be solved concerns the value of θ_{13}. Up until 2011, reactor and accelerator experiments had only successfully placed upper limits on its value. The question as to whether it was identically 0 was of great theoretical concern, as in the PMNS matrix (Equation 2.23) this would force there to be no CP violation in neutrino oscillations. Initial indications from electron neutrino appearance at T2K [2], followed soon after by definitive measurements of electron antineutrino disappearance from the reactor experiments Daya Bay [20], Double Chooz [9], and RENO [18] demonstrated that not only was θ_{13} non-zero, but is in fact large enough that a measurement of δ_{CP} is within experimental reach. Combining the T2K δ_{CP} dependent electron neutrino appearance measurement with the reactor δ_{CP} independent electron antineutrino disappearance measurement has produced some interesting

hints as to the value of δ_{CP} [8], but this is still an area of current and future interest in neutrino oscillation physics.

Another mystery remaining in neutrino physics concerns the signs of the $\Delta m^2_{kj} = m^2_k - m^2_j$. In all of the different types of neutrino oscillation experiments discussed earlier in this section, the dominant observation of neutrino oscillation comes from a disappearance channel (i.e. measurements based on detecting fewer neutrinos than expected, and computing $P(\nu_\alpha \to \nu_\alpha)$. Looking back at Equations 2.28 and 2.29, we see that when measuring the disappearance of a neutrino flavour, $\mathcal{J}^{kj}_{\alpha\beta} = 0$, and the oscillation probability is independent of the sign of Δm^2_{kj}. However, the MSW Effect can sufficiently modify the mixing such that the sign of the Δm^2_{kj} term can be determined. In the case of solar neutrinos, the extreme electron density present in the sun results in the MSW Effect being very significant [77], measurements therefore being able to establish that $m_1 < m_2$. As shown in Table 2.3, it has been established that $|\Delta m^2_{32}| \approx |\Delta m^2_{31}| >> \Delta m^2_{21}$, but it is currently unknown as to whether the mass hierarchy is $m_1 < m_2 < m_3$ (referred to as *Normal Hierarchy*) or $m_3 < m_1 < m_2$ (referred to as *Inverted Hierarchy*). Neutrino oscillation analyses sensitive to these parameters (for example, that discussed in Chapter 7) are therefore performed twice, once for each mass hierarchy assumption. Determining which mass hierarchy is correct remains a goal for current and future neutrino experiments.

Chapter 3

The T2K Experiment

The T2K Experiment [3] is a long-baseline neutrino oscillation experiment. A beam of muon neutrinos or antineutrinos is produced at the Japan Proton Accelerator Research Complex (J-PARC) in Tokai, Japan. There is a near detector complex located 280 m from the neutrino production target, and the far detector, Super-Kamiokande, is located 295 km from the neutrino production target. This chapter describes the goals of the experiment, and each component of the experimental apparatus in more detail.

3.1 Physics goals

At the time T2K was proposed, the value of the mixing parameter θ_{13} was unknown. It had been limited to a small value by the CHOOZ experiment [24], but as discussed in Section 2.3, a value of zero was a possibility, which would have had interesting theoretical consequences. So, a major T2K design goal was to be sensitive to values of $\sin^2 2\theta_{13}$ a factor of 20 smaller than the CHOOZ limit, corresponding to a T2K sensitivity for $\sin^2 2\theta_{13} > 0.008$ at the 90% CL, for $\delta_{CP} = 0$. This was to be accomplished by searching for $\nu_\mu \rightarrow \nu_e$ oscillation in a muon neutrino beam (a process that had not been observed before).

The muon neutrino beam also provided an opportunity to measure muon neutrino disappearance. T2K thus set the goal of making precise measurements of muon neutrino disappearance, specifically to the precision of $\delta(\Delta m^2_{23}) \sim 10^{-4}$ eV^2 and $\delta(\sin^2 2\theta_{23}) \sim 0.01$.

In addition to these neutrino oscillation goals, the inclusion of a near detector

also enables studies of neutrino interactions with matter to be performed. It is also possible to look for signs of sterile neutrinos (neutrino flavours that do not interact, but which do participate in neutrino oscillations).

As was shown in Section 2.3, the neutrino oscillation probabilities that T2K neutrino oscillation measurements are meant to probe are dependent on Equation 3.1:

$$\sin^2 \frac{\Delta m^2 L}{4E} \tag{3.1}$$

In Equation 3.1, $\Delta m^2 = \Delta m^2_{32}$ or Δm^2_{13} (NH or IH, respectively). In order to have the maximum probability of neutrino oscillation (and hence the largest effect to measure), an experimental configuration that makes Equation 3.1 as close as possible to 1 is needed. Given that Δm^2 was reasonably well known during the design phase of T2K, this meant choosing a suitable value of L/E, where L is the distance between the neutrino production point and the detector meant to observe the oscillations, and E is the energy of the neutrinos. Therefore, given the distance between J-PARC and Super-Kamiokande, producing neutrinos at J-PARC with the optimal energy was an important design consideration.

One additional element of fine tuning with regards to the neutrino energy was also incorporated into the T2K experimental design: directing the neutrino beam such that it defines an axis pointing 2.5° away from Super-Kamiokande. When a pion decays (Equation 3.3 and Equation 3.4), the energy of the neutrino is given [73] by Equation 3.2, where θ is the angle the neutrino direction makes with the pion direction (in the lab frame), and $\gamma = E_\pi/m_\pi$.

$$E_\nu = \frac{(1 - (m_\mu/m_\pi)^2)E_\pi}{1 + \gamma^2\theta^2} \tag{3.2}$$

The resulting dependence of the neutrino energy on the pion energy, for a few different angles it makes with the pion direction, is shown in Figure 3.1.

Unfortunately, the method described in Section 3.2.2 for producing the pions does not produce a monoenergetic pion beam. However, Figure 3.1 indicates that if off-axis neutrinos were considered, even a large range of pion energies could translate to a relatively small range of lower energy neutrinos. What this means for T2K is shown in Figure 3.2. At the T2K off-axis angle of 2.5°, the neutrino energy spectrum is peaked at the energy at which neutrino oscillation is most probable, $\sim$ 0.6 GeV. In addition, since the signal interaction process (CCQE) dominates at these lower

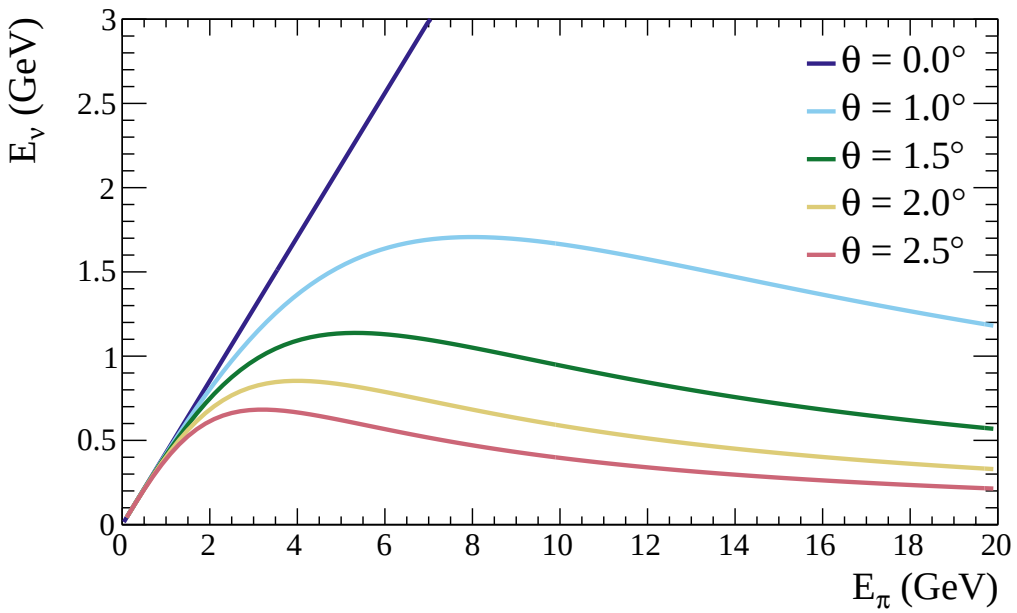

Figure 3.1: The energy of the neutrino produced in a pion decay, for different angles between the neutrino direction and the pion direction (in the lab frame), as a function of pion energy. Generated by plotting Equation 3.2 for different values of θ.

energies, this reduction in the number of high energy neutrinos (relative to smaller off-axis angles) reduces the incidence of the background interaction processes, thus reducing uncertainties in the measurement of neutrino oscillation.

As discussed in Section 2.3.3, much has changed since the construction of T2K. T2K measurements of muon neutrino disappearance have produced the world's most precise measurement of $\sin^2\theta_{23}$. T2K's observation of $\nu_\mu \rightarrow \nu_e$ oscillation and reactor experiments have established $\sin^2 2\theta_{13}$ to be sufficiently far from 0 that experimental probes of δ_{CP} are possible, with some interesting hints already appearing.

As described in 3.2.2, it is possible for T2K to produce and measure a muon antineutrino beam instead of the muon neutrino beam used for the earlier results. With interesting measurements already made with the neutrino beam, the decision to run in antineutrino beam mode was made. This allows study of muon antineutrino oscillation, including precision measurements of muon antineutrino disappearance, and a search for electron antineutrino appearance in the muon antineutrino beam. As discussed in Section 2.3, comparing muon neutrino disappearance and muon antineutrino disappearance provides a test of the CPT Theorem. In addition, measuring the

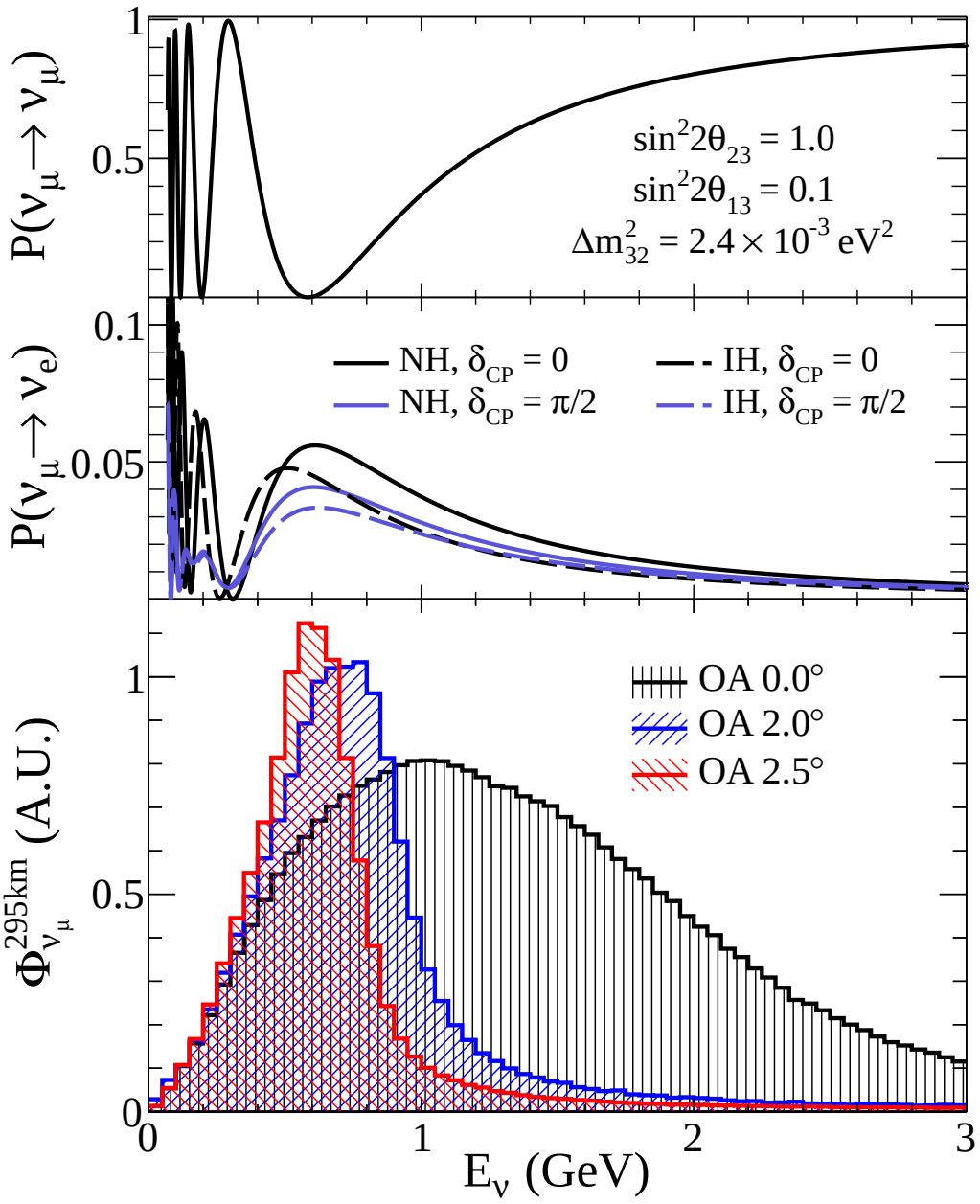

Figure 3.2: The neutrino energy spectrum at Super-Kamiokande (in arbitrary flux units) for different angles relative to the beam axis. The muon neutrino survival probability, and electron neutrino appearance probability are shown, demonstrating that for the 2.5° off-axis angle, the flux is peaked near maximal oscillation probability. From [89], though published earlier in [4].

difference between electron neutrino appearance and electron antineutrino appearance could allow T2K to measure δ_{CP} without relying on the reactor constraint, as discussed in Section 2.3.3.

3.2 The Japan Proton Accelerator Research Complex

The neutrino beam that T2K measures is produced by the Japan Proton Accelerator Research Complex [97], abbreviated as J-PARC. This facility is located in Tokai, Ibaraki, on the East coast of Japan. It consists of three proton accelerators, with multiple different experiments making use of various proton beam configurations. In the case of T2K, protons are directed from the *Main Ring* to the *neutrino beamline*, and the neutrinos and antineutrinos that T2K studies are produced there.

3.2.1 The proton accelerators

The proton beam begins with a source of protons to accelerate. In the case of J-PARC, this takes the form of a source of H^- ions. These are injected into a linear accelerator, the LINAC. The LINAC accelerates the H^- ions up to a kinetic energy of 400 MeV. The H^- ions are then passed through charge-stripping foils in order to turn them into H^+ ions (i.e. protons), and injected into the RCS ("Rapid-Cycling Synchroton").

The RCS accelerates the protons up to a kinetic energy of 3 GeV, with a 25 Hz cycle, and two bunches in a cycle. Of these proton bunches, 95% are extracted for use in the Materials and Life Science Facility, and the remaining 5% are injected into the Main Ring (MR).

The MR accelerates the protons up to a kinetic energy of 30 GeV, in 8 bunches. When the proton beam is being directed towards the neutrino beamline, the MR is operated in a mode called *Fast Extraction*, whereby all 8 bunches are extracted from the MR in one turn around the ring. This sends one 8 bunch spill towards the neutrino beamline.

3.2.2 The neutrino beamline

The first section of the neutrino beamline is referred to as the primary beamline. It is divided into three sections: the 54 m long preparation section, the 147 m long arc section, and the 37 m long final focusing section. The preparation section tunes the beam so that it is suitable for the arc section. In the preparation section, there are also multiple beamline monitors that measure the beam intensity, position, profile,

and beam loss. The purpose of the arc section is to bend the beam towards the direction of Kamioka, which is an 80.7° change of direction, with a 104 m radius of curvature. There are also monitors for the beam position, profile, and beam loss in this section. With the proton beam properly directed by the arc section, it enters the final focusing section, which guides and focuses the beam onto the target, and directs it downward from the horizontal by 3.627°. The final focussing section also contains monitors that measure the beam intensity, position, profile, and beam loss. Thus, at the end of the primary beamline, the proton beam has been tuned and directed as needed, and its properties are well understood.

Upon exiting the primary beamline, the protons enter the secondary beamline. It begins with the target station. Here, the beam passes through a baffle, which collimates the beam. Then it passes through another beam profile monitor [38], just upstream of the target. The collisions of the 30 GeV protons in the graphite target result in the production of additional particles. This is modelled using a combination of FLUKA [52, 33, 43] and GEANT3 [42] (with GCALOR [98]), and tuned to external data from pion scattering experiments, as well as the experiment NA61/SHINE. Among the particles produced that are relevant for neutrino production, pions are the most prominent, though kaons are also produced. These charged particles are focussed by three magnetic horns. The direction of the 250 kA current flowing through them determines the direction of the magnetic field inside of them, and hence whether positive particles are focussed down the decay volume and negative particles bent out of the beam path, or vice versa.

In neutrino beam mode, the π^+ are focussed. Their decays result in muon neutrinos via Equation 3.3.

$$\pi^+ \rightarrow \mu^+ + \nu_\mu \tag{3.3}$$

In antineutrino beam mode, the π^- are focussed. Their decays result in muon antineutrinos via Equation 3.4.

$$\pi^- \rightarrow \mu^- + \bar{\nu}_\mu \tag{3.4}$$

As stated earlier, kaons are also produced in the target, and neutrinos from their decays contribute to the beam content. In addition, some of the muons produced in the pion decays also decay within the decay volume (via Equation 2.8 and Equation 2.9), making further contributions. As a result, the beam contains a combination of ν_μ, $\bar{\nu}_\mu$, ν_e, and $\bar{\nu}_e$, though the desired flavour dominates in each beam mode.

At the end of the $\sim$ 96 m long decay volume is the beam dump. It provides 3.174 m of graphite and 2.40 m of iron in the beam path, only allowing muons with a momentum above $\sim$ 5.0 GeV/c to pass through it. Just past the beam dump there is a detector (the muon monitor) which uses these muons to measure the neutrino beam intensity and direction. The remaining distance between the end of the muon monitor and the near detector complex is composed of the sand that J-PARC is built on, and is sufficient to stop any muons that remain, so that only neutrinos and antineutrinos make it to the near detector complex.

3.3 The near detector complex

The near detector complex is located on the J-PARC site, 280 m from the target. The detectors are contained inside a cylindrical pit dug into the ground, 37 m deep, with a diameter of 17.5 m, with 3 floors to provide support for the detectors themselves and the various services that are required for detector operation. The pit contains two detectors: INGRID ("Interactive Neutrino GRID"), centered on the beam axis, and ND280 ("Near Detector, 280 m"), situated 2.5° off-axis. In this section the structure and function of these detectors will be discussed, along with concepts relevant to their operation. Their positioning relative to each other, and their locations in the pit are shown in Figure 3.3.

3.3.1 INGRID

The INGRID detector is made up of 16 identical modules, arranged as shown in Figure 3.4. The centre of the cross, with two overlapping modules, is positioned at the beam centre (i.e. "on-axis"). The two modules outside of the cross shape check the axial symmetry of the beam. As a whole, INGRID monitors the neutrino beam direction and intensity. It has also been used to study neutrino interactions.

The INGRID modules are constructed of a sandwich of 9 iron plates (providing a dense target for neutrinos to interact with) and 11 tracking scintillator planes, and are surrounded by veto scintillator planes to reject external backgrounds. When a charged particle passes through scintillator, the molecules are moved into an excited state, which decays down to the ground state, emitting a photon of a characteristic frequency: a scintillation photon. The scintillator planes consist of rectangular scintillator bars, optically isolated from each other. Each bar has a wavelength shifting

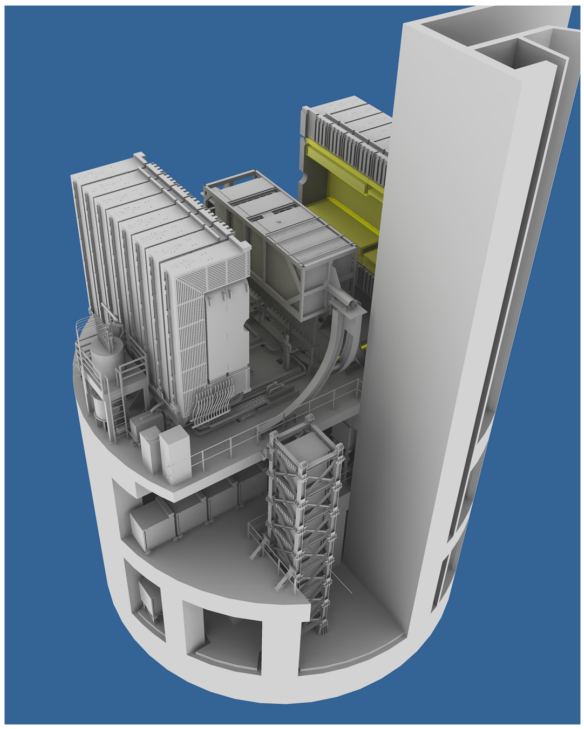

Figure 3.3: The positioning of the ND280 off-axis detector and the INGRID on-axis detector in the near detector complex pit. ND280 (with the magnet open) is located on the upper level. The horizontal INGRID modules are located on the level below, and the vertical INGRID modules span the bottom two levels. From [3].

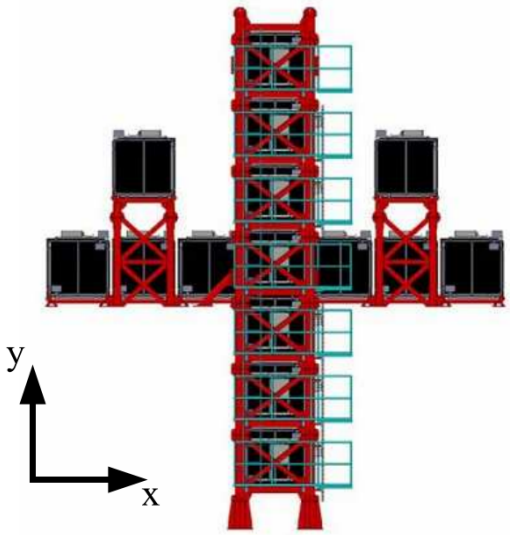

Figure 3.4: Diagram of INGRID, showing the positioning of the modules relative to each other and the coordinate system. From [3].

optical fibre running down the centre of it. This fibre absorbs some of the scintillation photons, emitting multiple photons of a lower frequency, some of which are transmitted by the optical fibre to a Multi-Pixel Photon Counter ("MPPC"). Each MPPC contains 667 independent pixels, each one an avalanche photodiode with a gain of the same order as a vacuum photomultiplier (e.g. the PMTs discussed in Section 3.4.) The spectral emission of the wavelength shifting fibres matches the sensitivity of the MPPCs well, and they are insensitive to magnetic fields. The same MPPC design is used for the ND280 subdetectors (where the magnetic field tolerance is especially important, due to those detectors being located inside a magnetic field).

3.3.2 ND280

ND280 is composed of multiple subdetectors contained inside of an electromagnet. A schematic diagram of ND280 is shown in Figure 3.5, which includes the beam direction and the coordinate system used to describe the detector. Each of the constituents of ND280 are explained below, going roughly from the outside in.

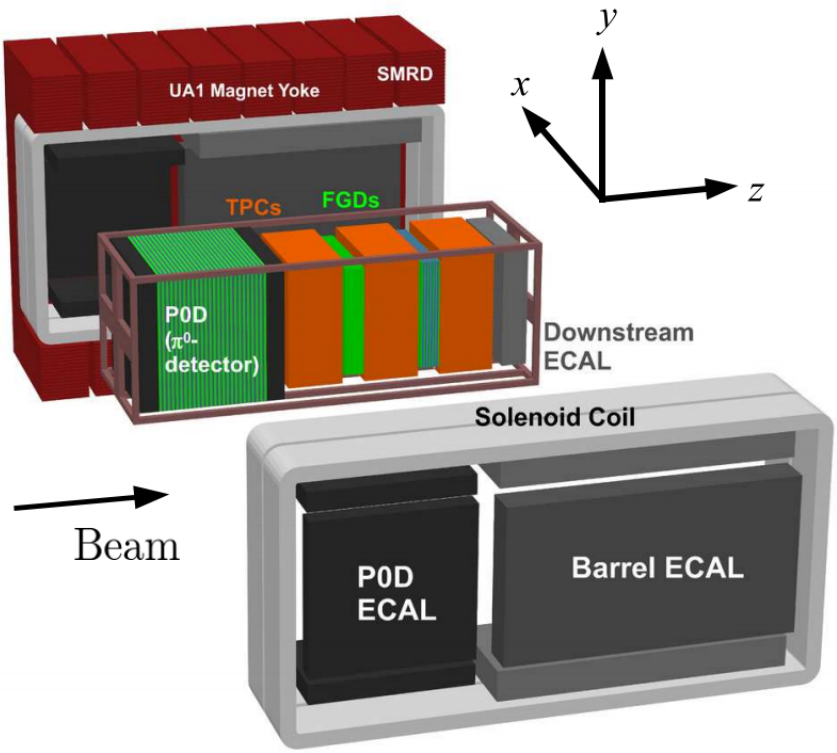

Figure 3.5: A view showing the consituents of the ND280 off-axis detector. The direction of the beam and the detector coordinate system are shown. From [3].

Magnet

The ND280 magnet was originally used in the UA1 experiment, then later reused for the NOMAD experiment (both taking place at CERN.) It was refurbished, shipped in pieces to Japan, and installed at the near detector complex for use in ND280. It provides a 0.2 T dipole magnetic field in the $+x$ direction by passing a current of approximately 2900 A through water-cooled aluminum coils. The space inside the aluminum coils is 7.0 m $\times$ 3.5 m $\times$ 3.6 m , and contains the basket containing most of the ND280 detectors. Outside of the aluminum coils is an iron flux return yoke, weighing 850 tons, and bringing the total external dimensions of the magnet to 7.6 m $\times$ 5.6 m $\times$ 6.1 m The magnet is divided into two mirror-symmetric halves, which are together during normal operation, but can be spread apart to open the magnet to access the detectors inside. Figure 3.3 shows the magnet halves in the "open" position.

Side Muon Range Detector (SMRD)

The SMRD is composed of 440 plastic scintillator modules inserted into the 1.7 cm air gaps between the 4.8 cm thick steel plates of the magnet flux return yoke. Each of the SMRD modules has an S-shaped groove machined into it, into which a wavelength shifting optical fibre has been inserted, which is read out by an MPPC. This configuration allows the SMRD to record muons that escape ND280 with large angles relative to the beam direction, and measure their momenta. It also provides a trigger on cosmic ray muons entering ND280. Finally, it can help identify charged particles entering ND280 from beam neutrino interactions occurring in the magnet or the walls of the near detector complex pit.

Electromagnetic Calorimeter (ECal)

The ECal is made out of alternating layers of lead absorber and plastic scintillator bars (also read out with wavelength shifting optical fibres and MPPCs). It provides near hermetic coverage for the detectors inside the basket, in order to measure particles escaping those detectors. In addition to the ability to detect charged particles and differentiate between electrons, muons, and pions, its particular strength is the detection of photons, which would cause electrons and positrons to be produced within it (an "electromagnetic shower"), allowing their energy and direction to be measured. In the ND280 detectors, π^0 are produced in some neutrino interactions, and rapidly

decay by the process $\pi^0 \rightarrow \gamma + \gamma$. The only way to infer the existence of the π^0 is through these photons, thus the ECal could play an important role in detecting any π^0 produced in the basket detectors.

π^0 Detector (P0D)

The P0D is designed specifically to look for the Neutral Current process $\nu_\mu + N \rightarrow \nu_\mu + N + \pi^0 + X$ on a water target. This process is a background at Super-Kamiokande, as the π^0 decay photons would undergo pair production in the detector ($\gamma \rightarrow e^+ + e^-$), possibly producing a signal resembling ν_e CCQE. The P0D is constructed of x and y layers of triangular scintillator bars, read out with wavelength shifting optical fibres and MPPCs. Alternating with these layers are bags that can be filled with water (to provide the target) and lead and brass sheets (nominally to induce electromagnetic showers from photons, like in the ECal, enabling π^0 detection.) Since neutrinos will interact in the lead and brass (and to a lesser extent, the scintillator), P0D is operated both with and without water in the bags, allowing the water target cross sections to be determined using a subtraction method.

Fine Grained Detectors (FGD)

There are two FGDs inside the ND280 basket: FGD1, located between TPC1 and TPC2, and FGD2, located between TPC2 and TPC3.

FGD1 is constructed entirely of alternating x and y layers of square scintillator bars, which are optically isolated from each other. Down the centre of each bar is a wavelength shifting optical fibre, which captures any scintillation light and brings it to an MPPC to be read out. FGD1 provides an active neutrino target on carbon. That is to say that the dense target volume that neutrinos are meant to interact with is also instrumented, so that the interaction vertex is directly observable.

However, the far detector contains mostly water as a target, and making measurements of neutrino interactions on carbon does not constrain model uncertainties specific to oxygen. For this reason, in FGD2 some of the x and y layers are replaced with water volumes, which enable measurements of neutrino interactions on oxygen to be made. Although these are passive volumes (i.e. they are not instrumented), the remaining x and y scintillator layers still allow FGD2 to measure interactions that occur within it.

Both FGDs are capable of reconstructing charged particle tracks that go through

the scintillator bars. The energy deposition of the particle as is passes through the bars is also measured, and can provide some information about the identity of the particle. This concept is discussed in more detail in the context of the TPCs in Chapter 4, as the TPCs can perform this measurement more precisely, and the FGD particle identification information is only used when the particle does not enter a TPC, as discussed in Chapter 5.

The timing information provided by the scintillator bars is used to provide a definite beginning time for the interaction when reconstructing an event. It also allows the FGDs to tag Michel Electrons produced within them. Michel Electrons are the electrons produced in muon decays, $\mu^- \rightarrow e^- + \bar{\nu}_e + \nu_\mu$ and $\mu^+ \rightarrow e^+ + \nu_e + \bar{\nu}_\mu$. The tagging of Michel Electrons is based on the muon having stopped in the detector. The stopped muon decays after some elapsed time from the beginning of the event, so delayed charge deposition from the electron or positron is the signature that is searched for, as is discussed in Chapter 5. This is one important method for detecting pions produced in neutrino interactions that stopped in the FGD. They will decay into muons that will produce Michel Electrons (via Equation 3.3, or Equation 3.4 if the π^- is not captured on a positive nucleus in the detector before it decays).

Time Projection Chambers (TPC)

The three TPCs are constructed of an instrumented Inner Volume (IV), containing a gas mixture that is 95% Ar, 3% CF_4, and 2% Isobutane, and an Outer Volume (OV) filled with CO_2, which acts as an electrical insulator, and helps keep air from entering the IV. The IV has readout electronics on each end ($\pm x$), and a central cathode in the middle, held at -25 kV, to provide an electric field.

When a charged particle passes through the IV, it ionizes the gas along its track, which is curved by the magnetic field provided by the magnet. The ionization electrons drift under the TPC's electric field to the readout electronics, allowing a 3D track to be reconstructed. Using the curvature of the track under the magnetic field, the particle's momentum is measured via the Lorentz force law. The amount of ionization along the particle's track is also measured, and is used to determine the type of particle that produced the track.

The TPCs and the principles behind their operation are described in more detail in Chapter 4.

3.4 Super-Kamiokande

Super-Kamiokande [57] is the *far detector*, located 295 km away from the neutrino production target, situated 2.5° off-axis. It is located inside the Mozumi mine, inside Mt. Ikenoyama. This gives it a mean overburden of 1000 m of rock, or 2700 meters-water-equivalent. This reduces the background from cosmic ray muons. A schematic diagram of Super-Kamiokande is shown in Figure 3.6.

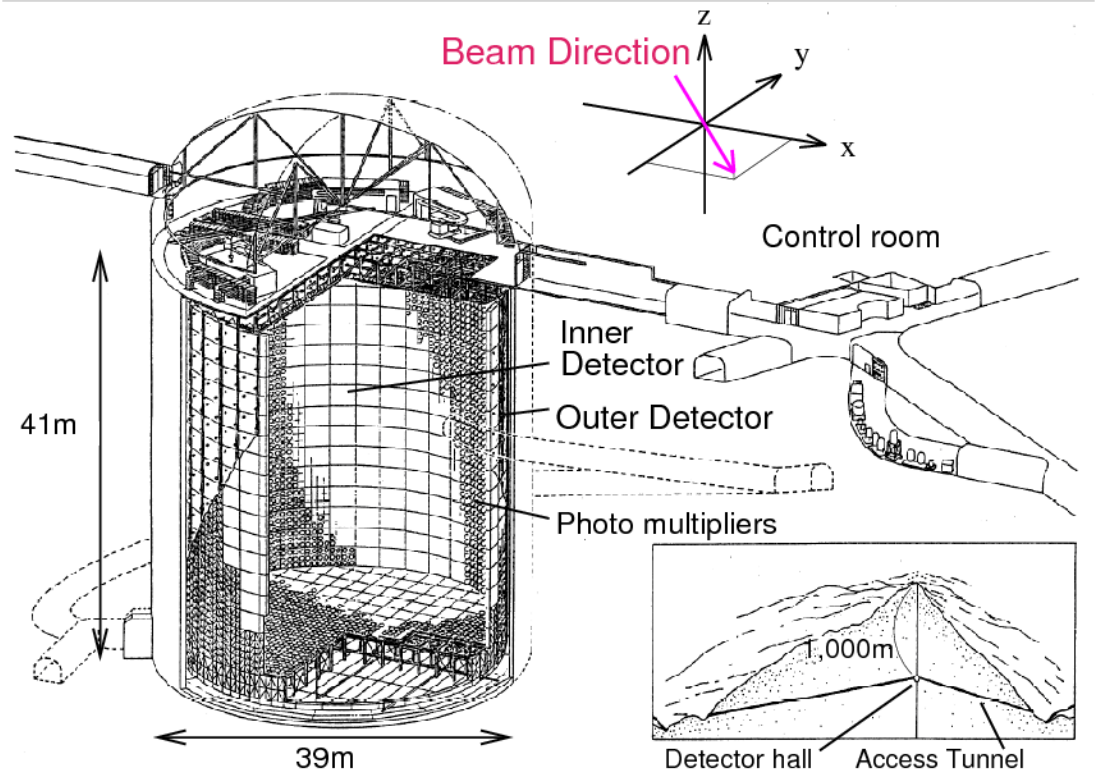

Figure 3.6: A schematic diagram of Super-Kamiokande, including its size, position within Mt. Ikenoyama, and the direction of the beam relative to it. From [4].

The detector is contained inside a cylindrical stainless steel tank, 39 m in diameter and 42 m tall, with a total nominal water capacity of 50 ktons. This tank is divided into two regions: the Inner Detector (ID), and the Outer Detector (OD). The boundary between the ID and OD is a cylindrical stainless steel scaffold, which is about 50 cm wide. It is covered by plastic sheets in order to optically separate the ID and OD, and it also supports the detector instrumentation.

The detector is instrumented with photomultiplier tubes, abbreviated PMTs. PMTs are sensitive light sensors, capable of amplifying a single photon up to a readable signal. As shown in Figure 3.7, when a photon strikes the photocathode, the

photoelectric effect causes an electron to be produced. This electron is accelerated towards the first dynode by the electric field inside the PMT, and upon collision with the dynode, more electrons are produced. This process is repeated for multiple dynodes, producing a signal at the anode that is suitable for the readout electronics.

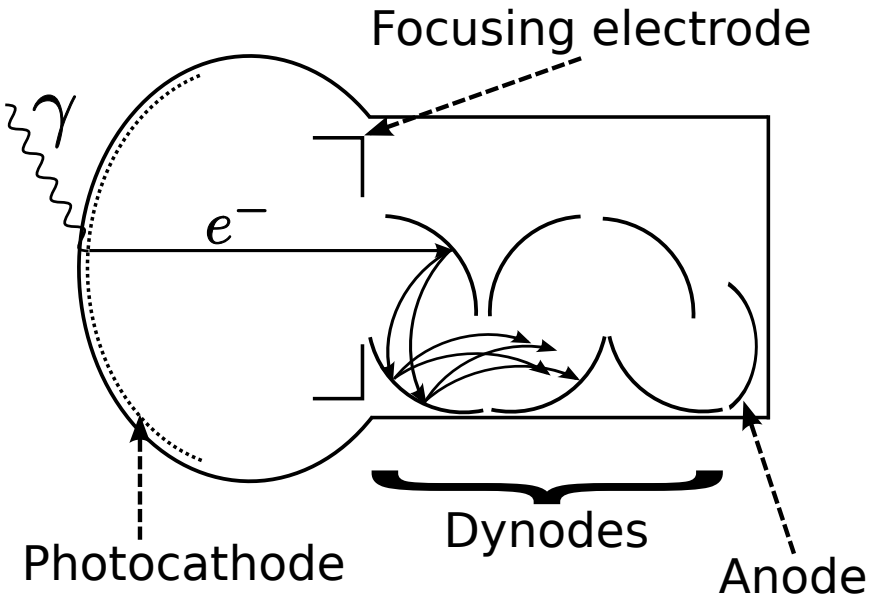

Figure 3.7: A diagram demonstrating the main operating principles of a photomultiplier tube. Drawn using information from [45] and [57].

The OD, which is about 2 m thick radially and on the axis at both ends, is meant primarily to act as an active veto of cosmic ray muons and other backgrounds that enter the detector. It is thus sparsely instrumented by 1885 outward facing PMTs. To compensate, the walls of the OD are lined with Tyvek®, which is highly reflective, and thus increases the chances that photons in the OD will be detected by one of the PMTs.

The ID occupies the remaining space, and is 33.8 m in diameter and 36.2 m in height. Since the ID is meant to perform precise measurements, it is heavily instrumented, with 11129 inward facing PMTs. This provides 40% PMT cathode surface coverage. Since reflected photons would negatively impact the reconstruction, the ID walls are lined with black plastic sheeting to absorb light that does not strike a PMT cathode.

The light that Super-Kamiokande is designed to detect is produced by the Cherenkov Effect. Often descibed as the equivalent of a sonic boom for light, the Cherenkov Effect is the production of light by a charged particle travelling through a medium faster

than the speed of light in the medium. So, given an index of refraction n, speed of light in a vacuum c and charged particle speed v, Cherenkov light is produced when $v > (c/n)$, where $v = (c/n)$ is referred to as *Cherenkov Threshold*. The light is emitted at an acute angle to the direction of the charged particle, $\cos\theta_C = (c/nv)$, producing a cone of light projected in the direction of the particle, centered on the path of the particle. The cone of light produced is detected by the PMTs as a ring, and its properties (such as which PMTs detected light, and the opening angle of the Cherenkov ring) allow identification of the charged particle that produced it (discussed below) and reconstruction of its momentum, direction, and initial position. These are exactly the quantities required for reconstructing the neutrino energy for a CCQE interaction (as shown in Equation 2.13). For electrons, the momentum resolution is estimated to be $0.6\% + 2.6\%/\sqrt{P[\mathrm{GeV/c}]}$, and for muons, $1.7\% + 0.7\%/\sqrt{P[\mathrm{GeV/c}]}$ [8]. For muons at common T2K momenta, this works out to a momentum resolution of approximately 3%. The angular resolution for electrons is estimated to be 3.0° and for muons 1.8° [8]. In addition to these reconstructed quantities, Michel Electrons (described in Section 3.3.2) would also result in delayed charge deposition on the PMTs, and they can therefore be tagged at Super-Kamiokande as well.

Finally, there is the issue of particle identification. The neutrino oscillation goals of T2K require the ability to determine the flavour of neutrino that interacted. In particular, it is important to be able to discriminate between electron neutrinos and muon neutrinos, by being able to discriminate between electrons and muons producing Cherenkov rings in Super-Kamiokande. How this is accomplished is demonstrated in Figure 3.8. As electrons travel through the water in Super-Kamiokande, they scatter, undergo bremsstrahlung, and initiate electromagnetic showers. This results in fuzzy Cherenkov rings, as shown in Figure 3.8b. Muons are much heavier particles ($m_\mu = 105.3$ MeV/c^2, compared to $m_e = 0.511$ MeV/c^2), and thus tend to maintain their initial direction, which results in sharp Cherenkov rings, as shown in Figure 3.8a. This allows Super-Kamiokande to discriminate well between electrons and muons in the detector.

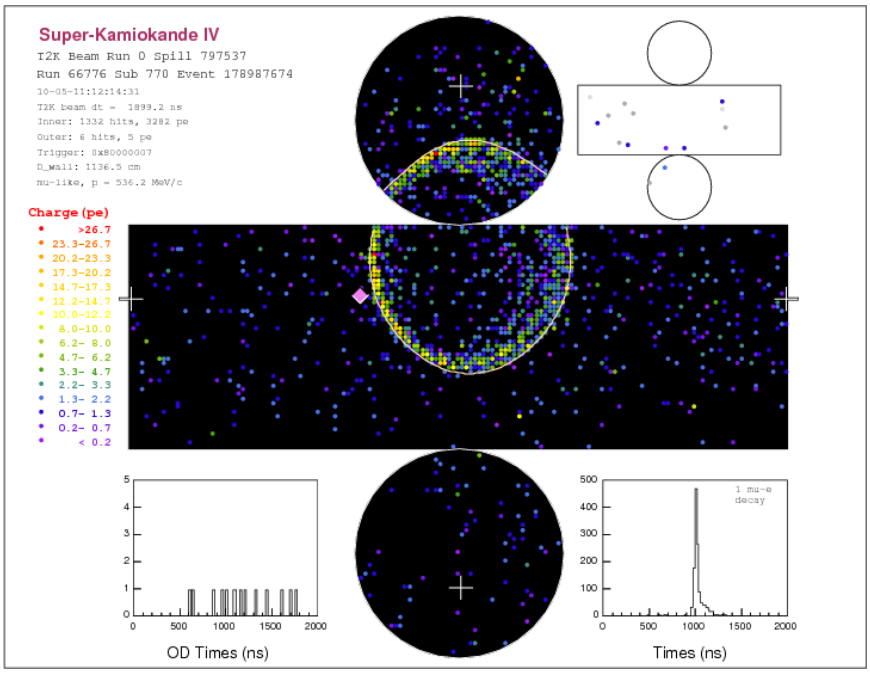

(a) A muon-like ring

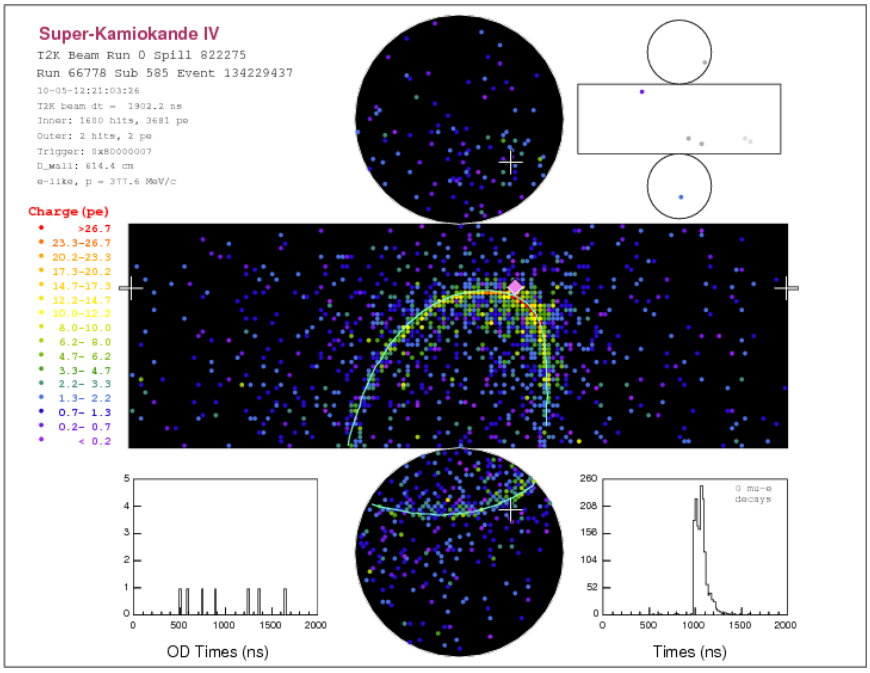

(b) An electron-like ring

Figure 3.8: Two example reconstructed T2K events at Super-Kamiokande, showing the difference between a muon-like ring and an electron-like ring. The cylindrical detector is unrolled onto a plane. If a PMT collected charge, it is shown as a point with a colour corresponding to the charge collected. From [3].

Chapter 4

The T2K Time Projection Chambers

The three Time Projection Chambers (TPCs) [10] are important subdetectors of ND280. They allow ND280 to reconstruct the tracks of charged particles passing through them, providing precise measurements of the particles' momentum, and identification of the particle type. This chapter discusses the fundamental principles behind their operation, along with the key subsystems required for their function.

4.1 Fundamental principles

The TPCs exploit a number of physical principles in order to make measurements of the charged particles passing through them. In this section, these physical principles are introduced, and the specific techniques employed by the ND280 TPCs to exploit them are discussed.

4.1.1 Passage of charged particles through matter

When a charged particle passes through matter, its electric field can act on both the positive nuclei and the surrounding electrons of the atoms that make up the matter. This results in a transfer of energy from the particle to the surrounding matter, and therefore energy loss of the charged particle. The energy transfer is predominantly to the electrons of the atoms, and takes the form of either *excitation*, which leaves the atom in an excited state, or *ionization*, where the electron is given sufficient energy to escape the atom. For the excitation process, the excited state may decay down

into the ground state by emission of a photon, or, if a large spin-parity difference prevents this from occurring, through collision with and subsequent ionization of a second atom, in a phenomenon called the *Penning Effect*.

These processes by which charged particles lose energy while travelling through matter are probabilistic in nature, but the average energy loss over a given distance is quantified by the *Bethe formula*, which relates the energy loss of a charged particle along its trajectory (dE/dx) to the magnitude of the charge of the particle, the speed of the particle, and the composition of the material it is travelling through (including its density.) (For a comprehensive discussion of the Bethe formula, see *32. PASSAGE OF PARTICLES THROUGH MATTER* in [79]). The amount of energy loss of the charged particle in the material therefore translates into a characteristic amount of ionization electrons. This can be used to identify a particle travelling through a detector volume.

4.1.2 Gaseous ionization detector principles and the TPCs

In Section 4.1.1, ionization electrons produced along the trajectory of a charged particle played an important role in its energy loss. The goal of a gaseous ionization detector is to measure the particle's ionization of the gas along its trajectory, and use it to reconstruct the properties of the particle. In a TPC, this is accomplished by drifting the ionization electrons to the ends of the TPC (the readout planes), where they produce a signal that is read out. This provides a two dimensional projection of the position of the track, which when combined with the arrival time of the ionization electrons, allows for 3D reconstruction of the track.

To cause the ionization electrons to drift in the desired direction, an electric field is applied. This nominally uniform electric field is chosen to be large enough that the ionization electrons move away from the ions (instead of recombining with them), but small enough that the ionization electrons do not attain sufficient energy to ionize additional atoms in the gas. For the ND280 TPCs, this nominal electric field strength is approximately 275 V/cm. As the electrons drift through the gas, they collide with atoms in the gas, losing energy. This limits the maximum velocity they can attain. The average velocity of the ionization electrons as they drift towards the end of the TPCs is called the *drift velocity*. Good knowledge of the drift velocity is essential to using the arrival time of the ionization electrons to reconstruct the 3D track position. For the ND280 TPCs, the drift velocity is approximately 78.5 mm/μs, and it is one

of the quantities monitored by the calibration systems discussed in Section 4.4.

In a gas, absent an electric field, the ionization electrons would undergo diffusion, before the random nature of that process brings them back to a position where they recombine with the ion. Although the presence of the electric field in the drift direction causes them to move on average in the drift direction, diffusion still occurs, broadening the distribution of the ionization electrons in all directions, affecting the resolution of the position measurement of the track. Diffusion along the drift direction is referred to as *longitudinal diffusion*, and diffusion perpendicular to the drift direction is referred to as *transverse diffusion*. For TPCs in a magnetic field (such as the ND280 TPCs), the magnetic field is oriented parallel or antiparallel to the electric field. As a result, any transverse diffusion has the Lorentz force acting to counter it, bending the ionization electrons back towards the straight line between their production point and the readout plane. The magnetic field therefore helps reduce the magnitude of the transverse diffusion.

Once the ionization electrons have drifted to the end of the TPC (i.e. through the *drift region*), they have arrived at the readout plane. The electrical signal produced by the small amount of charge of the ionization electrons alone would be highly susceptible to electrical noise, so amplifying the signal in the gas is desirable. The ND280 TPCs accomplish this amplification and subsequent readout using *Micromegas modules* [39, 23]. Each Micromegas module consists of a fine wire mesh (the *micromesh*) suspended 128 μm above charge readout pads. The wire is biased to -350 V, relative to the grounded pads. This results in a 27.4 kV/cm electric field between the micromesh and the pads (the *amplification region* of the detector). This region of intense electric field accelerates the electrons within it sufficiently to create a cascade of ionizations of the gas. This produces a *gain* of approximately 2000 (i.e. each ionization electron arriving at the Micromegas results in approximately 2000 electrons collected by a pad.) In addition to the gas composition, the gain is dependent on the density of the gas, and therefore its temperature and pressure. Variations in gain are mostly from atmospheric pressure variations, which are measured and corrected for in calibrating the TPCs.

After being collected in the pads, the charge signal of each pad (including its arrival time) is digitized by the readout electronics and stored. Once ND280 data collection for a given run period is complete, it undergoes processing, which includes applying calibrations, and use of an algorithm to reconstruct the particle trajectories using the pad positions, charge arrival times, and information on position and timing

from other ND280 subdetectors. The amount of charge collected by the pads is used to identify the particle that produced the track. How this is done is discussed in the next section.

A full discussion of the spatial and momentum resolution of the TPCs is given in [10]. To give a rough summary of the figures therein, the spatial resolution per column of pads is typically 0.7 mm, and the transverse momentum resolution is typically 10% at 1 GeV/c. An example event display is shown in Figure 4.1.

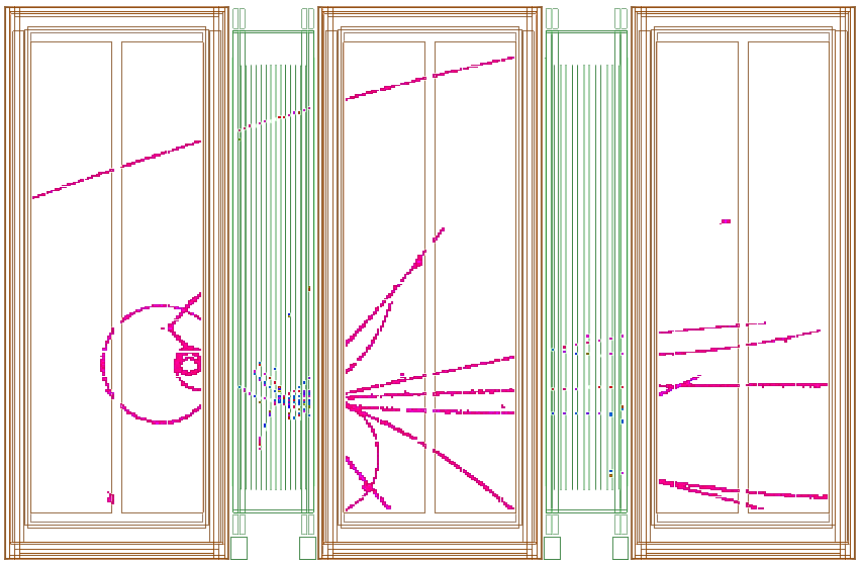

Figure 4.1: An event display including the three TPCs (in light brown, TPC1 on the left, TPC2 in the middle, and TPC3 on the right) and the two FGDs (in green, FGD1 between TPC1 and TPC2, and FGD2 between TPC2 and TPC3), where the beam would be coming in from the left. In this event, there was one neutrino interaction in front of TPC1, producing the track coming in at top left. A second neutrino underwent a deep inelastic scatter interaction near the bottom of FGD1, the resulting particles producing many tracks of different momenta (and therefore curvature in the magnetic field). The neutrino interactions selected for study in Chapter 5 would typically involve a smaller number of particle tracks. From [10].

4.1.3 Particle identification in the TPCs

As discussed in Section 4.1.1, the expected number of ionization electrons produced along the track of a charged particle in the TPC is a function of its speed. These ionization electrons are drifted to the Micromegas modules, which amplifies this charge proportionally to a signal suitable for the readout electronics. In this way, the TPCs

can measure the dE/dx of the charged particles passing through it. A comparison of dE/dx values reconstructed in data, and the expected values for each particle type are shown in Figure 4.2.

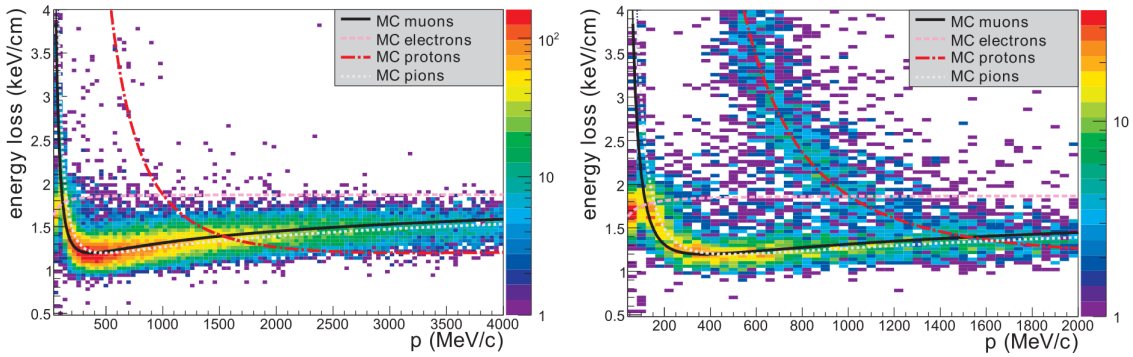

Figure 4.2: Comparison of dE/dx as a function of momentum, measured with neutrino beam data by the TPCs for negative particles (left) and positive particles (right), with the expected value for each particle shown for comparison. From [10].

Once the dE/dx value for a reconstructed particle track has been determined, it is compared to the expected value for various particle types (electron, muon, proton, and pion) through a quantity called the *pull*, defined in Equation 4.1 [32], where $(dE/dx)_{meas}$ is the measured dE/dx for the reconstructed track, $(dE/dx)_{exp,i}$ is the dE/dx expected for particle of type i at the measured momentum, and $\sigma_{(dE/dx)_{exp,i}}$ is the uncertainty in the expected dE/dx for a particle of type i at the measured momentum.

$$\delta_E(i) = \frac{(dE/dx)_{meas} - (dE/dx)_{exp,i}}{\sigma_{(dE/dx)_{exp,i}}} \tag{4.1}$$

That is to say, the pull gives the number of standard deviations the measured dE/dx is from the expected value for a particle of type i. An important example is shown in Figure 4.3. There the electron pull is calculated for a sample of through going muons. The probability of identifying a muon as an electron is 0.2% for $-1 < \delta_E(e) < 2$, for tracks below 1 GeV/c. This demonstrates that the TPCs can differentiate well between muons and electrons in the momentum region of most particles travelling through the TPC. So, for example, intrinsic ν_e in the beam that interact via Charged Current processes would be distinguished from ν_μ CC interactions.

In order to use the pulls to determine which of the different particle hypotheses for the reconstructed track is most likely, the pulls are used to calculate a statistic,

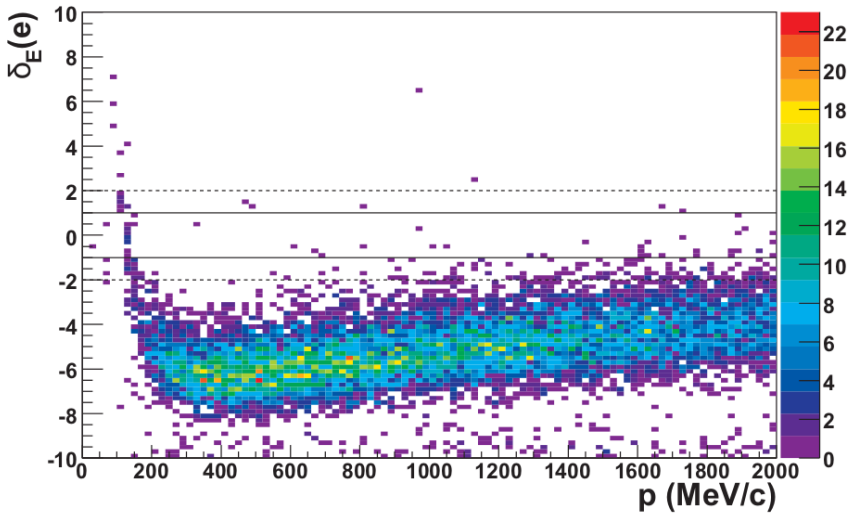

Figure 4.3: The electron pull as a function of momentum for a sample of through going muons, demonstrating a good capability to reject the electron hypothesis for true muons for $-1 < \delta_E(e) < 2$. From [10].

L_i, as shown in Equation 4.2 [32].

$$L_i = \frac{e^{-(\delta_E(i))^2}}{\sum_\ell e^{-(\delta_E(\ell))^2}} \tag{4.2}$$

The statistic is calculated for each hypothesis (muon, proton, electron, and pion), where the denominator is the sum over each of these hypotheses. The sum of the statistics for each hypothesis is therefore equal to 1. In making the event selections described in Chapter 5, cuts based on these statistics were determined based on their ability to properly identify simulated particles, and a systematic uncertainty was assigned to account for possible mis-modelling of the detector response.

4.2 Detector configuration

As shown in Figure 3.5, ND280 contains 3 TPCs having the same design:

- TPC1 between the P0D and FGD1.
- TPC2 between FGD1 and FGD2.
- TPC3 between FGD2 and the Downstream ECal.

A simplified cut-away drawing of the TPC design is shown in Figure 4.4. Each TPC has an Inner Volume (IV) and an Outer Volume (OV). The exterior of the OV is made of aluminum and aluminum/rohacell laminates, and is electrically grounded. The OV of each TPC is constantly flushed with CO_2 at a rate of 2.0 l/min. The CO_2 has a sufficiently high breakdown voltage to act as an electrical insulator for the high voltages used in the IV, and any CO_2 that diffuses into the IV can be easily removed, as discussed in Section 4.3.3.

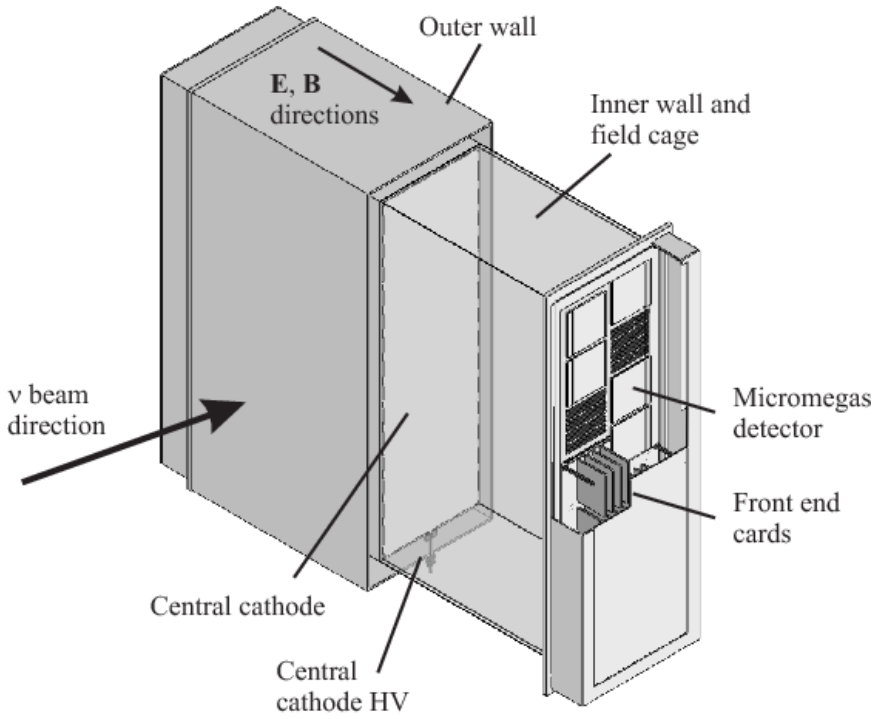

Figure 4.4: A cutaway drawing showing the structural components of a TPC. The outer box has exterior dimensions 2302 × 2400 × 974 mm ($x \times y \times z$ in the coordinate system shown in Figure 3.5), and the inner box has exterior dimensions $1808 \times 2230 \times 854$ mm, excluding the Micromegas module frames. Along the neutrino beam dimension (z), the interior dimension of the inner box is 772 mm. The distance between the central cathode and the Micromegas modules (i.e. the maximum drift distance) is 897 mm. From [10].

The IV is further subdivided into two separate volumes, separated by the central cathode. During normal operation, a voltage of -25 kV is applied to the central cathode. The IV walls are made of G10 and G10/rohacell laminates, and are covered with a series of copper strips, which run around the walls of the TPC, parallel to the

central cathode. The strips are electrically connected via precision resistors. This configuration is a voltage divider, and creates a nominally uniform electric field along the drift direction.

The IV is filled with a mixture of 95% argon, 3% CF_4, and 2% isobutane, and is kept at a pressure of 0.4 mbar $\pm$ 0.1 mbar above the OV pressure, with a constant input flow rate of 10.0 l/min, and a variable output flow rate. The motivations for the IV gas mixture and the details of the Gas Handling System are discussed further in Section 4.3.

Finally, at each end of the IV are 12 Micromegas modules. They are positioned in two columns which are vertically offset from each other, so that the gaps between modules (i.e. a dead region oriented in the same direction as the tracks to be measured) are not aligned between the two columns. Each Micromegas module is subdivided into 48 rows of 36 pads, for a total of 1728 pads, of which a 2 pad equivalent area in one corner is reserved for the voltage supply, and 1726 pads are used for the charge collection readout, providing good spatial resolution for track reconstruction.

Operation with a differential pressure of up to 5 mbar between the Outer Volumes and atmosphere was indicated to be structurally possible by tests. In order to ensure that overpressures or underpressures sufficient to damage the TPCs cannot occur, each TPC Inner and Outer Volume input and the combined Inner and Outer Volume outputs are protected by a device called a *bubbler* (for a total of 8 bubblers). A bubbler relies simply on a glass tube submerged in a low vapour pressure liquid (in this case dibutyl phthalate) to a depth corresponding to the pressure at which pressure relief is required. This entirely non-mechanical device therefore provides a way to ensure that damaging differential pressures do not occur (for example, due to device malfunctions) by either bubbling out gas on an overpressure, or bubbling in air on an underpressure.

During experiment shutdown periods where the TPCs are not in use, they are put into *Standby Argon Mode*. In this configuration, approximately 0.25 l/min of argon is flowed into each of the Inner and Outer Volumes and then out to exhaust at ground level. This mode of operation is maintained solely with manually operated devices, and therefore operates even in the absence of power. The purpose of this mode of operation is to keep the TPCs clean and dry for their next use (otherwise the bubblers would suck in ambient air from the service level as atmospheric pressure fluctuations required).

4.3 Gas Handling System

As discussed earlier in this chapter, the function of the TPCs is dependent in many ways on the properties of the gas they contain. The gases the TPCs depend on are provided by the Gas Handling System, made up of multiple components. In this section, the important components and their functions are discussed, along with their impact on the operational goals of the TPCs. Where it is necessary to include pressure setpoints and values, the unit *barg* denotes a pressure relative to atmospheric pressure, *bara* denotes an absolute pressure relative to a vacuum (i.e. ambient atmospheric pressure is approximately 1 bara, or 0 barg), and if the pressure is a differential pressure between two volumes, the pressure difference will be expressed in bar. A simplified schematic of the Gas Handling System is shown in Figure 4.5.

4.3.1 Inner Volume gas composition and supply

The gas mixture chosen for the TPC Inner Volumes is a mixture of 95% argon, 3% CF_4, and 2% isobutane. This mixture has a high drift velocity, low transverse diffusion, and the Micromegas modules work well with it. Each of the gas components plays a specific role in the operation of the TPCs. Argon makes up the majority of the gas mixture. It has a low primary ionization energy (15.8 eV), which encourages the production of ionization electrons. Also, as a noble gas, its full shell of electrons means that other argon atoms in the gas volume are unlikely to attach to drifting ionization electrons. Finally, as the third most abundant constituent of air, argon is reasonably low-cost to purchase.

CF_4 increases the drift velocity and reduces the transverse diffusion, and both CF_4 and isobutane play a role in the process known as *quenching*. In addition to ionization, the argon atom could instead receive only enough energy (11.6 eV) to enter an excited state. A photon is produced in the deexcitation that follows, which is capable of producing additional electrons by ionizing both the central cathode and the Micromegas wire mesh. If more ionization electrons are produced in the Micromegas wire mesh by photons produced in amplification process, new cascades will continuously be started, producing continuous discharge throughout the detector. At best this would blind the detector to subsequent particle tracks travelling through it, and at worse even damage the equipment.

In order to prevent this from happening, polyatomic gases (referred to as *quench gases*) are added to the gas mixture, which can absorb the photons and dissipate the

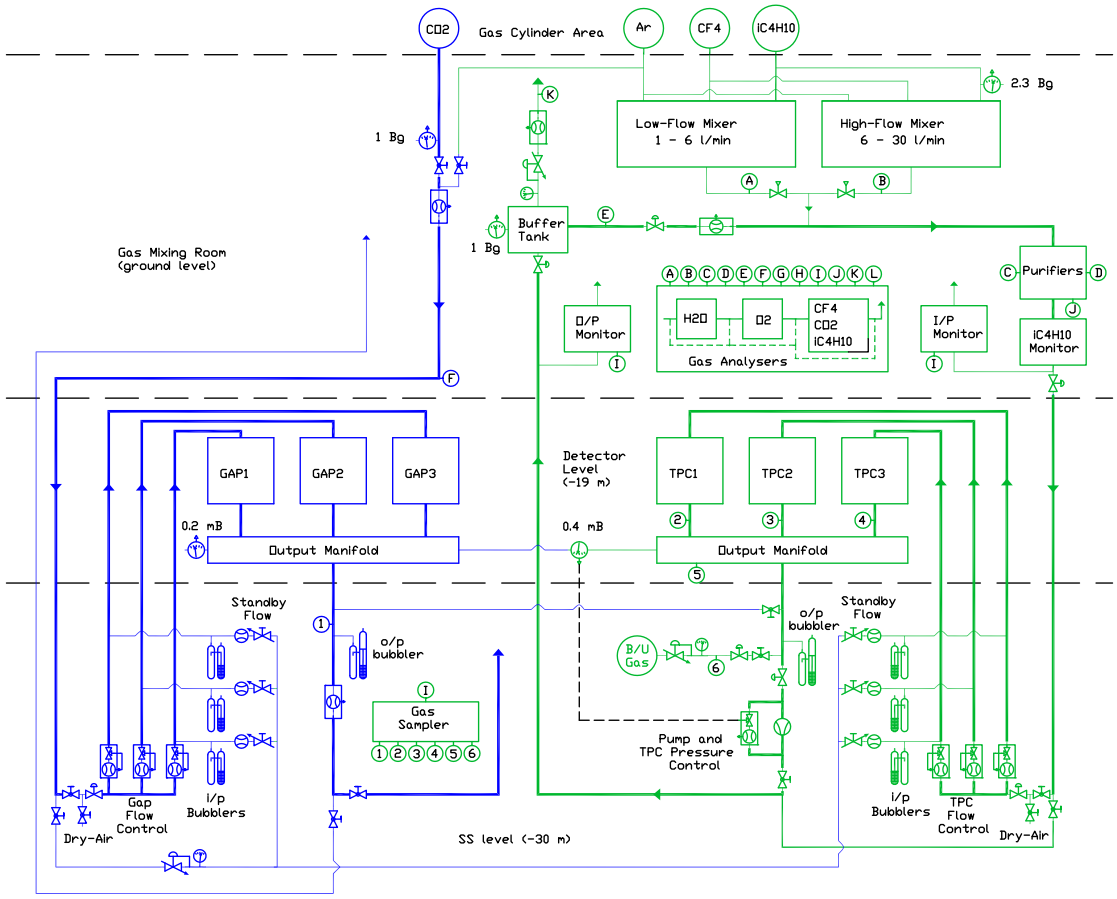

Figure 4.5: A simplified schematic of the Gas Handling System. From top to bottom, the dashed lines separate the schematic based on the location of the equipment: gas cylinder bays, the mixing room at ground level, the detector level, and the service stage level. On the left (in blue) is the part of the system servicing the Outer Volumes (*Gaps*) and on the right (in green) is the part of the system servicing the Inner Volumes. From [10].

energy through dissociation or elastic collisions. It is this role that CF_4 and isobutane perform in the ND280 TPC gas, with isobutane required as a quench gas for use of the Micromegas modules.

During normal operation, each TPC Inner Volume is supplied a constant flow of 10 l/min of this gas mixture, for a total of 30 l/min. The gas mixture is prepared onsite from separate supplies of argon, CF_4 and isobutane, mixed together with mass flow controllers. During normal operation, a 3 l/min flow of fresh mixed gas is supplied by mixing 2.85 l/min Ar, 0.09 l/min of CF_4 and 0.06 l/min of isobutane, which is combined with 27 l/min mixed gas from the TPC Inner Volume outputs (a 90%

recycling rate.) This configuration ensures that diffusion of nitrogen (from air) into the mixed gas does not build up to levels that would affect the gas properties, while keeping gas costs reasonably low. As discussed in Section 4.3.5, the TPC Inner Volume output flow rate is variable as a function of ambient pressure conditions, so a buffer tank is included in the recirculation loop to provide a reservoir of gas to draw from should the output flow drop temporarily below the 27 l/min required for this operating mode. Also present are a second set of higher flow but less precise mass flow controllers capable of providing the full 30 l/min flow. They are used to purge the Inner Volumes to transition from Standby Argon Mode to the normal gas mixture.

4.3.2 Support subsystems

Some components of the Gas Handling System require additional design considerations in order for them to function properly. As a result, a subsystem for keeping the isobutane at the desired temperature, and another subsystem for supplying pressurized air are included in the Gas Handling System. Both these subsystems are described in this section.

Isobutane heating

As discussed in Section 4.3.1, the TPC gas mixture contains 2% isobutane. In order to ensure that the pressure drop across the mass flow controller is sufficient for it to operate properly, an interlock requires an isobutane supply line pressure of at least 1.6 barg. Regulators attached to each bottle have setpoints at 2.4 barg and 2.1 barg, so that a drop in pressure can be used to signal that a bottle has been depleted, with a "Warning" setpoint at 2.2 barg to notify the operator that this has occurred.

Argon and CF_4 are delivered in 47 l bottles pressurized up towards $\sim$150 barg. However, the vapour pressure of isobutane is sufficiently low at ambient temperatures that pressures higher than $\sim$2 barg result in the isobutane liquifying. Therefore, isobutane is delivered in bottles containing 10 kg of liquid isobutane, and the pressure the bottle supplies is the vapour pressure of isobutane at the temperature of the bottle. In order to attain the required pressures and ensure that isobutane does not condense in the supply lines, temperatures must be kept above 25°C, requiring a heating system for the isobutane bottles and the lines up to the mass flow controllers. Once the isobutane is mixed with the argon and CF_4, its partial pressure is low enough

that no heating of the mixed gas lines are required. J-PARC safety regulations also require that the isobutane bottles not be heated above 40°C.

The heating near the mass flow controllers is provided by electrical heating tape, which the control system uses to nominally keep the tubing near 30°C, turning the tape on and off according to the temperature measurement from a thermocouple. From the bottles to the equipment rack, a non-electrical heating method must be used, so that electrical devices are not located in the flammable gas storage room (to reduce the risk of explosion in the event of a leak). This is accomplished with nominally 45°C water, heated up in an adjacent room by a chiller, which acts as a heat pump, pumping heat from the air in the room into the water. Water is pumped from a reservoir through the chiller, and then divided off into three separate streams: one for each of the two isobutane bottles, and one for the tubing from the bottles to the mass flow controllers. This arrangement ensures that when a new, cold bottle is connected, the heating of the other bottle and the tubing is not compromised. Each bottle is sealed in a separate side of an insulated box, and its temperature monitored by the control system with a thermocouple, as well as separate mechanical thermocouple that will shut off the flow of water to a side of the box if its bottle reaches a temperature of 40°C. Additional thermocouples connected to the control system monitor the isobutane line temperature both in the flammable gas room and near the mass flow controllers, and are used as inputs to interlocks in the control system, shutting off the flow of isobutane if temperatures get too low.

Pressurized air supply

In addition to a supply of air being necessary for flushing TPC volumes prior to maintenance (to ensure a breathable atmosphere), the Gas Handling System contains many valves whose states are changed using pressurized air (between 4.0 barg and 4.5 barg). Two types of air-actuated valves are used in the gas handling system:

1. Air-actuated poppet valves: The air pressure moves a poppet that would otherwise be held in the default position by a spring. At the end of the poppet is a needle, that blocks the flow of gas when the valve is closed, and allows its passage when opened. Unlike solenoid valves, the air actuated poppet valves are resistant to being opened by application of a backpressure. They also have a lower purchase price and lower power requirements.

2. Air-actuated ball valves: The air pressure acts to rotate the ball mechanism of

the valve, countering a spring that would otherwise return it to its default state. These valves are on the main, high flow lines in the recirculating gas loop. They cost-effectively provide a large aperture (and therefore low resistance to high flow), and backpressures cannot affect their state.

In both of these cases, for each valve there is a small solenoid actuator controlled by the control system, which provides the compressed air to the valve as needed to change its state. The initial plan involved using bottled gas to supply the necessary pressure to actuate these valves, as it was thought that only a small amount of gas would be required on a fairly infrequent state change. However, during testing at TRIUMF the solenoid actuators were discovered to leak at approximately 130 cc/min/valve. This amounts to approximately 6 l/min leaking from this system to supply the valves at ground level alone, which is a flow rate high enough to drain a standard 47 l bottle pressurized to 15 MPa in less than a day. A more cost-effective solution was therefore desired.

By the time of system installation in 2009, such a pressurized dry air supply was available on the service level of the ND280 pit (shown in Figure 3.3). This system consists of an oil-less dry air supply meant for use in a dental practice, which supplies dry air to the ND280 subdetectors, to protect them from the otherwise high humidity ambient air at J-PARC. The TPC Gas Handling System components on the service level were therefore connected into this system, using a regulator to bring the pressure down to the desired range, and drawing a miniscule flow rate of air in comparison to the dry air needs of ND280.

However, a large fraction of the Gas Handling System devices are located at ground level, where no supply of pressurized air was available. From commissioning in 2009 until early 2014, this air was supplied with an oil-less air compressor meant for painting applications (acquired at a local hardware store), whose output was attached to a simple filter/dryer. After a few years of successful operation the original unit had failed, and its replacement had inexplicably shut down during normal operation not long after. Since failure of the compressed air supply results in the TPCs being shut down and stoppage of data taking, a change to this configuration was contemplated in order to improve its reliability. Ultimately, the following improvements were made in 2014:

- A more robustly-constructed oil-less air compressor, designed for constant operation in industrial applications, was purchased, along with a spare.

- The water drainage output of this air compressor was connected to an auto-drain device, which prevents water from building up inside the tank, and does so without compromising the supply pressure of the air compressor.

- A backup bottle of dry air was purchased and connected into the system. Its regulator is set to deliver sufficient pressure to operate the valves, but far enough below that supplied by the compressor that an alarm would alert personnel in the control room that it was supplying air instead of the compressor. Should the compressor fail, it would be possible to swap in the spare air compressor without any interruption in data taking.

This improved system therefore provides greater reliability and the ability to remedy any malfunctions before they affect detector operations.

4.3.3 Purification

With 90% of the gas sent to the TPC Inner Volumes recycled, the issue of maintaining its purity requires some consideration, since contaminants can affect the properties of the gas, and therefore the operation of the detector. Although the Inner Volumes are kept at a positive pressure relative to the Outer Volumes, CO_2 can still diffuse from the Outer Volumes to the Inner Volumes. In addition, air can diffuse through fittings elsewhere in the system, introducing nitrogen, oxygen, and water vapour into the gas. Nitrogen is sufficiently inert that it cannot be removed, so its levels are kept down with the input of fresh gas. However, there are options for removing the other gases, which the Gas Handling System makes use of.

The removal of CO_2 and H_2O from the gas is accomplished by adsorbing it to a highly porous material, the ceramic 5A Molecular Sieve. As for O_2, it is removed from the gas by its participation in the oxidation of the activated copper catalyst BASF R3-11. To include these materials in the gas stream, 9.6 l of molecular sieve and 5.4 l of R3-11 are placed inside each of two stainless steel cylinders, and referred to as the *purifiers*. Each purifier's temperature is controlled using thermocouples and electrical heaters, and they are thermally insulated. During normal operation, one of the purifiers is in use, downstream of where the recycled and fresh gas mix together, and its temperature kept at 24°C. Having two purifiers allows the second to be regenerated, which is accomplished by heating it up to 180°C and flowing clean argon through it (to knock the CO_2 and H_2O from the molecular sieves) and subsequently flowing a

mixture of argon and up to 10% hydrogen, to reduce the oxidized R3-11, removing the oxygen in the form of water. The purifiers are not, however, solely specific to contaminants, and will also absorb CF_4 and isobutane, but thankfully only up to a maximum amount. The purifier therefore must be pre-saturated in CF_4 and isobutane before being used during normal operation. This is currently accomplished by inserting a fresh purifier at the beginning of the purge transition from Standby Argon Mode to normal operation (with saturation of both gases occurring approximately 75 minutes into the purge), though a dedicated procedure for pre-saturation using system exhaust also exists.

In practice, CO_2 levels were found to rise toward approximately the 100 ppm limit specified as acceptable, and level off there due to the diffusion rate into the Inner Volumes matching the removal rate from the addition of fresh gas. Since stable CO_2 levels are more conducive to stable detector operation than a level steadily rising then suddenly dropping to zero with the insertion of a new purifier, regenerated purifiers are only inserted at the start of a running period. In addition, O_2 levels have never been significant, and after a few years of operation the dry gas input coupled with the dessicating effect of the purifiers has removed most residual water from the TPCs, leading to H_2O levels below 1 ppm.

4.3.4 Composition analysis

Monitoring gas composition is an important part of ensuring good gas quality and ensuring that the TPCs are operated safely. To this end, the Gas Handling System contains four analyzers: an isobutane safety monitor, a water analyzer, an oxygen analyzer, and a multigas analyzer. Each of these analyzers is discussed below.

With the exception of the isobutane safety monitor, the analyzers can sample from multiple locations in the Gas Handling System. In practice, they spend most of their time sampling the gas recirculating from the TPC Inner Volumes, with a 2 hour period each day spent monitoring the gas at the output of the purifier that is in use, monitoring the purifier performance. Both sampling regimes use a flow rate of 0.5 l/min.

Isobutane safety monitor

The isobutane safety monitor is a General Monitors IR-2100, which was formerly used in the BaBar experiment. It is placed downstream of the purifiers, right before gas is

sampled by the monitor chambers (described in Section 4.4.1). It uses characteristic infrared absorption of the carbon-hydrogen bonds in isobutane to measure the percentage of isobutane in the gas flowing through it. This percentage measurement also includes temperature and pressure corrections performed inside the control system.

The measurement of this safety monitor has two important interlock levels associated with it. J-PARC safety regulations prohibit sending a gas mixture containing in excess of 3% isobutane to the TPCs. Alternatively, if the gas mixture were to contain less than 1% isobutane, the Micromegas modules could be damaged, as discussed in Section 4.3.1. Therefore, the isobutane safety monitor's reading would stop the flow of gas to the TPCs in both of these cases.

Water analyzer

The water analyzer is a Manalytical Pico-View, which uses a solid state sensor to measure H_2O levels ranging between 0 ppm and 1000 ppm. Although it has presented no trouble in its operation, if the sampling tubing has not been exposed mostly to dry gas, then diffusion of water in from the air can cause readings to be high until the tubing is dried sufficiently. Normal monitoring of the recycled gas and of the gas at the purifier output does not present this problem, but this is a concern for sampling from other areas of the system or checking this analyzer's calibration.

Oxygen analyzer

The O_2 molecule is highly electronegative, and its presence in the TPC gas in excess of 10 ppm would have a significant impact on the performance of the TPCs by attracting and binding to ionization electrons. The main source of oxygen in the TPC gas is from air diffusing through fittings, though a rise in oxygen content could indicate the development of a leak somewhere in the system.

The original oxygen analyzer in the Gas Handling System was a MecSens Series 511. It used an electrochemical method to measure the oxygen content of the gas, and was capable of making measurements from the ppm level up to the percentage in air. This range allowed for both monitoring of normal operation, and measuring breathability prior to opening the TPCs for maintenance. This analyzer's electrochemical technique also required regular cleaning of the electrodes, which was performed by a dedicated electronic cleaning station. In October 2012, the electrodes had degraded sufficiently that the cleaning station could no longer function. Neither repair nor

replacement was possible, as the product line had been discontinued as part of the sale of the manufacturer.

Based on past TRIUMF experience with their reliability, plus general availability of used units at low cost, a used Delta-F FA31110A was purchased, tested at the University of Victoria, then tested, commissioned, and its calibration verified in Japan in May 2013. Since operational experience deemed the measurement of oxygen at the $\sim$ 20% level to be non-crucial, its maximum possible oxygen measurement of 10000 ppm was deemed sufficient. Its electrochemical technique (likened to a fuel cell) does not produce a requirement for electrode maintenance. The only regular maintenance required is periodically topping off its electrolyte reservoir with distilled water.

Multigas analyzer

The multigas analyzer is an ADC MGA-3000, designed to be capable of measuring CO_2 contamination as well as the isobutane and CF_4 content of the gas. Like the isobutane safety monitor, it was designed to do so using the characteristic infrared absorption of the molecular bonds in each of these gases. In practice, it required an extensive set of polynomial corrections to be applied, based on the content of the other gases and on pressure and temperature conditions. Even then, the isobutane reading was deemed completely untrustworthy, to the point of using a fixed value of 2% or the isobutane safety monitor reading as the input to the correction calculations. Its monitoring of CO_2 and CF_4 has nonetheless been found to be fairly accurate, and provided reasonable measurements of gas quality.

4.3.5 IV-OV differential pressure control

Since the properties of the gas needed for accurately reconstructing events are pressure dependent, it is important to understand the pressure inside the TPC Inner Volumes. How this is accomplished is described below.

As discussed earlier, the flow rates into each TPC Outer Volume are the same, and the flow rates into each TPC Inner Volume are the same. The outputs of the Outer Volumes are linked together into a manifold, and the Inner Volumes outputs are linked together into a separate manifold, in both cases via wide diameter tubing, so measuring the pressure at the manifold effectively measures the pressure of the corresponding 3 volumes.

During normal operation, the Outer Volume exhaust is connected to a vent that is below the centre of the TPCs by 7 m. At this 6 l/min flow of normal operation, this produces a differential pressure between the Outer Volumes and atmosphere of approximately 0.2 mbar, due to a combination of the resistance in the tubing and the negative pressure head due to the lower elevation. A small positive pressure relative to atmosphere is therefore maintained (so that air is not drawn into the Outer Volumes), while the much larger pressure head required to exhaust 22 m up to the surface (1.3 mbar, due to the weight of the CO_2) is avoided.

The configuration of the Inner Volumes is more complicated. The need to recirculate gas places a requirement that at some point the TPC Inner Volume output reach a pressure of ~ 1 barg, which is the normal line pressure, required for the TPC input mass flow controllers to reliably supply flow to the TPC Inner Volumes with a pressure near 0 barg. To create this higher output pressure, a pump is used. However, fluctuations in atmospheric pressure would produce fluctuations in the Inner Volume pressure, which the constant action of the pump would be unable to moderate. Therefore a mass flow controller is used to flow gas back from the output of the pump towards the Inner Volume output manifold. How wide the solenoid valve of the mass flow controller is opened is determined by a PID (Proportional-Integral-Derivative) algorithm coded into the control system, taking input from a pressure transducer measuring the differential pressure between the Inner and Outer Volumes, and with desired setpoint of 0.400 mbar. However, since there is a delay inherent in communication with the mass flow controller, the resulting discontinuity in the solenoid setpoint was found to produce instability with the Derivative component (*how fast the pressure is changing*), so only the Proportional (*how far the pressure is from the setpoint*) and Integral (*how far the pressure has been adjusted so far*) components of the PID algorithm are used. The tuning was devised through trial and error in testing at TRIUMF and after installation at J-PARC. This pressure control system keeps the differential pressure between the Inner Volumes and Outer Volumes at 0.400 mbar $\pm$ 0.100 mbar, therefore ensuring the stable pressures needed for stable detector operation. The differential pressure requirements are primarily motivated by mechanical concerns. The differential pressure must be kept stable to within 0.100 mbar to keep the walls and the readout plane mechanically stable. The setpoint value of 0.400 mbar was chosen to be comfortably above 0 bar in order to ensure that CO_2 is not drawn into the Inner Volume. However, the maximum differential pressure between the IV and OV needs to be kept below 1 mbar to prevent

breaking joints.

4.3.6 Control system

In order to provide the functions described in the previous sections, the Gas Handling System contains more than 250 devices, including valves, flow meters and controllers, pressure transducers, gauges, and regulators, gas analysers, pumps, thermocouples, and heaters. Of these devices, approximately 170 of them accept an electronic signal for control, and/or provide an electronic signal for readback. These devices are connected into a Programmable Logic Controller (PLC) (Schneider Electric's Modicon Quantum platform), via various modules providing digital inputs/outputs, relay contacts for providing higher current power, analog inputs, or Modbus RTU.

Inside the PLC code, these inputs and outputs are associated with the corresponding devices, providing a platform for monitoring and controlling the devices. In addition, a comprehensive set of interlocks is included, in order to automatically prevent unsafe or undesirable operation of the devices.

The human interface to the PLC is provided with two separate software frameworks. The EPICS software package is used to provide the graphical user interface. The EPICS interface is laid out in approximately the same way as the system schematic, but providing buttons for device control, numerical fields for setpoint values, and coloured status and numerical readouts for devices as appropriate. Each device also has a *detail panel* associated with it, providing a visual representation of the interlocks affecting the device, and the ability to open the detail panel of any device participating in the interlock. The MIDAS ND280 slow control software also pulls information from the PLC. It provides a long term history of device readback values, a display resembling the system schematic, as well as a link into the ND280 Control Room alarm framework, with various alarms set to alert detector operators to problems with the Gas Handling System.

In combination, the PLC and its EPICS and MIDAS interfaces provide automated control of the system, the opportunity for operator input, and constant monitoring of system conditions. This allows the TPC Gas Handling System to maintain a solid record of stable operation in support of data taking.

4.4 Calibration systems

In order to make reliable measurements using the TPCs, the properties integral to their operation must be well understood. Two TPC subsystems help accomplish this: the Gas Monitor Chambers and the Laser calibration system.

4.4.1 Gas Monitor Chambers

The Gas Monitor Chambers are two "mini-TPCs" installed amongst the ground level components of the Gas Handling System where gas is mixed. They are each 1 l in volume, and are designed to have the same drift field as the TPCs. The Micromegas modules they use are smaller than that of the TPCs, but were produced the same way. One of the Gas Monitor Chambers samples the gas being sent down to the TPCs, and the other samples the gas returning from the TPCs. Both do so at a rate of 0.1 l/min, which corresponds to a full volume change every 10 minutes. The ambient pressure and temperature are also monitored, as these affect the gas properties as well.

One of the properties measured by the Gas Monitor Chambers is the gas gain. This is accomplished by using a ^{55}Fe x-ray source. ^{55}Fe decays into ^{55}Mn by electron capture, that is, an electron from its electron shell and a proton from the nucleus undergo the process $p + e^- \rightarrow n + \nu_e$. In the resulting reorganization of the electron shell, an x-ray is sometimes emitted, at an energy of 5.9 keV. When an x-ray interacts inside the gas, it tends to deposit all of its energy inside the Gas Monitor Chamber, producing a known number of electrons. These electrons drift to the Micromegas, and the resulting signal is recorded. This occurs multiple times over a 10 minute period, and the resulting distribution is compared to the expected number of electrons from the 5.9 keV x-ray, and the gain is calculated.

The other gas property measured is the drift velocity. This is accomplished by using two ^{90}Sr sources, placed above the chamber at different distances from the Micromegas module along the length of the chamber. ^{90}Sr decays via β-decay to ^{90}Y. The resulting electron produces a track inside the chamber. If the electron reaches the scintillating fibre below the chamber directly below one of the sources, a drift velocity measurement is triggered. The two sources therefore produce two tracks with a well defined separation distance between them, perpendicular to the drift field. By comparing the drift times between the two tracks, the drift velocity is calculated.

4.4.2 Laser calibration system

Since reconstructing charged particle tracks relies on electrons drifting to the readout planes in a predictable way, it is important to understand the drift of the electrons, which can be affected by distortions in the electric and magnetic fields inside the TPCs. In addition, performing a measurement of the drift velocity inside the TPCs themselves is a useful cross-check to the measurement performed by the Gas Monitor Chambers. These measurements are performed by the laser calibration system.

The design element included in the TPCs for this purpose is a pattern of dots and strips on the central cathode, which is shown in Figure 4.6. The surface of the central cathode is made out of copper. The dots are 8 mm diameter circles of aluminum, glued to the central cathode surface. The strips are also made of aluminum, and are 4 mm wide, and allow measuring the transverse size of the ionization. An Nd:YAG laser is sealed in an equipment rack on the floor below the detector, and 18 quartz optical fibres are used to transmit the laser pulse to the TPCs. Each quartz fibre is positioned to illuminate a region of the central cathode measured by 4 Micromegas modules, and an electromechanical multiplexor changes the position of a mirror inside the laser rack to choose which optical fibre is used.

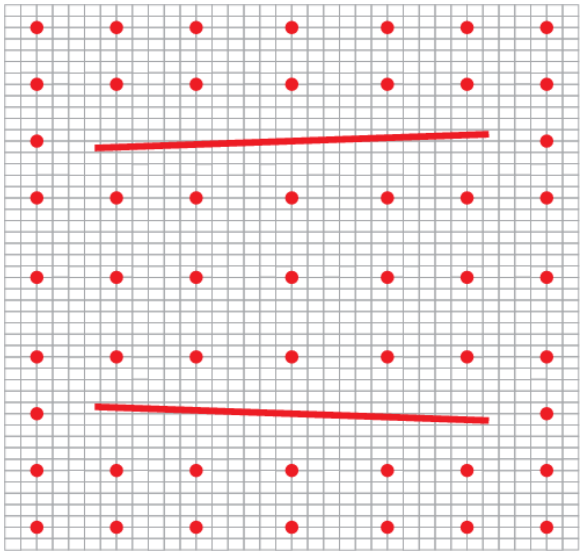

Figure 4.6: Pattern of aluminum dots and strips (for one Micromegas module) on both sides of the central cathode of the TPCs, which the laser calibration system uses to produce a corresponding pattern of photoelectrons for use in TPC calibration. The grid pattern gives the position of the pads, projected onto the central cathode. From [10].

A flash of 266 nm light produces electrons via the photoelectric effect in the aluminum dots, but not the surrounding copper. These electrons will drift to the Micromegas modules to be read out. Since the firing of the laser gives a definite time for the photoelectron emission, and the distance between the central cathode and the Micromegas is known, the time of the drift can be measured and used to determine the drift velocity. Electric and magnetic field distortions would affect the pattern of the dots and strips being reconstructed. The measured distortion of this pattern can be used to apply corrections to the reconstruction of events. The expected spatial resolution with approximately 100 photoelectrons per dot is better than 0.5 mm (dominated by transverse diffusion.)

Chapter 5

Event selection at ND280

The placement of ND280, 280 m from the beam target, results in a very high neutrino interaction rate, in comparison to Super-Kamiokande. This allows ND280 measurements to measure the neutrino beam flux, as well as to study how neutrinos interact with matter. In order to study neutrino interactions, ND280 events are selected into a number of samples meant to be dominated by the different interactions of interest. In this chapter, these samples and sources of systematic uncertainty are discussed.

5.1 Considerations

In Section 3.3.2, the ND280 detector was introduced as containing multiple subdetectors, with various design features meant to enable multiple types of measurements. The main considerations in defining the ND280 selections used for the neutrino oscillation analysis are that the selected samples are sensitive to the models for the neutrino beam flux (Section 6.2.2) and neutrino cross sections (Section 6.2.3), and that the systematic uncertainties related to the detector model are properly quantified.

As will be discussed in Section 6.2.2, the neutrino flavour composition of the beam is highly correlated between neutrino mode and antineutrino mode, and between the different neutrino flavours and energies. Therefore, any high purity large sample of muon neutrino or antineutrino interactions would be sufficient to constrain the flux model parameters.

For the cross section model, the overall goal of the ND280 measurement is to reduce uncertainty for the signal process (CCQE), and for the background processes (CCRES and CC 2p-2h being especially important, though other CC pro-

cesses and NC processes are present.) Therefore, restricting consideration to the easier-to-measure Charged Current processes goes a long way towards constraining signal and background, and any effort to separate out individual processes within this CC-Inclusive sample would better constrain the model parameters for the process, provided that a sufficiently large number of events is in the sample in question. Although there is some material dependence in the model, measurements of neutrino interactions on carbon at ND280 constrain many model parameters that also apply to interactions on oxygen at Super-Kamiokande.

Whether the data is being taken in neutrino beam mode or antineutrino beam mode is also important to consider in designing the ND280 selections. As the beam production process involves colliding positive particles (protons) with positive and neutral particles (protons and neutrons), there is a natural preference towards producing π^+ over producing π^- in the beam target. This leads to a ν_μ flux in neutrino mode that is 20% higher at its peak than the $\bar{\nu}_\mu$ flux in antineutrino mode, but also means that in antineutrino mode there are more high energy π^+ that the horns do not bend out of the beam. As a result, the *wrong sign* component of the antineutrino beam (i.e. neutrinos) is larger than the wrong sign component of the neutrino beam (i.e. antineutrinos).

In addition, neutrinos and antineutrinos have different cross sections for interaction with matter. The world data on the CC-Inclusive and CCQE cross sections for neutrinos and antineutrinos (Figure 49.1 and 49.2 respectively of [79]) show that the neutrino/antineutrino cross section ratio is about 2 at high energies, and about 4 at peak energy of the T2K energy spectrum. Antineutrino interactions are therefore suppressed relative to neutrino interactions.

As a result of these flux and cross section effects, the antineutrino background in neutrino mode is negligible, but the neutrino background in antineutrino mode is not. The neutrino background in antineutrino mode makes up an irreduceable background at Super-Kamiokande, since it cannot determine the charge of the lepton produced in the Charged Current neutrino interaction. Therefore, although it is reasonable to design the ND280 selection to assume that only neutrino interactions occur in neutrino mode, it is important for the antineutrino mode selection to attempt to distinguish between neutrino and antineutrino events.

Finally, there is the issue of detector systematic uncertainties. Advanced treatments of the systematic uncertainties in modelling FGD1 and TPC measurements of particle properties had been developed for earlier T2K analyses (such as [8]). Al-

though using other ND280 subdetectors would open up new possibilities for constraining models, at the time of this analysis the treatments of the systematic uncertainties had not advanced sufficiently to do so. The small amount of antineutrino beam mode data collected at Super-Kamiokande also suggested that the antineutrino oscillation measurement (discussed in Chapter 7) would be statistics limited. Therefore, pushing forward with the familiar ND280 neutrino mode event selection and antineutrino mode event selection, with well-understood detector systematic uncertainties, was deemed sufficient for this muon antineutrino disappearance analysis.

5.2 Neutrino mode event selection

The neutrino mode event selection [32] begins by selecting a sample of Charged Current ν_μ interactions, referred to as the *CC-Inclusive sample*. This involves performing a series of cuts on the event sample (be it data collected or simulated events). These cuts are outlined below.

1. **Data Quality Flag**: The slow control system for the ND280 subdetectors monitors their condition. If they are not in their normal configuration (for example, if readout electronics were off), a data quality flag is set to note this. The CC-Inclusive selection therefore begins by cutting out periods where this flag indicates bad data quality.

Each beam spill, consisting of 8 bunches of protons, is recorded by ND280 and the detector timing is sufficiently precise to distinguish these bunches. Therefore, to help avoid having multiple interactions in one event (referred to as *pile-up*), the spill is sub-divided into bunches, so that interactions in different bunches of the same spill are treated as separate events.

2. **Total Multiplicity Cut**: The precision measurements of momentum, charge, and particle identification performed by the TPC are required to perform a meaningful analysis. Therefore, at least one track reconstructed in the TPC is required.

3. **Leading Tracks and the Quality and Fiducial Cuts**: The tracks that are reconstructed to include segments in the TPC are considered, and two properties are checked:

- **Track Quality**: Reconstruction of short tracks in the TPC can be less reliable, so only tracks with more than 18 vertical or horizontal clusters in the TPC are selected. (A *cluster* is a group of Micromegas module pad signals above threshold close to each other in space and time. Clustering is discussed more in Section 5.4.8.)
- **Fiducial Cut**: The selection looks for interactions that occurred in FGD1. Therefore, in order to be selected, the track must contain an FGD1 segment, and the starting point of this track must be inside the FGD1 fiducial volume. The fiducial volume is a subvolume of the FGD1 sensitive area, excluding 5 bars from the edge of the XY modules (in x and y), and the first most upstream XY module (i.e. the one closest to TPC1) in z. Defining the fiducial volume in this way helps exclude interactions that occurred outside of FGD1.

Only tracks that satisfy these two criteria (henceforth *TPC-FGD1 tracks*) are considered further and the highest momentum negative TPC-FGD1 track is considered the *muon candidate* (i.e. the candidate for the muon produced in the Charged Current interaction). The reconstructed position of the neutrino interaction (the *vertex*) is then set to be the starting position of the muon candidate, and it is required to be in the FGD1 fiducial volume. This selection assumes that the muon direction is forward, along the neutrino direction.

4. **Upstream background veto**: Reject the event if the highest momentum track with a TPC component that is not the muon candidate starts 150 mm or more upstream (i.e. towards the P0D) from the start position of the muon candidate. This is meant to remove events where there is a reconstruction failure resulting in a muon track being reconstructed as beginning in the FGD1 fiducial volume, when in fact it originated far upstream.

5. **Broken Track Cut**: Reject the event if at least one FGD-only track was reconstructed, and the muon candidate track starts close to the downstream edge of FGD1. This is meant to exclude events where the reconstruction mistakenly breaks the muon candidate track (a TPC-FGD1 track) into an FGD1-only track and an TPC-FGD1 track that starts close to the downstream edge of FGD1. This is ultimately a fairly unlikely occurrence (this cut only excludes approximately 1% of events at this stage of the selection, according to Table 5

of [32]).

6. **Muon PID Cut**: Require that the muon candidate have a PID consistent with a muon (as discussed in Section 4.1.3).

After the CC-Inclusive sample has been obtained by applying the above cuts, it is further subdivided into three samples based on the number and charge of the pions that leave the nucleus: CC-0π, CC-1π, and CC-Other.

The CC-0π sample, selecting for events with no pions exiting the nucleus, should be enriched in CCQE events, and thus be especially sensitive to the CCQE model parameters. However, as mentioned in Section 2.2, this sample will also contain CC 2p-2h events, as well as CCRES and CC OTHER events where the pions did not escape the nucleus.

The CC-1π sample, selecting for events with one π^+ exiting the nucleus, should be enriched in CCRES (specifically, CCRES π^+) events, and thus be especially sensitive to the CCRES model parameters. As with the CCQE sample, CC OTHER events where some pions did not escape the nucleus should also be in this sample. In addition, the CCCOH events discussed in Section 2.2 would also be selected into this sample.

Finally the CC-Other sample includes all events with different pion content, though primarily the higher energy CC OTHER events.

In order to separate the events into these three samples, FGD1 and the TPC must be used to check for the existence and determine the charge of any pions in the event. There are 4 ways that the existence of a pion is inferred:

- TPC $\pi^{\pm}$: A TPC-FGD1 track (other than the muon candidate track) is identified as a $\pi^{\pm}$.

- TPC $e^{\pm}$: A TPC-FGD1 track is identified as an $e^{\pm}$. The $e^{\pm}$ track is assumed to be the result of a pair production ($\gamma \rightarrow e^+ + e^-$) from a photon produced by the decay of a π^0 ($\pi^0 \rightarrow \gamma + \gamma$) that was in the final state.

- FGD ME: A Michel Electron is detected in the FGD, which suggests that a pion stopped and decayed in the FGD, as discussed in Section 3.3.2. This can reasonably be assumed to be due to a stopped π^+, since stopped π^- tend to be captured by nearby positive nuclei.

- FGD π: A track is reconstructed in the FGD (but not the TPC) which the FGD identifies as a pion. This is assumed to be a π^+, as there is insufficient curvature

to identify the charge, and a low energy π^+ is more likely to be produced in a ν_μ interaction than a low energy π^-.

With the means of counting and identifying pions set, the selection into the three samples proceeds as follows.

- For the CC-0π sample, events must not contain any TPC $\pi^\pm$, TPC $e^\pm$, FGD ME, or FGD π.
- For the CC-1π sample, the following conditions must hold true:
  - There are no TPC π^-.
  - There are no TPC $e^\pm$.
  - There is 1 π^+ observed via one of the following two methods:
    * There is 1 TPC π^+ or 1 FGD ME. (Both of these methods are considered accurate individual ways to indicate the existence of a π^+, and if an FGD π were also found, it could very well be the pion that decayed to produce the FGD ME.)
    * There is neither an FGD ME nor a TPC π^+, but at least 1 FGD π. Any number greater than zero FGD π is allowed out of concern that the FGD reconstruction is more likely to break one pion track into multiple tracks than for there to be multiple low energy pions for which a Michel Electron is not tagged for at least one of them.
- The CC-Other sample includes all remaining cases.

The results of performing this selection on the default simulated event sample, in comparison to the data, are shown in Figures 5.1, 5.2, and 5.3. These figures show how the data compares to the default simulation (with updated beam flux model tuning), with the default simulated event sample broken down by the true event topology (i.e. the sample the event would be in if the detector could accurately determine all particles that left the nucleus, for all events.) This event selection is therefore reasonably successful at selecting the desired event topology. The breakdown into the interaction channels (CCQE, CCRES, etc.) is shown and discussed in Section 6.4.1.

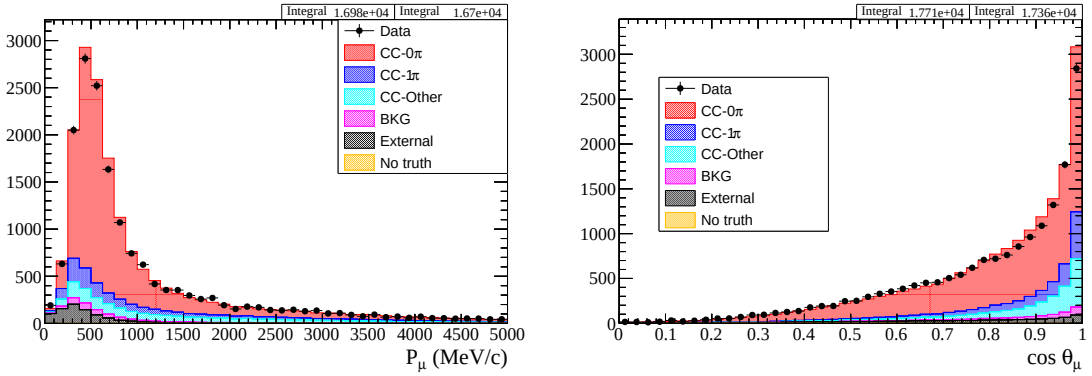

Figure 5.1: Momentum and angular distributions of events in the data and the default simulated event sample selected into the CC-0π sample (neutrino mode). The simulated event sample is subdivided by its true topology to demonstrate the extent to which other topologies are mis-selected into this sample. From [92] (T2K official plots associated with [32]).

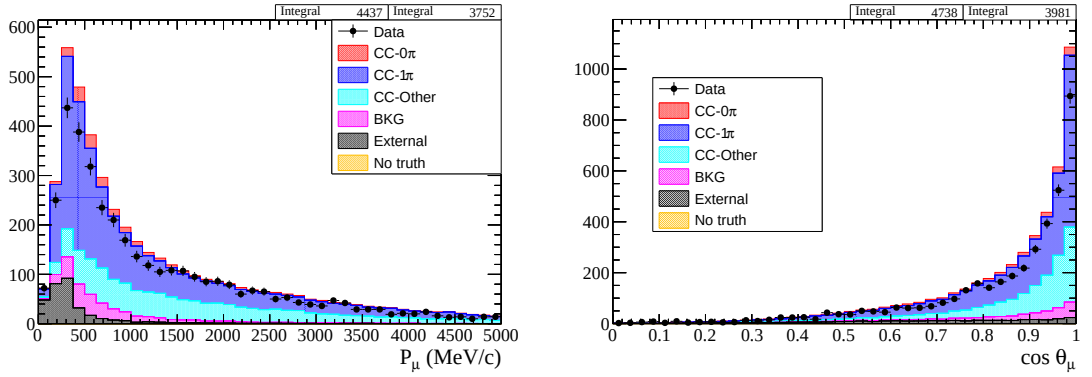

Figure 5.2: Momentum and angular distributions of events in the data and the default simulated event sample selected into the CC-1π sample (neutrino mode). The simulated event sample is subdivided by its true topology to demonstrate the extent to which other topologies are mis-selected into this sample. From [92] (T2K official plots associated with [32]).

5.3 Antineutrino mode event selection

As discussed in Section 5.1, in antineutrino mode it is important to attempt to distinguish between neutrino and antineutrino interactions, as beam flux and cross section considerations mean that neutrino interactions make up a non-negligible portion of the interactions at ND280. Therefore, two mutually exclusive selections are performed in antineutrino mode: one [35] beginning with a $\bar{\nu}_\mu$ CC-Inclusive sample, and the other [36] beginning with a ν_μ CC-Inclusive sample. These selections are nearly

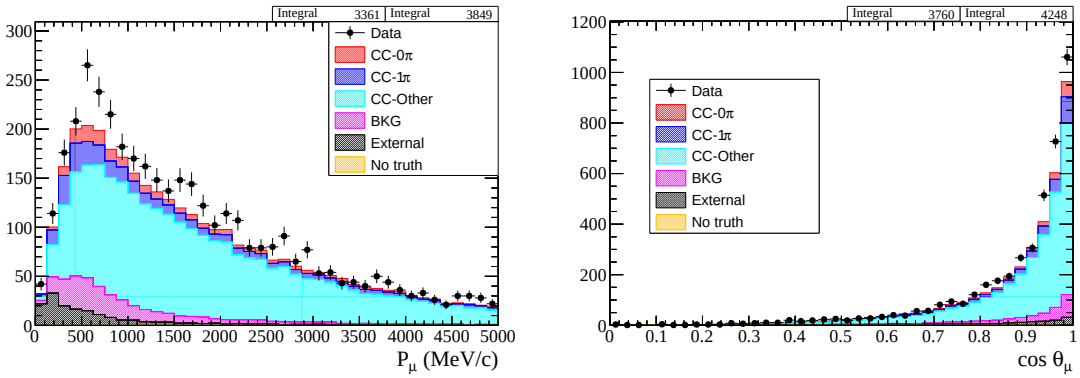

Figure 5.3: Momentum and angular distributions of events in the data and the default simulated event sample selected into the CC-Other sample (neutrino mode). The simulated event sample is subdivided by its true topology to demonstrate the extent to which other topologies are mis-selected into this sample. From [92] (T2K official plots associated with [32]).

identical to the neutrino mode ν_μ CC-Inclusive selection discussed in the previous section, but with a few important distinctions. The antineutrino mode $\bar{\nu}_\mu$ CC-Inclusive sample is looking for Charged Current $\bar{\nu}_\mu$ interactions, and therefore must find a μ^+ instead of a μ^-. Therefore, it is the highest momentum positive track that is the muon candidate in this selection, instead of the highest momentum negative track.

The only other difference with the neutrino mode CC-Inclusive selection is that after the "Leading Tracks and Quality and Fiducial Cuts" step, both the antineutrino mode $\bar{\nu}_\mu$ CC-Inclusive selection and antineutrino mode ν_μ CC-Inclusive selection insert an additional step that requires that the highest momentum TPC-FGD1 track in the event be the muon candidate track. That is to say, that for the $\bar{\nu}_\mu$ CC-Inclusive selection the highest momentum track must be positive, and for the ν_μ CC-Inclusive selection the highest momentum track must be negative. Since the outgoing charged lepton is usually the highest momentum particle produced in a Charged Current interaction, this is a reasonably effective way to decide whether an event is a $\bar{\nu}_\mu$ or ν_μ Charged Current interaction.

These two CC-Inclusive samples are each divided into two additional samples, CC-1-Track (enhanced in the signal CCQE process) and CC-N-Tracks (enhanced in the background processes), for a total of 4 antineutrino mode samples. As their names suggest, these selections are based on a simple counting of tracks using the TPC and FGD1. If there is one TPC-FGD1 track, the event is selected into the CC-1-Track sample. If there is more than one TPC-FGD1 track, the event is selected into the CC-

N-Tracks sample. This provides a reasonable amount of separation between the signal and background interaction processes, and for such small sample sizes, developing a more complex selection would not accomplish much more. For the $\bar{\nu}_\mu$ selection, this selection is made more accurate in that $\bar{\nu}_\mu$ CCQE takes the form $\bar{\nu}_\mu + p \rightarrow \mu^+ + n$, so (excepting FSI or reinteraction of the neutron), one would only expect one TPC-FGD1 track for CCQE, the μ^+. How these selections break down in terms of number of pions leaving the nucleus for the default simulation (with updated beam flux model tuning), in comparison to data, is shown in Figures 5.4, 5.5, 5.6, and 5.7. As with the neutrino mode samples, the breakdown into interaction channels is shown and discussed in Section 6.4.1.

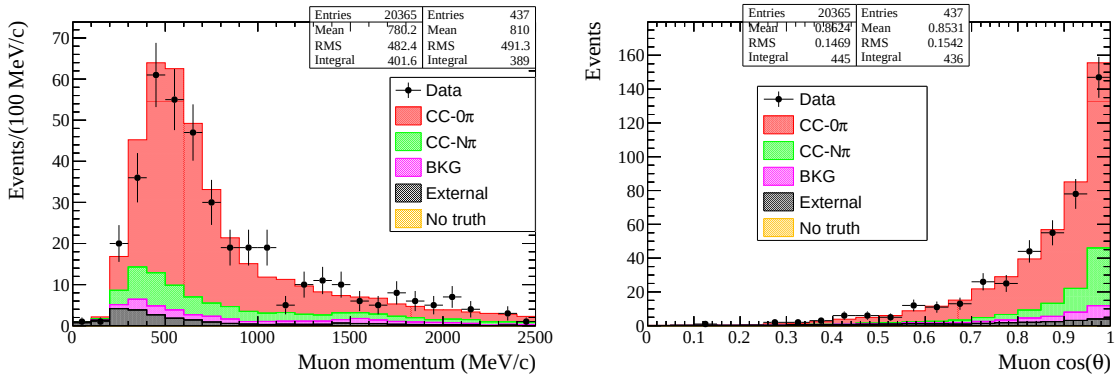

Figure 5.4: Momentum and angular distributions of events in the data and the default simulated event sample selected into the $\bar{\nu}_\mu$ CC-1-Track sample (antineutrino mode). The simulated event sample is subdivided by its true topology to demonstrate the extent to which other topologies are mis-selected into this sample. From [90] (T2K official plots associated with [35]).

5.4 Sources of systematic uncertainty

As will be discussed in Chapter 6, the event rates and distributions in each sample at ND280 depend on the beam flux and the cross sections for the various interaction channels. ND280 data are used to estimate flux and cross section model parameters in order to more accurately predict the unoscillated neutrino interaction rate at Super-Kamiokande. However, the event rates and distributions in these samples also depend on the properties of the ND280 detector itself. Therefore, it also important to consider the uncertainties in the detector model that are relevant to the measurement being

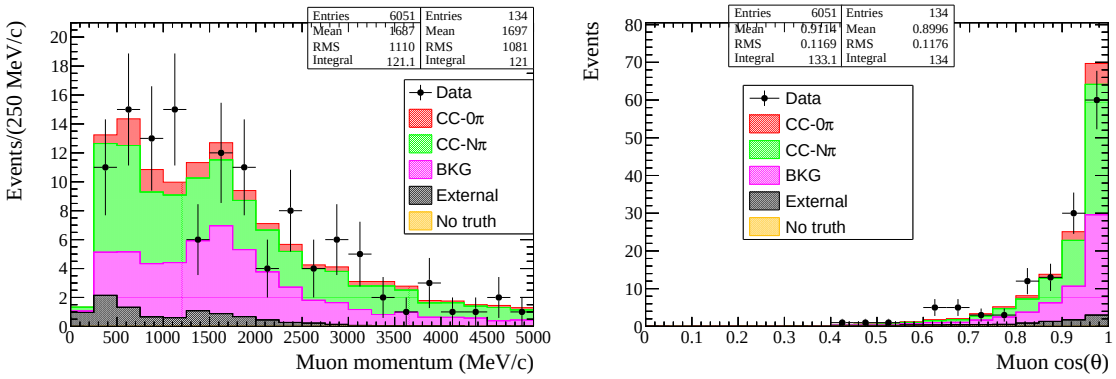

Figure 5.5: Momentum and angular distributions of events in the data and the default simulated event sample selected into the $\bar{\nu}_\mu$ CC-N-Tracks sample (antineutrino mode). The simulated event sample is subdivided by its true topology to demonstrate the extent to which other topologies are mis-selected into this sample. From [90] (T2K official plots associated with [35]).

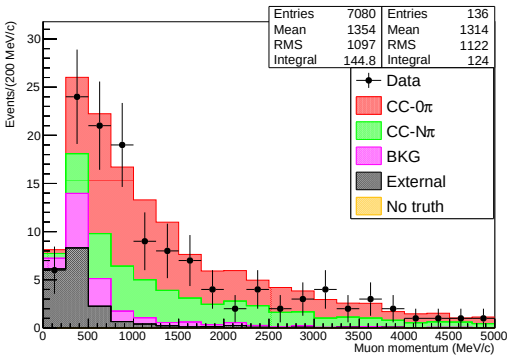

Figure 5.6: Momentum distribution of events in the data and the default simulated event sample selected into the ν_μ CC-1-Track sample (antineutrino mode). The simulated event sample is subdivided by its true topology to demonstrate the extent to which other topologies are mis-selected into this sample. From [91] (T2K official plots associated with [36]).

made. As these sources of systematic uncertainty originate from the detector model, they are collectively referred to as *detector systematics.*

These uncertainties are treated in two different ways, depending on the effect of the detector systematic. For *weight systematics*, weights are applied to events in the simulated sample, to mimic adjusting the detector properties in question. For *variation systematics*, an observable quantity in the event is varied (for example, the momentum of the muon.) Variation systematics have the added complication that they can change the outcome of the event selection. For example, since the selections

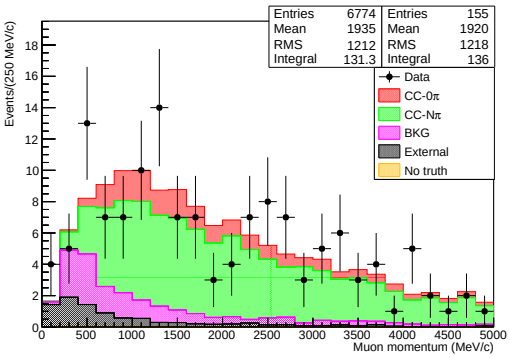

Figure 5.7: Momentum distribution of events in the data and the default simulated event sample selected into the ν_μ CC-N-Tracks sample (antineutrino mode). The simulated event sample is subdivided by its true topology to demonstrate the extent to which other topologies are mis-selected into this sample. From [91] (T2K official plots associated with [36]).

rely on the muon candidate being the highest momentum negative/positive track, a change in the muon momentum could change which track is identified as the muon candidate, and thus the selection outcome. Therefore, after variation systematics are applied, the selection must be rerun.

Each of the detector systematics [32] is described in more detail below, including how the size of the uncertainties were determined for each, and how they are modelled in the analysis. Their individual contributions to the uncertainty in the total event rate in each sample are given in Table 5.1 for neutrino mode samples, Table 5.2 for antineutrino mode antineutrino samples, and Table 5.3 for antineutrino mode neutrino samples.

5.4.1 Magnetic field distortions

The ND280 detectors are located inside the magnetic field provided by the magnet. This magnetic field curves the charged particle tracks in accordance with the Lorentz force law, allowing for the charge of a track to be determined, as well as a measurement of its momentum to be performed. Both of these observables are important to the selections described in the previous sections, as well as in measuring an accurate momentum distribution. It is therefore important that the magnetic field used in the detector model be as close as possible to the real magnetic field provided by the magnet, and the uncertainty quantified.

For the reconstruction of events, the magnetic field used to determine the momen-

Source of systematic uncertainty	Uncertainty in sample total event rate (%)		
	CC-0π	CC-1π	CC-Other
Magnetic field distortions	0.0254	0.0621	0.0812
Momentum resolution	0.0597	0.0951	0.2135
Momentum scale	0.0603	0.0784	0.2269
TPC PID	0.3083	0.7606	0.7478
FGD PID	0.0117	0.0350	0.0163
Charge misidentification	0.1719	0.2397	0.2017
Michel electron eff. and pur.	0.0613	0.2398	0.0076
TPC clustering eff.	0.0004	0.0004	0.0016
TPC tracking eff.	0.2796	0.2505	0.7180
FGD tracking eff.	0.1574	0.0748	0.9789
Sand Muons	0.0615	0.0795	0.0296
TPC-FGD matching eff.	0.0001	0.0001	0.0001
Pile-up	0.0727	0.0726	0.0726
FGD mass	0.5859	0.5741	0.5880
Out-Of-Fiducial-Volume	0.4674	0.7838	0.5165
Pion reinteractions	1.6658	2.7925	5.0173
Total	**1.9144**	**2.9813**	**6.0416**

Table 5.1: Contribution of each individual source of systematic uncertainty (in the order described in Section 5.4) to the total event rate in each of the ND280 neutrino beam mode ν_μ samples. Table data from [32].

tum of the track is one that was obtained by closing the magnet around an empty ND280 detector basket, and measuring the magnetic field at multiple points, to produce a full magnetic field map. TPC Laser (Section 4.4.2) calibration data has been used to provide an empirically corrected field map, which is also used to provide an alternate reconstruction of the track's momentum.

The magnetic field distortion systematic uncertainty is modelled with one uniform random variable between 0 and 1, used to vary the momentum of each track between the default field map and the empirical field map. The momentum having changed, the selection is rerun to take into account the new observable value.

5.4.2 Momentum resolution

The momenta of charged particles are key observables for ND280, especially for the muon candidate. The momentum of the muon candidate is directly used in the selection, and the distribution of muon momenta is used in the analysis of the sample, as described in Chapter 6.

Source of systematic uncertainty	Uncertainty in sample total event rate (%)	
	$\bar{\nu}_\mu$ CC-1-Track	$\bar{\nu}_\mu$ CC-N-Tracks
Magnetic field distortions	0.0064	0.0476
Momentum resolution	0.0616	0.1747
Momentum scale	0.0395	0.1220
TPC PID	0.2703	0.5400
FGD PID	NA	NA
Charge misidentification	0.0921	0.0709
Michel electron eff. and pur.	NA	NA
TPC clustering eff.	0.0002	0.0017
TPC tracking eff.	0.4987	0.1365
FGD tracking eff.	NA	NA
Sand Muons	0.1522	0.2179
TPC-FGD matching eff.	0.0002	0.0001
Pile-up	0.1466	0.1466
FGD mass	0.5872	0.5732
Out-Of-Fiducial-Volume	0.4784	0.8063
Pion reinteractions	5.3537	7.8775
Total	**5.7227**	**8.4491**

Table 5.2: Contribution of each individual source of systematic uncertainty (in the order described in Section 5.4) to the total event rate in each of the ND280 antineutrino beam mode $\bar{\nu}_\mu$ samples. Sources of systematic uncertainty marked "NA" were not applicable due to being specific to FGD information that is not used in the selection of these samples. Table data from [35].

The momentum resolution is determined by considering a sample of tracks that cross through multiple TPCs, and taking the measurement of momentum transverse to the magnetic field in each TPC. After correcting for energy loss in the FGDs between the TPCs, the differences between the independent momentum estimates is a Gaussian centred at zero, whose standard deviation is primarily due to the momentum resolution. This is done over multiple momentum, angle, and position ranges. The momentum resolution systematic is treated by 10 Gaussian random variables to modify the momentum of tracks independently in these different ranges. Since observables are modified, the selection is redone after the variation is applied.

5.4.3 Momentum scale

The measurement of a particle's momentum comes from measuring the curvature of the track in the TPC caused by the magnetic field. For a constant and uniform

Source of systematic uncertainty	Uncertainty in sample total event rate (%)	
	ν_μ CC-1-Track	ν_μ CC-N-Tracks
Magnetic field distortions	0.0397	0.0794
Momentum resolution	0.0958	0.1867
Momentum scale	0.0939	0.1527
TPC PID	0.4333	0.4417
FGD PID	NA	NA
Charge misidentification	0.0337	0.0489
Michel electron eff. and pur.	NA	NA
TPC clustering eff.	0.00001	0.0020
TPC tracking eff.	0.4043	0.0587
FGD tracking eff.	NA	NA
Sand Muons	0.4663	0.1571
TPC-FGD matching eff.	0.00001	0.00005
Pile-up	0.1331	0.1331
FGD mass	0.5286	0.5693
Out-Of-Fiducial-Volume	1.5356	0.6698
Pion reinteractions	1.5543	3.1820
Total	**2.4562**	**3.3573**

Table 5.3: Contribution of each individual source of systematic uncertainty (in the order described in Section 5.4) to the total event rate in each of the ND280 antineutrino beam mode ν_μ samples. Sources of systematic uncertainty marked "NA" were not applicable due to being specific to FGD information that is not used in the selection of these samples. Table data from [36].

magnetic field, this would be a straightforward application of the Lorentz Force Law, but magnetic field distortions can result in a bias in the measured momentum. This is referred to as the *momentum scale*, and understanding it is important to making accurate momentum measurements.

The momentum scale systematic uncertainty is derived from the uncertainty in the x component of the magnetic field in the default field map. It has also been checked by using the range of cosmic ray muons that stop in FGD1. It is treated by a Gaussian random variable used to adjust the measured track momenta, followed by redoing the selection.

5.4.4 TPC PID

As is evident from the selection steps in Sections 5.2 and 5.3, particle identification (abbreviated *PID*) is one of the important functions that the TPCs perform in the

event selection. It is therefore important to take into account how accurate the TPC PID is, as well as any differences between the data and the simulated event sample.

The TPC PID systematic is determined by considering *control samples* of muons, electrons, and protons passing through the TPC, in data and simulated event samples. These control samples are obtained through their own specialized selections, in order to achieve high purity of the desired particle. The pull distributions are calculated. The difference in the pull mean values between the data and the simulated event sample is used to estimate the bias between data and the model, and the ratio of the pull sigma values (data/model) is used to estimate the smearing to be applied.

The TPC PID systematic is treated by 88 Gaussian random variables, independently varying the mean difference and sigma ratio according to their respective errors for muons, electrons, and protons, over different momentum regions. The calculated dE/dx is changed according to these values, and the selection rerun with the new values. Since the dE/dx for pions is very similar to for muons (due to their similar mass), the treatment for pions is the same as for the muons.

5.4.5 FGD PID

In addition to the TPC PID, the FGD also provides particle identification, which is used in the neutrino mode selection to identify pions that stop in the FGD. As with the TPC PID, it is important to take into account how accurate the FGD PID is, as well as any differences between the data and the simulated event sample.

Similarly to the TPC PID systematic, control samples of protons and muons were selected to evaluate the size of the FGD PID systematic uncertainty, and pions were assumed to behave similarly to muons. As the FGD PID is only used on particles that have no TPC segment (i.e. start and stop in the FGD), this systematic is not broken down by momentum range, and therefore is modelled with only 4 Gaussian random variables, in a similar way to the TPC PID.

5.4.6 Charge misidentification

The selections described in Sections 5.2 and 5.3 use the reconstructed charges of the tracks in the event. The charge of the particle producing a track in the detector is determined by the direction that track curves in the magnetic field, and the direction the particle is travelling in (in accordance with the Lorentz force law). The probability that the charge is misidentified (for example, due to the wrong direction being

reconstructed, or the particle being high momentum and therefore low curvature) is adjusted in the simulated event samples to account for this systematic uncertainty. The charge confusion systematic uncertainty is treated by 7 Gaussian random variables, which are used to weight simulated events accounting for each track in the event.

5.4.7 Michel Electron efficiency and purity

The neutrino mode selection uses tagging of Michel Electrons as part of its algorithm to count π^+ produced in neutrino interactions that stopped in FGD1. It is therefore important to understand how often a Michel Electron produced in FGD1 is properly tagged, that is, the Michel Electron efficiency. Also included here is the Michel Electron purity, which considers how often backgrounds are mistakenly tagged as Michel Electrons.

The Michel Electron efficiency is determined by considering a control sample of cosmic ray muons that stop in the FGD1 fiducial volume. These cosmic ray muon tracks are plentiful and easy to identify, and each one should produce a Michel Electron when the stopped muon decays. Measuring the portion of these muons for which a Michel Electron is tagged therefore gives the efficiency of tagging them. The Michel Electron purity is assessed by considering data and simulated beam spills containing no activity in the FGDs during the time of the beam bunches in the spill. Since the amount of background is dependent on the neutrino beam power, the purity measurement is broken down by run period. The efficiency and purities are calculated both in data and simulated event samples.

The uncertainties in the Michel Electron efficiency and purity in FGD1 is treated by a total of 8 Gaussian random variables, one to vary the efficiency, and 3 to vary the purity independently in different run periods, separately for data and simulated samples. These values are then used to calculate a weight for the simulated event depending on the number of true Michel Electrons in the event, and the number of measured Michel Electrons in the event.

5.4.8 TPC clustering efficiency

The first step of the TPC reconstruction is to connect individual Micromegas pad signals above threshold in the same row or column that are close in space and time into *clusters*. The clusters are used by the pattern recognition algorithms and the

track parameters are estimated by a maximum likelihood approach. The clustering efficiency is the probability that a cluster is found along a particle's trajectory through the TPC. Differences in the clustering efficiency between data and the simulated event sample would manifest as different fractions of data and simulated events passing the "Track Quality Cut" described in Section 5.2.

The TPC clustering efficiency is determined by examining the distribution of the number of clusters per track in data and the simulated event sample. Gaussian random variables are then used to vary the data and detector model efficiency, and compute an event weight according to the number of tracks and clusters to take into account the data-model difference in efficiency.

5.4.9 TPC tracking efficiency

The TPC tracking efficiency is the probability that when a charged particle travels through the TPC, that a track is reconstructed for it. Any difference in this quantity between the detector and the detector model must be accounted for, as reconstructing tracks in the TPC is at the heart of the event selection.

The TPC tracking efficiency is determined by considering control samples of beam and cosmic ray muons, in data and simulated event samples. Its uncertainty is treated with 6 Gaussian random variables to vary the detector model efficiencies in different momentum regions and compute an event weight.

5.4.10 FGD tracking efficiency

Like the TPC tracking efficiency, the FGD tracking efficiency is the probability that a charged particle travelling through the FGD will result in a reconstructed track. Any possible difference in this quantity between the detector and the detector model must be accounted for, as reconstructing tracks in the FGD plays a role in the outgoing pion counting that is needed by the neutrino mode event selection.

The use case of the FGD-only reconstruction (only on tracks that do not exit the FGD) makes selecting a good control sample difficult, since an independent ND280 subdetector cannot be used. The FGD tracking efficiency is determined by selecting events in the FGD containing CCQE-like vertices, where there is a muon candidate track in the TPC, but no tracks contained in the FGD. This is done for data and the simulated event sample. Simulated proton and pion tracks were then inserted into these samples, which allows the tracking efficiency to be evaluated in data and

simulated samples, as well as examining the effect of the momentum and angle of the particle. The FGD tracking efficiency uncertainty is treated by 24 Gaussian random variables, which vary efficiencies for the detector model, for protons and pions, over different angular regions and are used to calculate an event weight.

5.4.11 Sand Muons

The ND280 detector pit, being below the surface, is surrounded by the material making up the "ground" of the J-PARC facility, which is sand. In addition to interacting inside the detector, neutrinos from the beam can also interact in the sand surrounding the ND280 pit, and possibly enter the detector, where they would contribute to the Out-Of-Fiducial-Volume background (discussed in Section 5.4.15) and if coincident with an FGD1 event, contribute to pile-up as well (discussed in Section 5.4.13). This systematic uncertainty concerns the sand muon events that pass the event selection. Since the simulated samples only include interactions in the ND280 detector plus the surrounding magnet, the systematic uncertainty due to sand muons being mis-selected into the event sample is handled separately.

A dedicated sample of simulated sand muon events is included in the analysis, and an event weight is applied to these events to account for the uncertainty on the number of sand muons entering ND280. This uncertainty is determined by comparing the data and simulated rates of tracks entering ND280 through the upstream end of the P0D. This is dependent on the beam mode and the version of the neutrino interaction model, therefore 3 Gaussian random variables are used to treat this systematic uncertainty in each configuration independently.

5.4.12 TPC-FGD matching efficiency

As discussed earlier in this chapter, the event selections are heavily dependent on the reconstruction matching tracks in the TPC with tracks in FGD1. To reiterate, if an FGD track and a TPC track from a muon produced in a CCQE interaction were not successfully matched, the event would not even be selected into the CC-Inclusive sample. It is therefore important to understand how often TPC-FGD matching is done properly, and this is quantified in the TPC-FGD matching efficiency.

The TPC-FGD matching efficiency is measured using control samples of cosmic ray muons and sand muons (which would produce tracks across multiple subdetectors which should be matched properly), in data and simulated event samples. Its sys-

tematic uncertainty is modelled with two Gaussian random variables, which adjust the detector model according to their uncertainties, and produce a weight for each simulated event.

5.4.13 Pile-up

Pile-up occurs when there are multiple neutrino interactions in the same time interval, producing tracks in the detector that can be mistaken as originating from the same neutrino interaction. Since the assumption in the analysis is that each event contains only one interaction, the pile-up rate is important to consider.

The ND280 event selections, through their various restrictions on track origins, and through dividing up the beam spill into its constituent bunches, manage to limit pile-up as a concern. The pile-up related issue that needs to be accounted for concerns sand muons. In the data, events containing sand muons would be excluded from the event selection. In the simulated event sample, the lack of sand muons creates a need to reduce the simulated event rate to compensate for events that would have been excluded due to a sand muon also being present, while taking into account the uncertainty on the sand muon event rate. The pile-up systematic uncertainty is modelled by 9 Gaussian random variables, which provide an event weight according to the pile-up uncertainty separately for each run period (since the sand muon production rate depends on the beam conditions of the run period.)

5.4.14 FGD mass

The number of events occurring inside FGD1 is dependent on the number of nuclei inside FGD1 with which neutrinos can interact, which is proportional to the mass of FGD1. Understanding both how the mass differs between the simulation and reality, as well as the uncertainty on the known mass, is therefore important in order to model neutrino interaction rates properly.

The FGD mass systematic is determined by a careful measurement and accounting of the materials making up the FGD, allowing a correction to be computed between data and the simulated event sample, and an uncertainty to be applied based on the uncertainty in the measured mass. The FGD mass systematic is calculated by applying the correction and modelling the uncertainty with a Gaussian random variable, and using this new mass value relative to the detector model mass to weight the event proportionally.

5.4.15 Out-Of-Fiducial-Volume

The event selections described in Sections 5.2 and 5.3 are meant to only consider neutrino or antineutrino interactions in the FGD1 fiducial volume, and the event rate is an important part of the information used to tune the neutrino interaction models. However, the ND280 detector contains other subdetectors as well as dead material that neutrinos can interact in, producing tracks in the detector. It is therefore important to quantify how often such "Out-Of-Fiducial-Volume" events are misidentified as originating in the FGD1 fiducial volume.

The Out-Of-Fiducial-Volume systematic uncertainty is determined by an examination of the simulated event sample and data for the specific reconstruction failures that can result in Out-Of-Fiducial-Volume events mistakenly passing the event selection. The Out-Of-Fiducial-Volume systematic is modelled by 18 Gaussian random variables, which apply weights to Out-Of-Fiducial-Volume simulated events according to the reason it passed selection and the uncertainty the examination of data and simulated events determined for that specific process.

5.4.16 Pion reinteractions

The neutrino mode selections depend on counting pions produced in the neutrino interactions, and the antineutrino mode selections depend on counting tracks that leave FGD1 and make it to the TPC. Unlike the muons produced in neutrino interactions, pions can undergo interactions via the strong force, which gives them a much higher interaction cross section. As discussed in Section 2.2, such interactions occur inside the nucleus the neutrino is produced in, which are denoted *Final State Interactions*, or FSI. However, the event selections discussed in Sections 5.2 and 5.3 are defined relative to the particles that escape the nucleus. Such pions ultimately can interact with other nuclei in the detector volume, and it is this phenomenon that is referred to as *pion reinteractions*.

At the pion momenta typical at ND280, for an FGD and TPC based analysis, three pion reinteraction channels are of main concern:

- Absorption: The pion interacts with a nucleus and the final state of the interaction contains no pions. If a pion were to disappear via this process before it could be measured by the detector, it may be selected into the wrong sample.

- Charge Exchange: A pion interacts with the nucleus and there is only one pion

in the final state of the interaction, differing in charge by 1 from the incoming pion. This would cause a π^+ or π^- to disappear and be replaced by a π^0. Once again, such a substitution could cause the event to be selected into the wrong sample.

- Quasi-Elastic Scattering: A pion interacts with the nucleus and the final state of the interaction contains a pion of the same charge. Also, the kinetic energy of the particle in the center of mass frame is not conserved (i.e. it is an inelastic collision.) Although in this case the outgoing pion is the same as the incoming pion, the possibly large changes of direction could affect the reconstruction of the particle. For example, a pion initially travelling towards a TPC could be scattered towards the ECal instead, and not be detected.

Therefore, pion reinteractions are of great concern to the event selection. Unfortunately, at the momenta of pions at ND280, and on the materials making up the detector, the uncertainty on the cross sections of these processes is large. In addition, it was found that Geant4 model (in this case the Bertini Cascade [63]) for these processes equates to cross sections that are significantly different from the world data. An example is given in Figure 5.8.

In order to evaluate this systematic uncertainty, the collection of external data on these processes used to tune the NEUT FSI model (tuning described in [51]) was used. The Geant4 model's cross section for the processes was computed on relevant detector materials over the relevant momentum range. In between data points the external data was interpolated linearly (with errors inflated as a function of the distance from the closest data point). Outside the momentum region for which there was external data, the shape of the Geant4 model was used, but scaled so as to be continuous at the boundary between the external data and the extrapolation. The uncertainties on the extrapolated data increase with distance from the last data point. For both interpolations and extrapolations of the external data, the uncertainty could only increase up to a maximum. This maximum was chosen by applying the corrections used at the end points of the data momentum region to the Geant4 value throughout the data momentum region, then taking the largest data $\pm 1\sigma$ to Geant4 difference. This procedure was chosen to conservatively assign the uncertainties to cover possible shape differences in the extrapolated region (with the conservative nature of the extrapolated uncertainties demonstrated in Figure 5.8). As this maximum tends to be quite large, it was also deemed a sufficient maximum uncertainty when performing

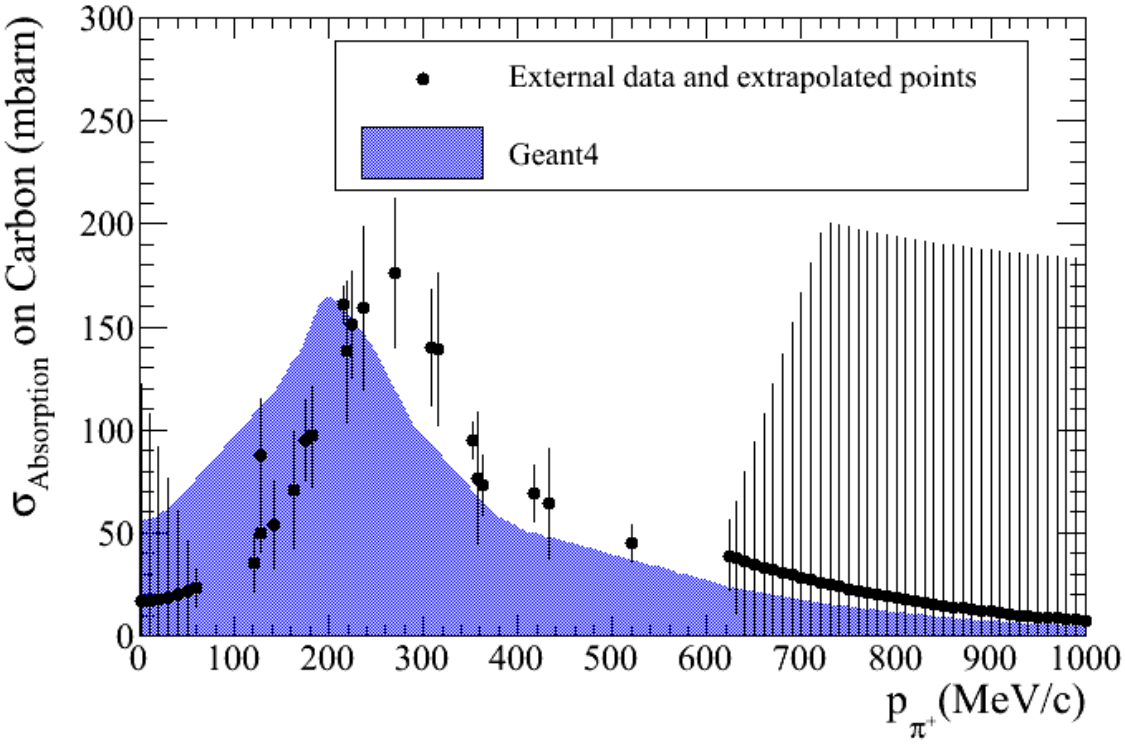

Figure 5.8: Comparison of the cross section for absorption of π^+ on carbon nuclei in Geant4 and from external data (with extrapolations outside the momentum region covered by the data). The external data spans the momentum region of 58.99 MeV/c to 623.7 MeV/c, and comes from multiple experiments [25, 68, 59, 84, 87, 78]. The extrapolated points and their uncertainty are determined using the procedure described in this section (Section 5.4.16).

interpolations. Although Figure 5.8 would appear to suggest that linear interpolation of the error bars would be reasonable, other processes and materials had large momentum regions between data points, therefore necessitating larger uncertainties in these gaps (up to the maximum) as the distance from the nearest data point increases.

In order to account for the difference between the pion reinteraction model and the external data cross sections for Absorption, Charge Exchange, and Quasi-Elastic Scattering, an event weight is calculated to correct each simulated event to the external data cross section (or an extrapolated or interpolated value). Then, to model this systematic uncertainty, 3 Gaussian random variables are used, one to vary each of the Absorption, Charge Exchange, and Quasi-Elastic Scattering cross sections, according to their uncertainty in the external data and its interpolations and extrapolations. A weight is then calculated to use these varied cross sections.

In computing the weight for an event, all pions relevant to the event (i.e. in FGD1 and out to the inner volume of TPC2) are considered. All of the particles produced in the interaction at the end of the simulated pion's trajectory are examined using true information from the simulation, in order to identify the type of interaction that the pion underwent. Since the cross sections of the relevant process also affect the probability of the particle not interacting, this also needs to be taken into account. The event weight applied to the simulated event is therefore calculated via the following procedure:

1. Take a step along a relevant pion trajectory through the detector volume. Small steps are used where the pion's momentum is approximately constant in order to effectively numerically integrate along the pion's trajectory.

2. Use the pion's momentum and the detector composition of the step to calculate the non-interaction probability during the step from the cross sections for Absorption, Charge Exchange, and Quasi-Elastic Scattering.

3. Use the Bethe formula and Lorentz force law to determine the pion's momentum for the next step.

4. Continue stepping until the pion either:

   - Stops.
   - Escapes FGD1 + dead material up to TPC2 active volume.
   - Interacts. In this case, determine the cross section for this interaction from the pion's final momentum and the material it interacted in.

5. Given two different sets of cross section values, the event weight for this pion is ratio of survival probabilities multiplied by the ratio of the cross sections for the pion's interaction (if it interacted at the end of its trajectory).

6. Repeat for the remaining relevant pions. The total event weight is the product of the weight for each pion.

Chapter 6

Measuring model parameters with ND280 data

As described in Chapter 5, ND280 selects a large number of events into different samples. This chapter describes how this data is used to measure parameters that are relevant to the neutrino oscillation analysis.

6.1 Motivation

In Section 2.3, neutrino oscillation parameters were shown to affect the probability of a neutrino produced as one flavour being observed as a neutrino of another flavour. However, detectors do not directly measure oscillation probabilities; they measure event rates. The number of neutrinos and their energy spectrum observed at Super-Kamiokande depend on:

1. Unoscillated neutrino beam flux: The number of neutrinos of each flavour passing through the fiducial volume of the detector, and their energy spectrum in the absence of neutrino oscillation.

2. Neutrino interaction cross sections: The probability that a given neutrino will interact with the detector, and whether it will be an interaction process defined as "signal" or "background."

3. Detector performance: How well the detector can measure and reconstruct events.

4. Neutrino oscillation probability: The probability that a neutrino produced by the beam appears as the same flavour or a different flavour. This is usually a function of several oscillation parameters.

So, in addition to the oscillation parameters, which we shall denote $\vec{o}$, one can also define a set of parameters that describe the beam flux, denoted $\vec{b}$, a set of parameters in a neutrino cross section model, denoted $\vec{x}$, and a set or parameters describing the detector systematic uncertainties, $\vec{d}$. Therefore, amongst the oscillation parameters we wish to measure, there are also so called *nuisance parameters* (also referred to as *systematic parameters*, as they parameterize the systematic uncertainties of the analysis) that must be accounted for, and would increase the uncertainty on any measurement of the oscillation parameters. Thankfully, measurements by other experiments ("external data") or specific internal measurements to constrain detector systematics (as discussed in Sections 5.4 and 7.3) can be used to constrain all nuisance parameters. In addition, ND280 measurements can also constrain flux and cross section parameters.

Given the external data ($\vec{M}^{Ext}$), ND280 data ($\vec{M}^{ND280}$) and SK data ($\vec{M}^{SK}$), and the beam, cross section, oscillation, and detector systematic parameters that describe this data ($\vec{b}$, $\vec{x}$, $\vec{o}$, and $\vec{d}$, respectively) one can define a global *likelihood function*, $\mathcal{L}(\vec{b},\vec{x},\vec{o},\vec{d}) = p(\vec{M}^{Ext},\vec{M}^{ND280},\vec{M}^{SK}|\vec{b},\vec{x},\vec{o},\vec{d})$, the probability density of the observed data given the parameter values. In practice, maximizing this global likelihood function can prove difficult, as this involves simultaneous consideration of multiple datasets from different experiments, and a large number of parameters, making for a complicated and computationally demanding analysis. Instead, a piecewise approach is taken:

1. Analysis of the external data $\vec{M}^{Ext}$ (including ND280 control samples) provides the information needed to model flux (Section 6.2.2), cross section (Section 6.2.3), and detector (Section 6.2.4) systematic parameters with multivariate Gaussian likelihood functions.

2. Determine the parameter values that maximize the likelihood $\mathcal{L}_{ND280}(\vec{b},\vec{x},\vec{d})$, which is the product of a Poisson term to consider the ND280 data, and the Gaussian constraint terms determined in Step 1. This is the topic of this chapter.

3. Determine the parameter values that maximize the likelihood $\mathcal{L}(\vec{b},\vec{x},\vec{o},\vec{d})$, which

is the product of a Poisson term to consider the Super-Kamiokande data, and a constraint term that models the results of the ND280 analysis in Step 2 and the Super-Kamiokande detector systematic uncertainties as a multivariate Gaussian likelihood function. This is discussed in Chapter 7.

6.2 Analysis method

This analysis uses the Maximum Likelihood method to estimate the beam flux, cross section, and detector systematic parameters in the beamline, neutrino interaction, and ND280 models. The analysis relies on the algorithms of Minuit [66], in this case, the C++ implementation (Minuit2) included as part of the ROOT data analysis framework [41]. The MIGRAD algorithm (a gradient descent method) is used to minimize $-2\ln\mathcal{L}$. Then, the HESSE algorithm computes the full matrix of second derivatives (the Hessian matrix) of $-2\ln\mathcal{L}$ around the optimal parameter values found by MIGRAD. It then determines the covariance matrix (and therefore the uncertainty on the parameter estimations) by using that the inverse of the Hessian of $-\ln\mathcal{L}$ is an estimator for the covariance matrix (see, for example, Section 6.6 on p.76-78 of [47]). Parameters relevant to Super-Kamiokande are then used in the oscillation analysis, described in Chapter 7. Since the result of this analysis is a multivariate Gaussian distribution with mean vector given by the optimal parameter values, and the covariance matrix of the parameters has been calculated, the parameters not relevant to the analysis of the Super-Kamiokande data can just be ignored. This section describes the key components of this analysis in more detail.

6.2.1 The ND280 binned likelihood

In order to analyze the events selected into the samples described in Chapter 5, it is useful to subdivide the samples into bins of kinematic variables. This allows the analysis to constrain the neutrino energy distribution at Super-Kamiokande, in addition to the overall event rate. For the signal process (CCQE), the energy is reconstructed from the muon momentum (p_μ) and cosine of the muon angle with the neutrino beam direction ($\cos\theta_\mu$), as shown in Equation 2.13. A two dimensional binning in p_μ and $\cos\theta_\mu$ is therefore a natural choice, though for this analysis θ_μ is defined relative to the central axis of ND280 instead of the beam direction. This simplifies calculation of $\cos\theta_\mu$ while retaining the shape information useful to this analysis. This choice

of kinematic variables and binning also provides shape information that is helpful to constrain cross section model parameters (that would be lost with a one dimensional reconstructed neutrino energy binning, for example). This binning is described further in Section 6.2.4.

A useful consequence of binning the data and the simulated events is that the content of each bin is Poisson distributed. Therefore, given that the model prediction for bin i, $N_i^p(\vec{b},\vec{x},\vec{d})$, is the expected number of events in the bin, and the data observation, N_i^d, is the observed number of events, the probability of making that observation is the Poisson probability given by Equation 6.1:

$$P(N_i^d|N_i^p(\vec{b},\vec{x},\vec{d})) = \frac{(N_i^p(\vec{b},\vec{x},\vec{d}))^{N_i^d} e^{-N_i^p(\vec{b},\vec{x},\vec{d})}}{N_i^d!} \tag{6.1}$$

Therefore, the Poisson term of the likelihood function is simply the product of Equation 6.1 evaluated for each bin.

This approach relies on the model providing a prediction for each bin that is a function of the flux, cross section, and detector systematic parameters ($N_i^p(\vec{b},\vec{x},\vec{d})$). The analysis uses Monte Carlo integration, where tuning weights based on these parameters are applied to each simulated event individually, and the bin contents recalculated for each variation of the systematic parameters during the minimization. The relationships between the parameters and the tuning weights are described in Sections 6.2.2 (flux), 6.2.3 (cross section), and 6.2.4 (detector).

In addition to the tuning weights are two sets of weights concerning the beam flux. In order to ensure that the cross section model is well-represented by the simulated event sample, ~ 10 times the data POT is used in the analysis for each run period. Each simulated event is therefore weighted down to the data POT for that run period.

The second set of weights concerns the beam model. The default simulated event sample is produced with the default beam model. External data and measurements from beamline monitors and INGRID are used to further tune the flux prediction, producing a weight for each simulated event, which depends on its true neutrino energy and flavour.

The remaining terms in the likelihood are the constraint terms for the beam (Section 6.2.2), cross section (Section 6.2.3), and ND280 detector (Section 6.2.4) parameters. Since these constraint terms are all arrived at independently, they are modelled by three separate multivariate Gaussian terms, $\pi(\vec{b})$ (beam flux), $\pi(\vec{x})$ (cross section), and $\pi(\vec{d})$ (detector). Each of the $\pi(\vec{\phi})$ (for $\vec{\phi}$ in $\{\vec{b},\vec{x},\vec{d}\}$) is given by Equation 6.2,

where V_ϕ is the covariance matrix that describes the covariance between the $\vec{\phi}$ parameters, $\Delta\vec{\phi} = \vec{\phi}_{curr} - \vec{\phi}_{nom}$ is the difference between the current and nominal value of the parameters, and k is the number of parameters (i.e. the dimension of $\vec{\phi}$).

$$\pi(\vec{\phi}) = (2\pi)^{-\frac{k}{2}} |V_\phi|^{-\frac{1}{2}} e^{-\frac{1}{2}\Delta\vec{\phi}(V_\phi^{-1})\Delta\vec{\phi}^T} \tag{6.2}$$

Having defined all the components of our likelihood function, we make a number of utilitarian choices to arrive at the quantity manipulated in this analysis.

To start, we use the likelihood function to define a likelihood ratio, given in Equation 6.3. It has the likelihood function we defined in the numerator, and in the denominator (which is a constant) the likelihood function we defined evaluated at $N_i^p = N_i^d$, with the constraint terms evaluated at the nominal parameter values.

$$\lambda_{ND280} = \frac{\pi(\vec{b})\pi(\vec{x})\pi(\vec{d}) \prod_i (N_i^p(\vec{b},\vec{x},\vec{d}))^{N_i^d} e^{-N_i^p(\vec{b},\vec{x},\vec{d})}}{\pi(\vec{b}_{nom})\pi(\vec{x}_{nom})\pi(\vec{d}_{nom}) \prod_i (N_i^d)^{N_i^d} e^{-N_i^d}} \tag{6.3}$$

This is done in order to take advantage of the fact that $-2\ln(\lambda_{ND280})$ is χ^2 distributed (see Section 38.2.2.1 of [79]), providing a natural goodness of fit test. Due to this property, it is conventional to adopt the notation $\Delta\chi^2_{ND280} \equiv -2\ln(\lambda_{ND280})$.

As mentioned in the beginning of Section 6.2, estimating the covariance of the parameters requires the computation of the Hessian of $-\ln\mathcal{L}_{ND280}$. Since λ_{ND280} differs only by a constant factor from $\mathcal{L}_{ND280}$, the Hessian of $-\ln(\lambda_{ND280})$ is equal to that of $-\ln\mathcal{L}_{ND280}$. Therefore, minimizing $\Delta\chi^2_{ND280}$ does not complicate the estimation of the covariance of the parameters.

Therefore, this analysis minimizes the quantity $\Delta\chi^2_{ND280}$, which is given in Equation 6.4.

$$\begin{aligned}\Delta\chi^2_{ND280} =& 2\sum_i^{Nbins}\left[N_i^p(\vec{b},\vec{x},\vec{d}) - N_i^d + N_i^d\ln(N_i^d/N_i^p(\vec{b},\vec{x},\vec{d}))\right] \\ &+ \sum_i^{E_\nu\ bins}\sum_j^{E_\nu\ bins}\Delta b_i(V_b^{-1})_{i,j}\Delta b_j + \sum_i^{xsec\ pars}\sum_j^{xsec\ pars}\Delta x_i(V_x^{-1})_{i,j}\Delta x_j \\ &+ \sum_i^{det\ bins}\sum_j^{det\ bins}\Delta d_i(V_d^{-1})_{i,j}\Delta d_j\end{aligned} \tag{6.4}$$

Now that the likelihood has been defined along with how it is maximized, the

following sections will discuss in more detal how the beam flux model (Section 6.2.2), cross section model (Section 6.2.3), and the ND280 data, model prediction, and detector systematic uncertainties (Section 6.2.4) are considered in the analysis.

6.2.2 Neutrino beam flux parameterization

The number of neutrinos expected at the detector, their flavour, and their energy spectrum are important to model correctly in order to do a neutrino oscillation experiment. The uncertainties on this model ultimately translate into uncertainties on the neutrino oscillation measurement. There are many elements of the neutrino beam production that ultimately have an effect on the neutrino flux, such as the properties of the proton beam (e.g. energy, intensity, bunch shape, direction), and the cross sections for both proton interaction processes in the target, as well as interactions of the secondary particles (i.e. the pions that later decay into neutrinos.) Therefore, T2K has a complex flux model (described in [6]), using technical design specifications and standard particle physics simulation packages, further tuned with data from beam monitors and with the results of external experiments.

From this model, a flux prediction is produced which is binned in neutrino energy, for each of ν_μ, ν_e, $\bar{\nu}_\mu$ and $\bar{\nu}_e$, for both ND280 and Super-Kamiokande. It is done separately for each run period, in order to correct for different beam conditions as measured by the beam monitors in each run, as was discussed in Section 6.2.1. This flux prediction is used as input to produce the default simulated event sample. The beam flux is tuned by minimizing $\Delta\chi^2_{ND280}$, using the $\vec{b}$ parameters. We define 100 $\vec{b}$ parameters, corresponding to 100 different bins of beam mode, neutrino flavour, detector, and neutrino energy. All sources of systematic uncertainty in the flux model are considered through simulation studies to produce a covariance matrix for the $\vec{b}$ parameters. The bins are divided into energy bins (GeV) by flavour and by beam mode as follows:

- ν_μ (ν-mode), $\bar{\nu}_\mu$ ($\bar{\nu}$-mode): 0.0, 0.4, 0.5, 0.6, 0.7, 1.0, 1.5, 2.5, 3.5, 5.0, 7.0, 30.0
- $\bar{\nu}_\mu$ (ν-mode), ν_μ ($\bar{\nu}$-mode): 0.0, 0.7, 1.0, 1.5, 2.5, 30.0
- ν_e (ν-mode), $\bar{\nu}_e$ ($\bar{\nu}$-mode): 0.0, 0.5, 0.6, 0.8, 1.5, 2.5, 4.0, 30.0
- $\bar{\nu}_e$ (ν-mode), ν_e ($\bar{\nu}$-mode): 0.0, 2.5, 30.0

This binning parametrizes with 50 parameters the flux of ν_μ, ν_e, $\bar{\nu}_\mu$ and $\bar{\nu}_e$ from 0-30 GeV in both beam modes. This results in a total of 100 parameters to include in the analysis (50 for ND280, and 50 for Super-Kamiokande.) Since these parameters are defined relative to the tuned flux prediction, they all have a nominal value of 1. Their correlation matrix is shown in Figure 6.1a. These flux parameters are

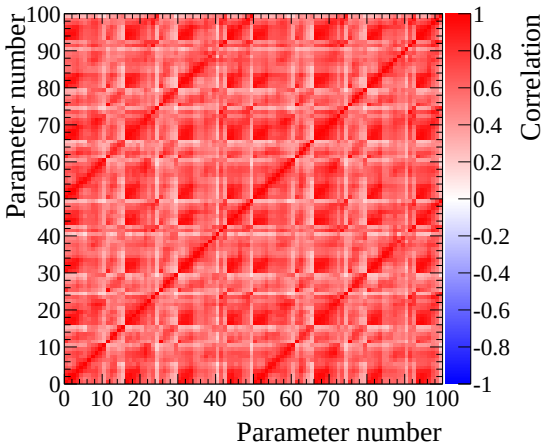

(a) The correlation matrix for the 100 flux parameters prior to the analysis.

Parameters	Parameter number(s)
ND280, ν mode, ν_μ	0 – 10
ND280, ν mode, $\bar{\nu}_\mu$	11 – 15
ND280, ν mode, ν_e	16 – 22
ND280, ν mode, $\bar{\nu}_e$	23 – 24
ND280, $\bar{\nu}$ mode, ν_μ	25 – 29
ND280, $\bar{\nu}$ mode, $\bar{\nu}_\mu$	30 – 40
ND280, $\bar{\nu}$ mode, ν_e	41 – 42
ND280, $\bar{\nu}$ mode, $\bar{\nu}_e$	43 – 49
SK, ν mode, ν_μ	50 – 60
SK, ν mode, $\bar{\nu}_\mu$	61 – 65
SK, ν mode, ν_e	66 – 72
SK, ν mode, $\bar{\nu}_e$	73 – 74
SK, $\bar{\nu}$ mode, ν_μ	75 – 79
SK, $\bar{\nu}$ mode, $\bar{\nu}_\mu$	80 – 90
SK, $\bar{\nu}$ mode, ν_e	91 – 92
SK, $\bar{\nu}$ mode, $\bar{\nu}_e$	93 – 99

(b) The correspondance between the flux parameters and their parameter number.

Figure 6.1: Flux parameters and their correlations prior to the analysis.

very highly correlated, between the different energy bins, flavours, beam modes, and detectors. As a result, the analysis of the ND280 data reduces the uncertainty due to the flux model in the Super-Kamiokande model predictions due to uncertainties in the beam flux.

6.2.3 Neutrino cross section parameterization

As discussed in Section 2.2, there are multiple interaction channels for neutrinos on nuclei. Furthermore, the products of these interactions can be further modified by interactions that occur inside the nucleus, Final State Interactions (FSI). These processes are all modelled in the neutrino interaction generator, which in the case of this analysis is NEUT [62]). Given the flux prediction, NEUT simulates the corresponding neutrino interactions in the detector according to its model. It simulates both the neutrino interaction itself, as well as any interactions the resulting particles have

inside the nucleus (FSI). NEUT then passes the list of particles that leave the nucleus and their kinematic information on to the next stage in the detector simulation, where Geant4 [12] is used to simulate the particles as they travel through the detector volume.

There are a number of ways that the NEUT model prediction can be tuned. One simple way is to apply a multiplicative factor to the events in a given interaction channel. This simply increases or decreases the rate at which a given interaction channel occurs, in a uniform manner across all neutrino energies, and all interaction product observables. This multiplicative factor is referred to as a *normalization parameter*. Such parameters are labelled "Norm" in Table 6.3.

Alternatively, the model for a given process may have model parameters that enter into the theoretical calculation of the cross section, and the determination of which particles are produced in the interaction, and their momentum and angle with the path of the incoming neutrino. Tuning these parameters can significantly change the composition of the simulated event sample, and alter the p_μ and $\cos\theta_\mu$ distributions. This potentially complicated response earns these parameters the classification of *response parameters*. The CCQE model and the CCRES model are both parameterized this way, as is the model for FSI.

Alas, with the potentially complicated response caused by the tuning of a response parameter comes a computational concern. Nominally, one would have to rerun NEUT with the tuned parameter value, then run the full chain of ND280 simulation, calibration, reconstruction, and analysis software packages in order to produce a simulated event sample reflecting the new parameter value. Doing so at each step of the minimization of $\Delta\chi^2_{ND280}$ would be computationally prohibitive. Instead, sufficient information is passed through from NEUT that a weight can be calculated for each event that results in the simulated event sample having the appropriate response to the tuning. However, even this weight calculation procedure is too computationally intensive to perform at each step of the minimization. Instead, before the minimization, for each response parameter relevant to the event, the resulting event weight is computed for various values of the parameter, and these weights as a function of the parameter value are used to produce a cubic spline. This provides the ability to interpolate smoothly between the stored points. In this way, the splines for each response parameter for each event encode the information needed to tune the parameter in a computationally efficient way. Response parameters are therefore labelled "Spline" in Table 6.3.

For both normalization and response parameters, there is a complication arising from the detector composition of ND280 and Super-Kamiokande. For an analysis of neutrino and antineutrino interactions occurring in FGD1 (such as the one described in this chapter), the predominantly polystyrene composition of FGD1 results in the interactions occurring mostly on carbon nuclei. However, at Super-Kamiokande, the detector is filled with water, meaning that the interactions occur mostly on oxygen nuclei. Although some parameters in the model apply to both carbon and oxygen, others are specific to one of those nuclei (and are named to reflect this in Table 6.3). The oxygen-only parameters are unconstrained by ND280 data, though the CC 2p-2h normalization on oxygen is correlated with that on carbon in such a way that the measurement on carbon will result in the central value for oxygen attaining the same value, but the oxygen parameter retaining the prior uncertainty.

With the model sufficiently well parameterized, the prior constraints on the model parameters needed to be determined. The determination of the prior uncertainties for the CCQE parameters included using datasets from the experiments MiniBooNE (neutrinos [13] and antineutrinos [14]) and MINERνA (neutrinos [54] and antineutrinos [53]). The determination of the prior uncertainties for the CCRES parameters included the performance of a re-analysis of the ANL and BNL bubble chamber data [95].

6.2.4 ND280 data, model prediction, and systematic uncertainties

The data used in this analysis consists of 5.82×10^{20} POT of neutrino beam mode data collected between November 2010 and May 2013, and 0.43×10^{20} POT of antineutrino beam mode data, collected in June 2014. The model produces a simulated event sample of approximately 20 times data POT (weighted down to data POT), in order to have a large enough sample to represent the model.

The data and simulated event samples were binned as follows (a total of 531 bins):

- CC-0π (neutrino mode) (154 bins)
  - p (MeV/c): 0, 300, 400, 500, 600, 700, 800, 900, 1000, 1250, 1500, 2000, 3000, 5000, 30000
  - $\cos\theta$: -1.0, 0.6, 0.7, 0.8, 0.85, 0.9, 0.92, 0.94, 0.96, 0.98, 0.99, 1.0
- CC-1π (neutrino mode) (143 bins)

  - p (MeV/c): 0, 300, 400, 500, 600, 700, 800, 900, 1000, 1250, 1500, 2000, 5000, 30000
  - $\cos\theta$: -1.0, 0.6, 0.7, 0.8, 0.85, 0.9, 0.92, 0.94, 0.96, 0.98, 0.99, 1.0

- CC-Other (neutrino mode) (154 bins)
  - p (MeV/c): 0, 300, 400, 500, 600, 700, 800, 900, 1000, 1250, 1500, 2000, 3000, 5000, 30000
  - $\cos\theta$: -1.0, 0.6, 0.7, 0.8, 0.85, 0.9, 0.92, 0.94, 0.96, 0.98, 0.99, 1.0

- $\bar{\nu}_\mu$ CC-1-Track (antineutrino mode) (20 bins)
  - p (MeV/c): 0, 500, 900, 1200, 2000, 10000
  - $\cos\theta$: -1.0, 0.8, 0.92, 0.98, 1.0

- $\bar{\nu}_\mu$ CC-N-Tracks (antineutrino mode) (20 bins)
  - p (MeV/c): 0, 600, 1000, 1500, 2200, 10000
  - $\cos\theta$: -1.0, 0.8, 0.9, 0.97, 1.0

- ν_μ CC-1-Track (antineutrino mode) (20 bins)
  - p (MeV/c): 0, 500, 900, 1200, 2000, 10000
  - $\cos\theta$: -1.0, 0.8, 0.92, 0.98, 1.0

- ν_μ CC-N-Tracks (antineutrino mode) (20 bins)
  - p (MeV/c): 0, 600, 1000, 1500, 2200, 10000
  - $\cos\theta$: -1.0, 0.8, 0.9, 0.97, 1.0

For all samples, this binning is finer in the 2D region with the highest event rates, and coarser in lower event rate regions. This maximizes the ability to use the shape of the distributions to constrain the models, while ensuring that there is sufficient statistics in each bin.

For the neutrino mode samples, the binning used was the same as that used for the previous recent neutrino mode-only analyses (e.g. [7]). This was a reasonable choice to make as the only difference between the data samples used in those analyses and in this one amounts to less than 3% of the data taken in neutrino beam mode.

(The earliest data taken by ND280 was excluded from this analysis, due to challenges in calibrating the data from the, at the time, unfinished ND280 detector).

For antineutrino mode samples, starting from the binning used in similarly low POT earlier ND280 analyses (e.g. [5]), the binning was tuned under the principle that neither the default nor nominal simulated event samples should have less than approximately 1 event in any given bin after they have been weighted down to the data POT. Although a more thorough binning study may have produced a more optimal binning, the relatively small contribution of the antineutrino event mode data resulted in such a study being not a priority.

In Section 5.4, the various contributions to the systematic uncertainty in the ND280 detector model are discussed, along with how they are modelled. However, independently applying these is impractical in this analysis. Although a concerted effort was made to produce a fast implementation of these systematic uncertainties, the time it would take to vary the detector systematic parameters and produce new selection results was still a concern. However, the main issue with the approach described in Section 5.4 concerned the variation systematics. These systematics change the observables of the analysis, and possibly the result of the selection. This results in migration of events between bins, which manifests as a discontinuous jump in the value of $\Delta\chi^2_{ND280}$ for what could be a small variation of a parameter value. Since the MIGRAD algorithm uses the method of gradient descent to find the minimum, such a discontinuous jump presents a problem it cannot solve, and the minimization fails. Therefore, a faster representation of the ND280 systematics without discontinuous migration of events between bins is required.

The effect of adjusting the ND280 detector systematic parameters discussed in Chapter 5 is ultimately to vary the content of the reconstructed p-$\cos\theta$ bins of each of the ND280 samples. Therefore, the effect of the ND280 systematic parameters can be approximated by a set of *observable normalization parameters* (the $\vec{d}$ parameters in Equation 6.4), which apply a multiplicative weight to an event according to its reconstructed p_μ and $\cos\theta_\mu$. The same binning used as the analysis is indeed a natural choice, and what is used for the antineutrino beam mode samples. However, the larger the number of parameters, the longer it takes for MIGRAD to find the minimum of $\Delta\chi^2_{ND280}$, so for the neutrino mode beam samples, the following binning was used for each of the samples (70 bins):

- p (MeV/c): 0, 300, 500, 600, 700, 900, 1000, 1500, 3000, 5000, 30000

- $\cos\theta$: -1.0, 0.6, 0.8, 0.85, 0.9, 0.94, 0.98, 1.0

This coarser binning for the detector systematic observable normalization parameters was used for the ND280 neutrino mode analysis for, for example, [7]. For that analysis, the difference in the response of the analysis between the coarser and the finer binning for these parameters was studied and found to be small. Since this analysis is similar, this coarser binning for these parameters was deemed acceptable for use in this analysis as well.

To determine the nominal values of these 290 observable normalization parameters and their covariance, 2000 simulated event samples were generated by tuning the simulated event sample with different values of the detector systematic parameters discussed in Chapter 5, as well as considering statistical errors resulting from the size of the simulated event sample.

The data, nominal model prediction, and the model prediction tuned with the results of this analysis are compared in Figures 6.9, 6.10, and 6.11, (showing model uncertainties before and after the analysis) and Figures 6.12, 6.13, 6.14, 6.15, 6.16, 6.17 and 6.18 showing the breakdown of the simulated events into individual interaction channels. The contribution of the flux, cross section, and detector uncertainties to the uncertainty in the predicted event rate in each of the ND280 samples before the analysis is shown in Table 6.1. The event rates in each sample (with uncertainties) are provided in Table 6.2.

Sample	Flux (%)	Cross section (%)	Detector (%)
ν_μ CC-0π (ν mode)	8.5	6.5	1.9
ν_μ CC-1π (ν mode)	7.9	12.1	3.0
ν_μ CC-Other (ν mode)	8.3	7.9	6.0
$\bar{\nu}_\mu$ CC-1-Track ($\bar{\nu}$ mode)	8.4	6.6	5.7
$\bar{\nu}_\mu$ CC-N-Tracks ($\bar{\nu}$ mode)	7.4	12.0	8.4
ν_μ CC-1-Track ($\bar{\nu}$ mode)	7.3	8.9	2.5
ν_μ CC-N-Tracks ($\bar{\nu}$ mode)	7.7	10.2	3.4

Table 6.1: Contributions of the flux, cross section, and detector systematic uncertainties to the uncertainty in the predicted event rate of each ND280 sample, before the analysis. Table data for flux and cross section parameter contributions are from [61], while the totals for the detector samples are taken from Tables 5.1,5.2, and 5.3 (whose table data are originally from references [32], [35], and [36], respectively) and rounded to one decimal place.

6.3 Validation

Since nature does not provide a "back of the book" in which to check the result of an analysis for correctness, it is important to verify that an analysis will produce a reasonable result. The various tests that are performed are known as *validations*. This section describes in more detail the validations undertaken for this analysis.

6.3.1 Asimov data set

In the 1955 short story *Franchise* (printed, for example, in [26]) by Isaac Asimov, election results are decided by a computer based on questions it asks of one representative voter. Inspired by this story, Cowan et al. [48] coined the term *Asimov data set* to describe a representative simulated data set used to replace an ensemble of simulated data sets in the determination of the median sensitivity of an experimental measurement. The Asimov data set is defined as the data set in which the contents in each bin equals the expectation.

An analysis of an Asimov data set is a convenient check for bias in the parameter estimation. Indeed, the parameter values returned by this analysis when it is performed on the Asimov data set are all within 10^{-11} of the true parameter value (i.e. not different to much more than machine precision.) The true parameter values and those returned by performing this analysis on the Asimov data set are plotted in Figure 6.2. Although any deviation from the true parameter value is too small to be seen in this figure, it acts as a point of comparison for the Fake data studies discussed in Section 6.3.2. These results indicate that this analysis is performed properly on the Asimov data set, and therefore this validation is considered successful.

6.3.2 Fake data sets

In addition to the Asimov data set, additional fake data sets were analyzed to understand the sensitivity to modified neutrino interaction models. Two fake data sets were considered, named after the models that produced them: "Relativistic RPA" and "Spectral Function".

The Relativistic RPA fake data was generated with the same model and parameter values as the Asimov data set, which produces event rates in each of the samples that are similar to those of the Asimov data set. As a result, one would expect that performing the analysis on this fake data would produce a result similar to that of

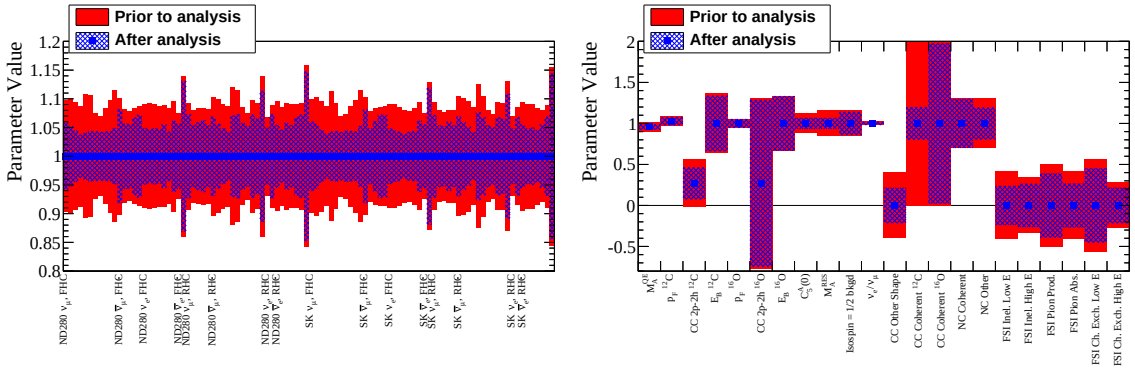

(a) Flux parameters, in the same order as Figure 6.1b, with the starting bin of each category labelled.

(b) Cross section parameters, in the same order as Table 6.3.

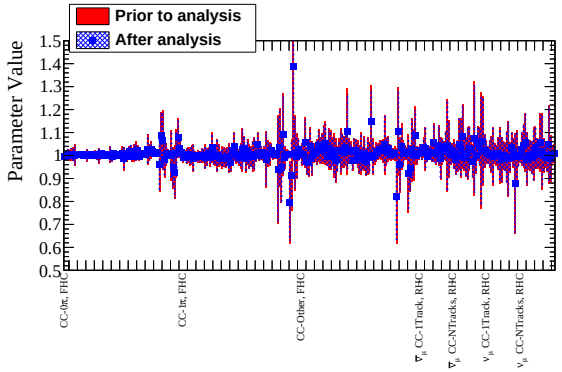

(c) Observable normalization parameters, with the starting bin of each category labelled.

Figure 6.2: Flux, cross section, and observable normalization parameter measurements from this analysis when performed on the Asimov data set.

the analysis of the Asimov data set. Indeed, this is approximately what is seen, as shown in Fig. 6.3.

The Spectral Function fake data uses an alternate model. This model has a higher CCQE event rate than the Relativistic RPA model, which results in a larger number of events in the CC-0π sample for this fake data set. So, successful analysis of this fake data would demonstrate that this analysis can successfully be performed even if the real data is closer to the Spectral Function model than the Relativistic RPA model. Performing the analysis on this fake data set results in the CCQE model parameters and the flux parameters being pulled to increase the CCQE event rate. These results are shown in Fig. 6.4.

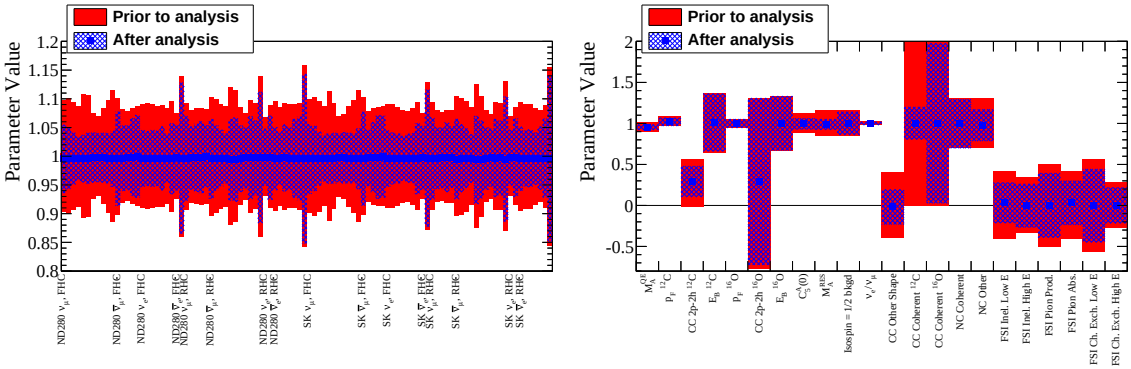

(a) Flux parameters, in the same order as Figure 6.1b, with the starting bin of each category labelled.

(b) Cross section parameters, in the same order as Table 6.3.

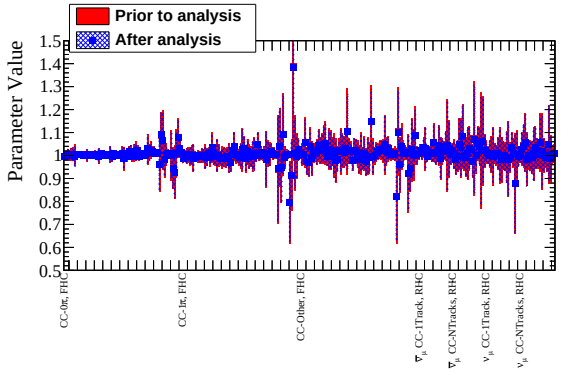

(c) Observable normalization parameters, with the starting bin of each category labelled.

Figure 6.3: Flux, cross section, and observable normalization parameter measurements from this analysis when performed on the Relativistic RPA fake data set.

Since the analysis of these fake data sets agreed sufficiently with expectations, this validation was deemed a success.

6.4 Results and discussion

In this section, the results of this analysis will be reviewed, and the model parameter measurements will be related to the data, nominal model prediction, and the model prediction tuned with the analysis results. The specific deliverables to the oscillation analyses will be featured. In addition, the results of a goodness of fit test will be discussed, and this result will be compared to that of a separate analysis method as

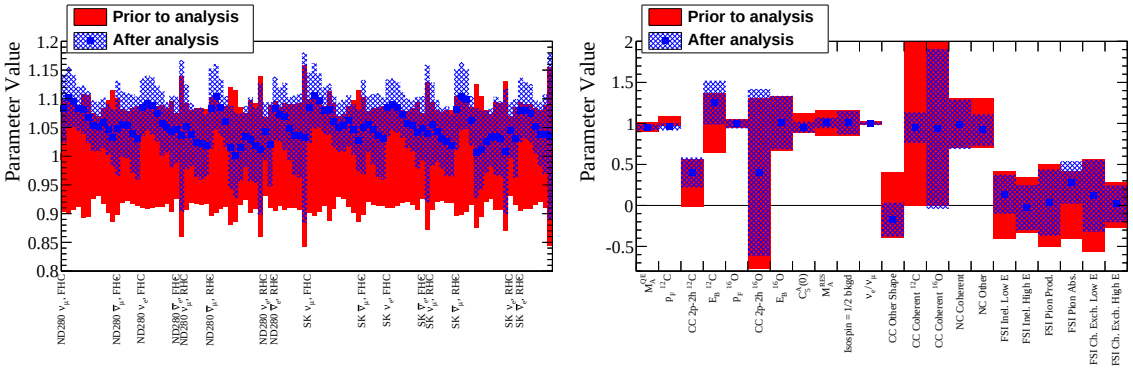

(a) Flux parameters, in the same order as Figure 6.1b, with the starting bin of each category labelled.

(b) Cross section parameters, in the same order as Table 6.3.

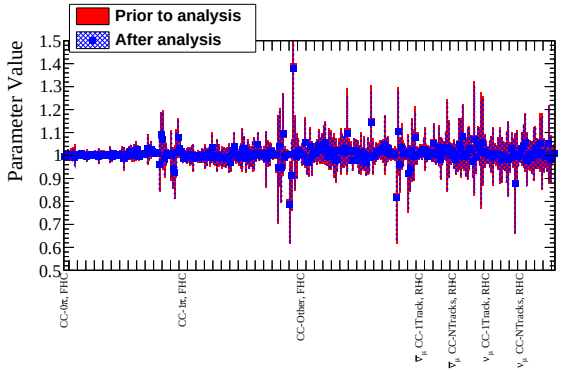

(c) Observable normalization parameters, with the starting bin of each category labelled.

Figure 6.4: Flux, cross section, and observable normalization parameter measurements from this analysis when performed on the Spectral Function fake data set.

a cross check.

6.4.1 Analysis results and deliverables

Once $\Delta\chi^2_{ND280}$ has been minimized, and the covariance matrix of the parameters calculated, the analysis is complete. The ultimate effect of the analysis is to determine the values of the flux, cross section, and detector (observable normalization) parameters that tune the simulated event sample to best resemble the data collected, while taking into account the prior knowledge of the parameters.

Of these parameters, the observable normalization parameters and the FSI cross section parameters are nuisance parameters that are ignored, as discussed in Sec-

tion 6.1. The remaining parameters (ND280 and Super-Kamokande flux parameters, and the remaining cross section parameters) have physical meaning for this analysis and/or constitute deliverables to the oscillation analyses, so will be discussed in more detail.

Sample	Data	Nominal model	Analysis-tuned model
ν_μ CC-0π (ν mode)	17362	15625 ± 1663	17248 ± 133
ν_μ CC-1π (ν mode)	3988	4748 ± 686	4190 ± 60
ν_μ CC-Other (ν mode)	4219	3772 ± 431	4079 ± 62
$\bar{\nu}_\mu$ CC-1-Track ($\bar{\nu}$ mode)	435	387 ± 41	438 ± 13
$\bar{\nu}_\mu$ CC-N-Tracks ($\bar{\nu}$ mode)	136	128 ± 17	129 ± 5
ν_μ CC-1-Track ($\bar{\nu}$ mode)	131	141 ± 15	147 ± 6
ν_μ CC-N-Tracks ($\bar{\nu}$ mode)	145	147 ± 17	144 ± 6

Table 6.2: Data and simulated ("model") event rates, both prior to ("Nominal") and after ("Analysis-tuned") the analysis.

Considering the event rates of the different samples in Table 6.2 for data, nominal model and tuned model demonstrates the key areas where the analysis needed to make changes. For both the CC-0π and CC-Other samples, the nominal model underestimates the event rate in comparison to the data, while for the CC-1π sample, the event rate is overestimated. In order to deal with this, the flux parameters (Figures 6.6 and 6.7) are all increased, driving up the overall event rate. More sample-specific changes come from the cross section parameters (Figure 6.8), as they allow for differences in event rate between the samples. The event rate is further increased in the CC-0π sample (enhanced in the signal CCQE process, as shown in Figure 6.12) by a large increase in the CC 2p-2h ^{12}C normalization. The CCRES parameters (CA_5^{RES}, M_A^{RES}, and Isospin=$\frac{1}{2}$ Background) are all changed in the direction needed to reduce the event rate in the CCRES-enhanced CC-1π sample (Figure 6.13). In addition, CCCOH events tend to be selected into the CC-1π sample, and the analysis greatly reduces their presence relative to the nominal model by a large reduction of the CC Coh ^{12}C normalization parameter. The event rate in the CC-Other sample is increased by the increase in the CC Other Shape parameter, as well as with a large increase in the NC Other normalization parameter. NC Other events would get mis-selected into the CC-Other sample due to multiple pions being produced, one of which being mis-identified as a muon. This increase in NC Other events is shown in Figure 6.14.

Although the antineutrino beam mode samples were included in this analysis

(Figures 6.15, 6.16, 6.17, and 6.18), their relatively small event rates did not give them much constraining power in this analysis. Nonetheless, their inclusion in this analysis ensured that any gross inconsistencies between neutrino and antineutrino beam mode would not go unnoticed, and constituted an important first step in the simultaneous analysis of neutrino and antineutrino beam mode data at ND280.

In addition to the tuning of the central values of the model parameters, the ND280 data was also able to reduce uncertainties on them. This translates into the large reduction in uncertainty in the overall event rates shown in Table 6.2. This is also demonstrated in the comparison between the data and the model before and after the analysis is shown Figures 6.9, 6.10, and 6.11.

Although the improved agreement between the ND280 data and the model, and the reduced uncertainties are satisfying, the main purpose of performing this analysis is to tune the Super-Kamiokande model. As discussed earlier, only the Super-Kamiokande flux parameters and a subset of the cross section parameters (labelled in Table 6.3) are relevant for Super-Kamiokande, so the rest are ignored in the oscillation analysis. Although the strong correlations between the ND280 and Super-Kamiokande flux parameters resulted in similar constraints, many of the cross section parameters (especially those specific to oxygen, and most notably, CC 2p-2h ^{16}O, with a large uncertainty and a large change in central value) were not meaningfully constrained by this analysis.

In addition to the parameter values reported by this analysis, their uncertainties are passed to the oscillation analyses through their covariance matrix. As discussed earlier, although the prior covariances for the flux and cross section parameters were independent, this analysis determines the covariance of the full set of parameters. There are therefore correlations between the flux parameters and the cross section parameters, as they are both capable of changing the event rate in the ND280 samples. For the parameters used in the oscillation analyses, the prior correlation matrix and the correlation matrix determined from this analysis are shown in Figure 6.5. As can be seen there, the correlations between some cross section parameters and the flux parameters can be quite strong, which is therefore important for the oscillation analysis to take into account. The effect of this analysis on the event rates and energy spectrum predicted at Super-Kamiokande (and through them, the oscillation analysis) is discussed in Section 7.5.

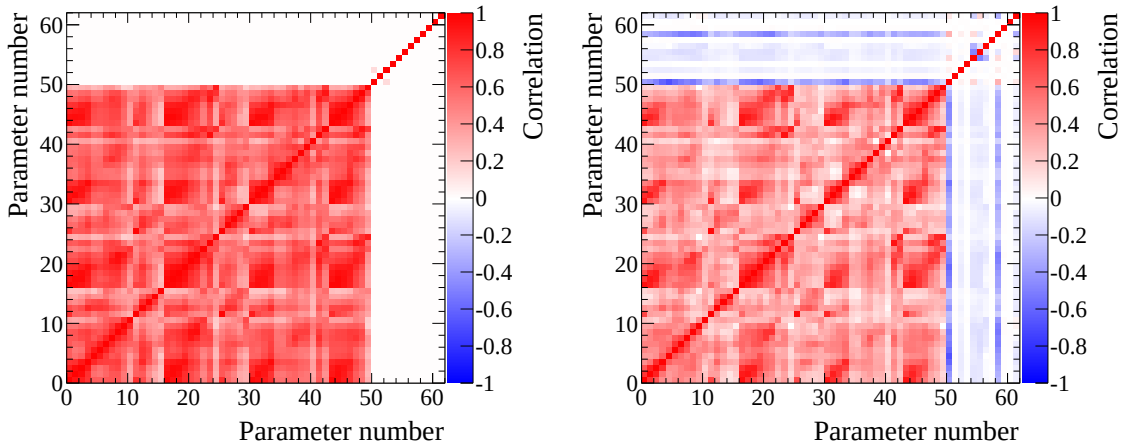

Figure 6.5: Correlation matrices for the parameters passed to the oscillation analyses both before (left) and after (right) the analysis of the ND280 data. Parameters 0-49 are the Super-Kamiokande flux parameters in the same order as Figure 6.1b, and the remaining parameters are the cross section parameters "Used at SK" in the same order as in Table 6.3.

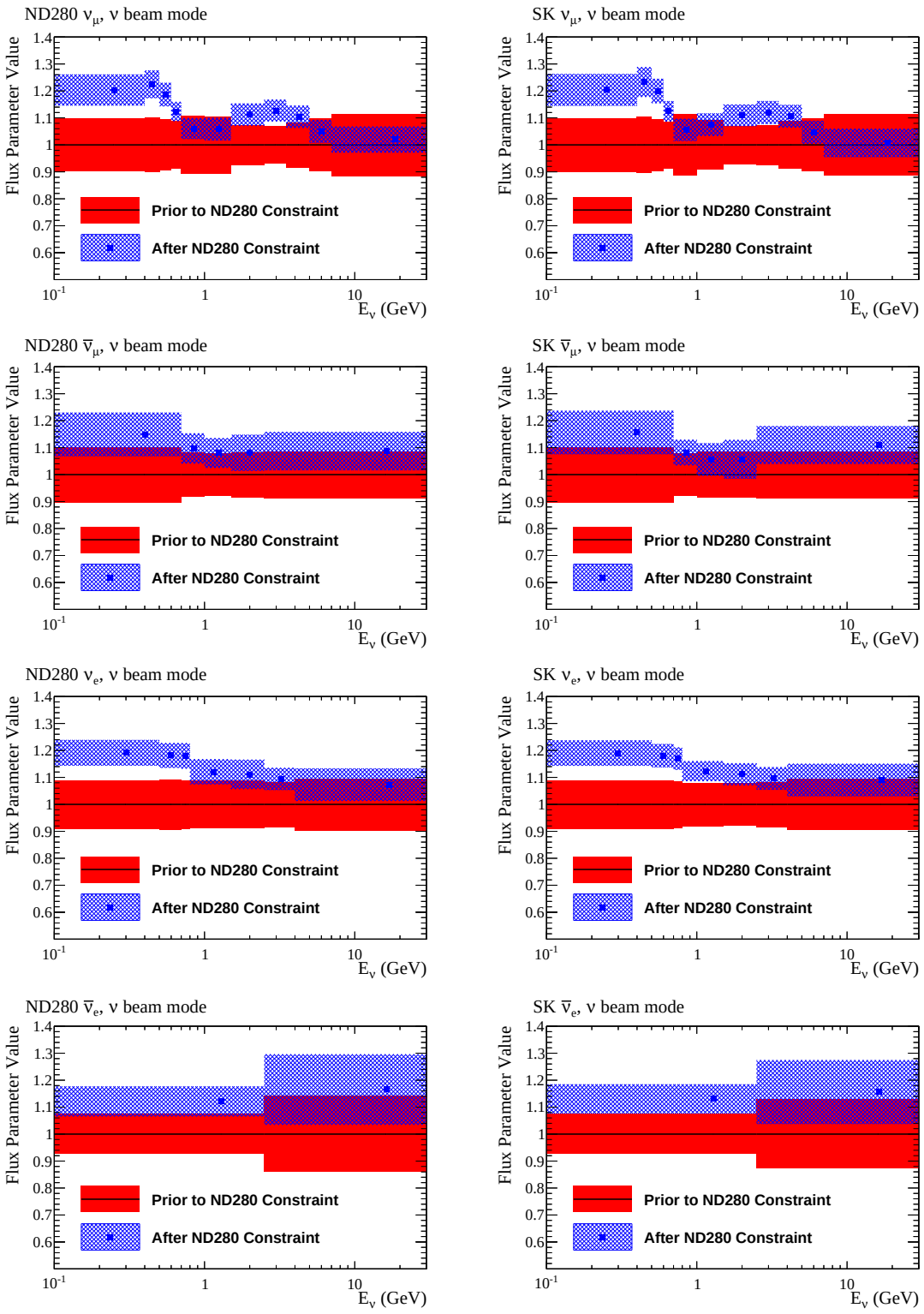

Figure 6.6: Values and uncertainties of the neutrino mode flux parameters for ND280 and Super-Kamiokande, prior to and after the analysis.

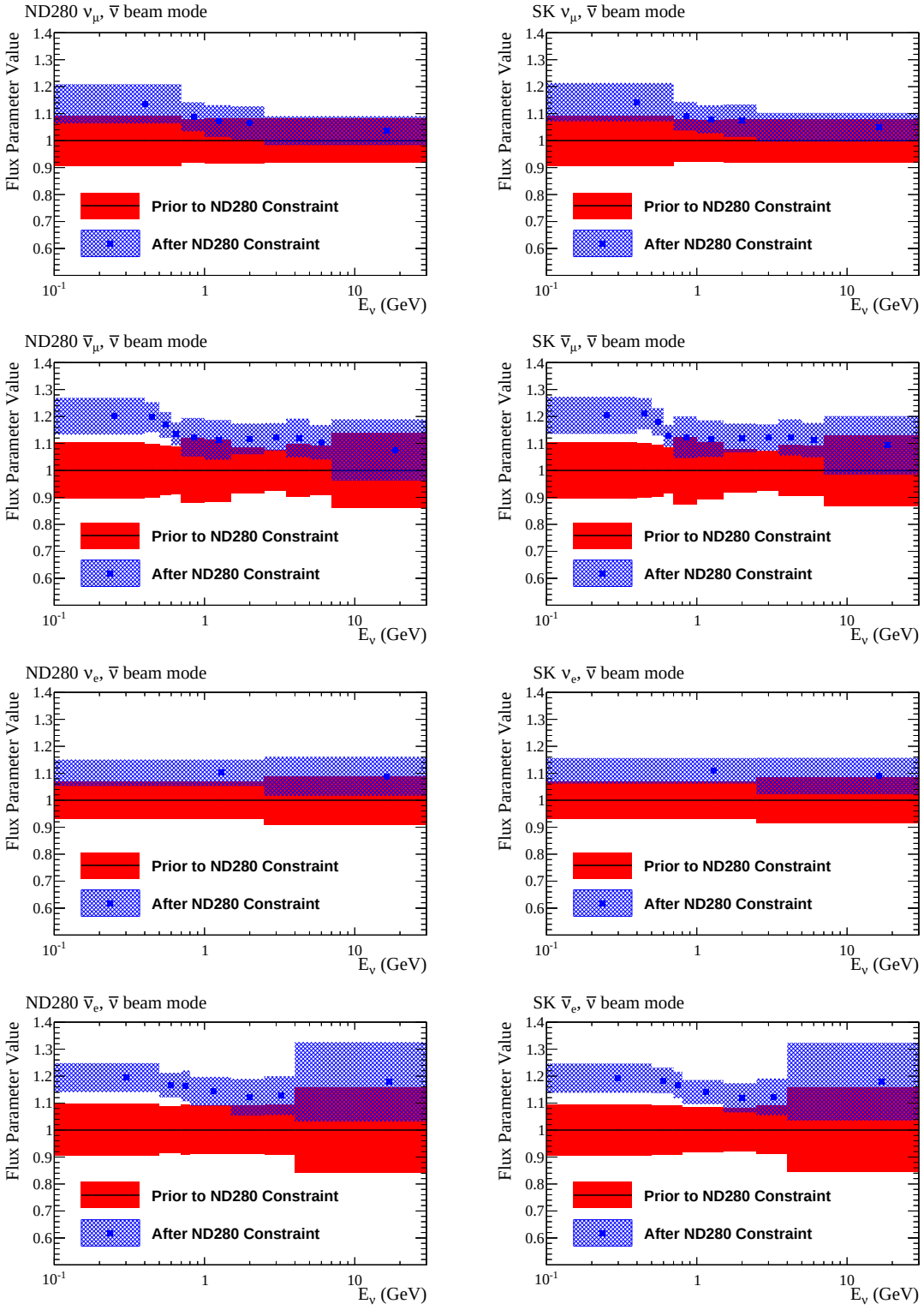

Figure 6.7: Values and uncertainties of the antineutrino mode flux parameters for ND280 and Super-Kamiokande, prior to and after the analysis.

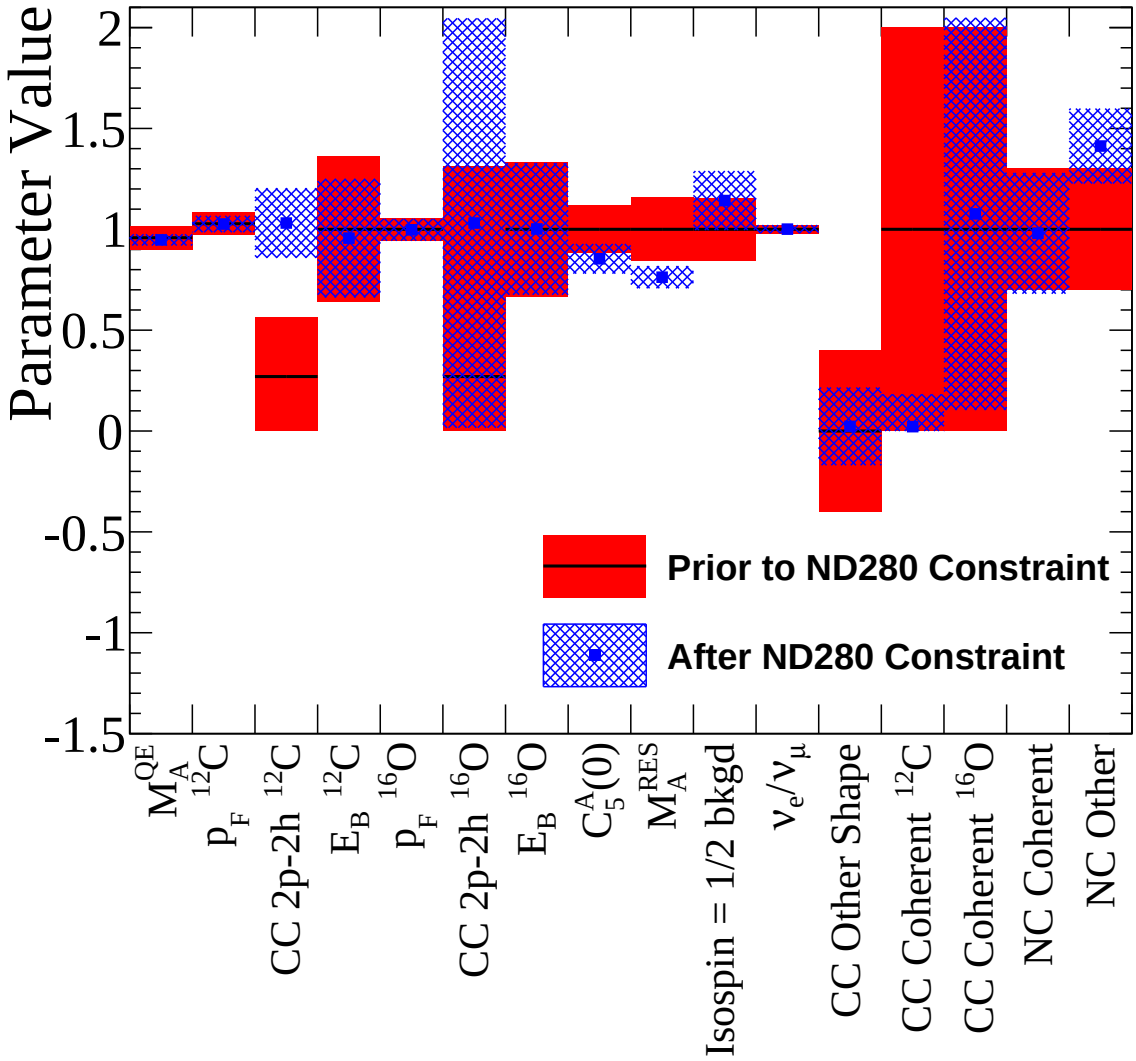

Figure 6.8: Values and uncertainties of the cross section parameters prior to and after the analysis.

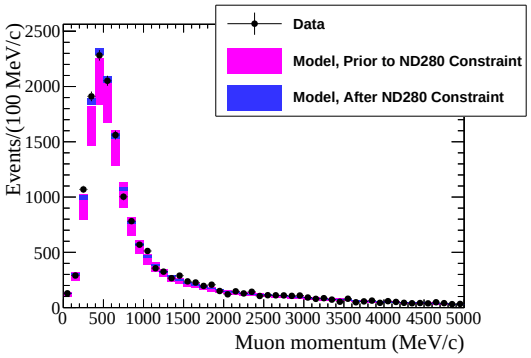

(a) CC-0π, muon momentum

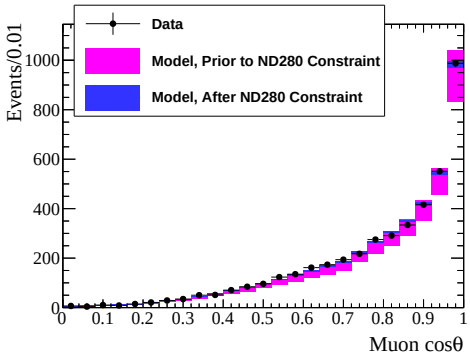

(b) CC-0π, muon $\cos\theta$

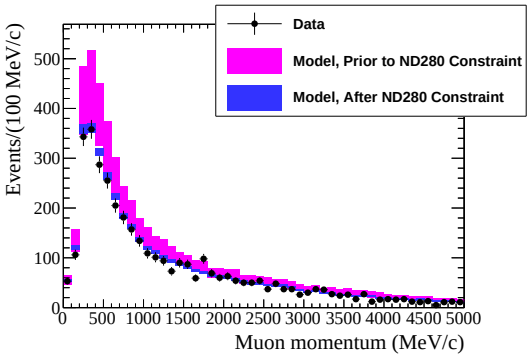

(c) CC-1π, muon momentum

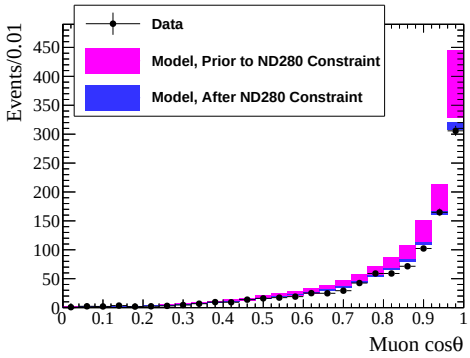

(d) CC-1π, muon $\cos\theta$

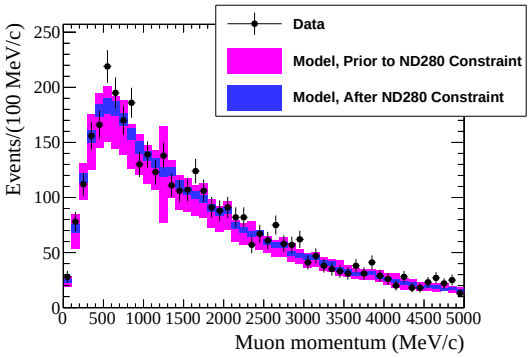

(e) CC-Other, muon momentum

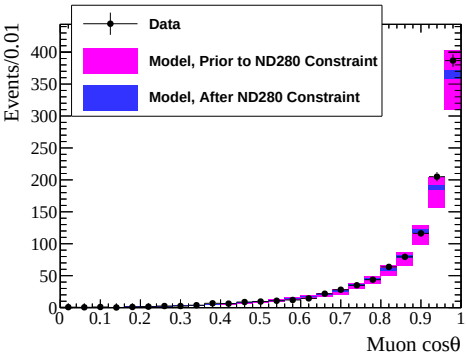

(f) CC-Other, muon $\cos\theta$

Figure 6.9: Momentum and angular projections of the neutrino mode samples, showing the uncertainty in each bin due to combined flux, cross section, and detector systematic uncertainties, before and after the analysis.

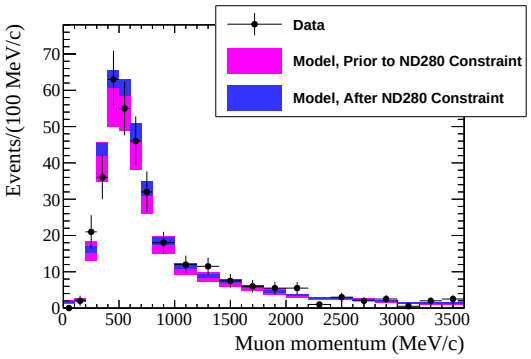

(a) $\bar{\nu}_\mu$ CC-1-Track, muon momentum

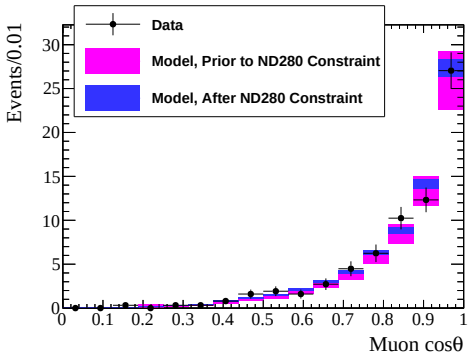

(b) $\bar{\nu}_\mu$ CC-1-Track, muon $\cos\theta$

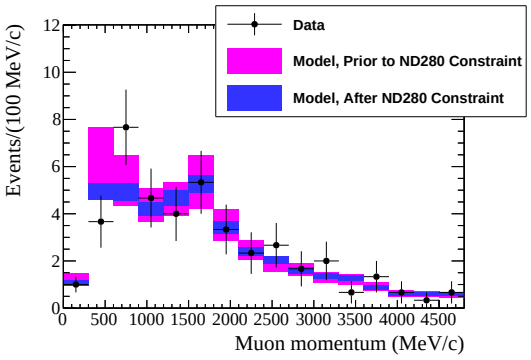

(c) $\bar{\nu}_\mu$ CC-N-Tracks, muon momentum

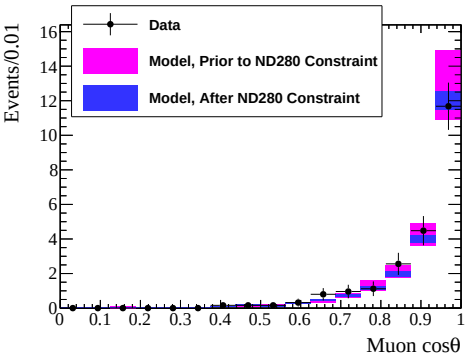

(d) $\bar{\nu}_\mu$ CC-N-Tracks, muon $\cos\theta$

Figure 6.10: Momentum and angular projections of the antineutrino mode muon antineutrino samples, showing the uncertainty in each bin due to combined flux, cross section, and detector systematic uncertainties, before and after the analysis.

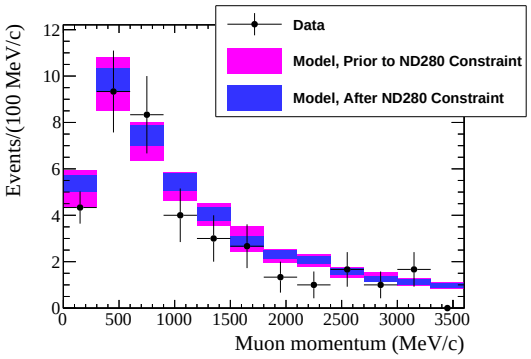

(a) ν_μ CC-1-Track, muon momentum

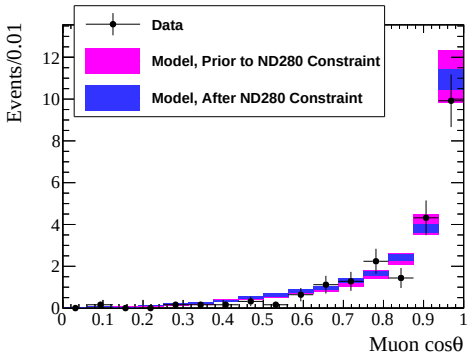

(b) ν_μ CC-1-Track, muon $\cos\theta$

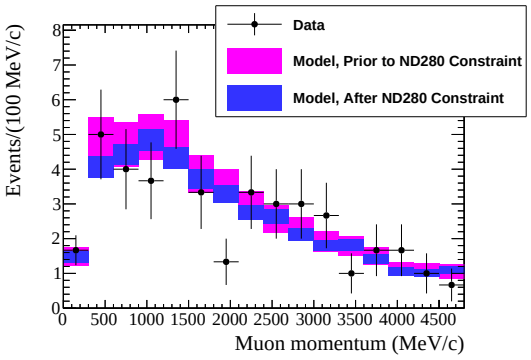

(c) ν_μ CC-N-Tracks, muon momentum

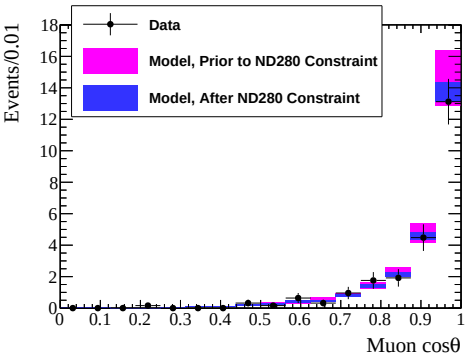

(d) ν_μ CC-N-Tracks, muon $\cos\theta$

Figure 6.11: Momentum and angular projections of the antineutrino mode muon neutrino samples, showing the uncertainty in each bin due to combined flux, cross section, and detector systematic uncertainties, before and after the analysis.

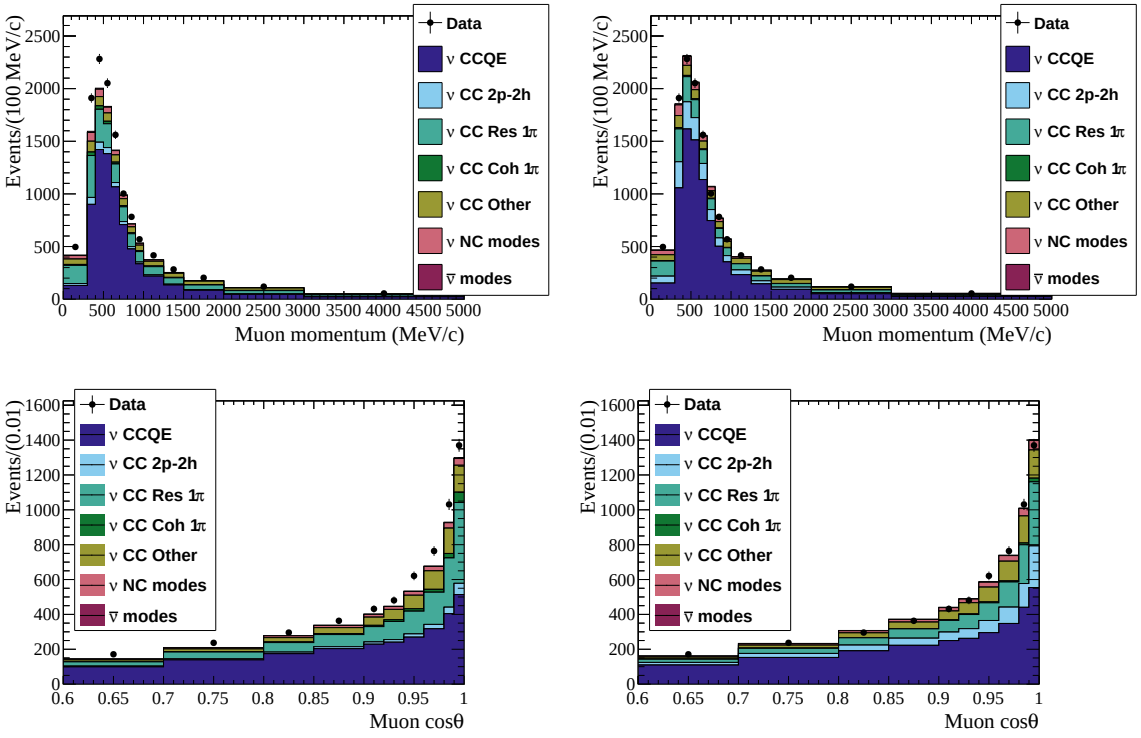

Figure 6.12: Data and simulated event sample momentum and angular projections of the CC-0π sample (neutrino mode), before (left) and after (right) the analysis, with the simulated event sample broken down by interaction channel.

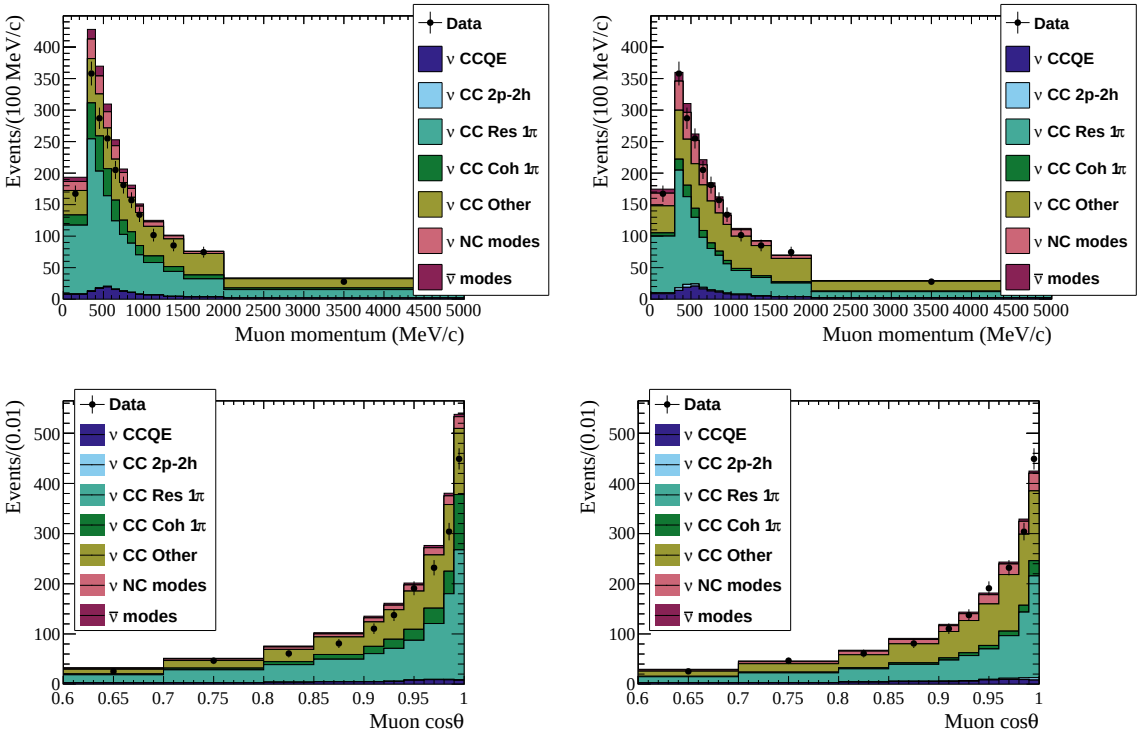

Figure 6.13: Data and simulated event sample momentum and angular projections of the CC-1π sample (neutrino mode), before (left) and after (right) the analysis, with the simulated event sample broken down by interaction channel.

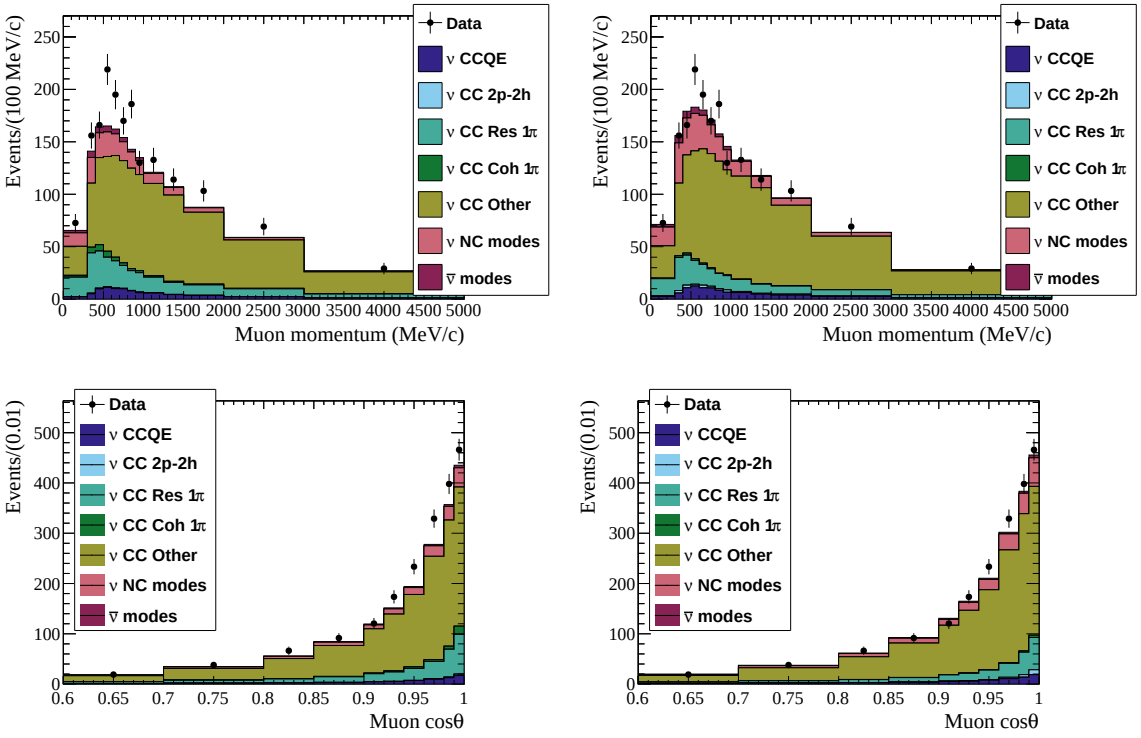

Figure 6.14: Data and simulated event sample momentum and angular projections of the CC-Other sample (neutrino mode), before (left) and after (right) the analysis, with the simulated event sample broken down by interaction channel.

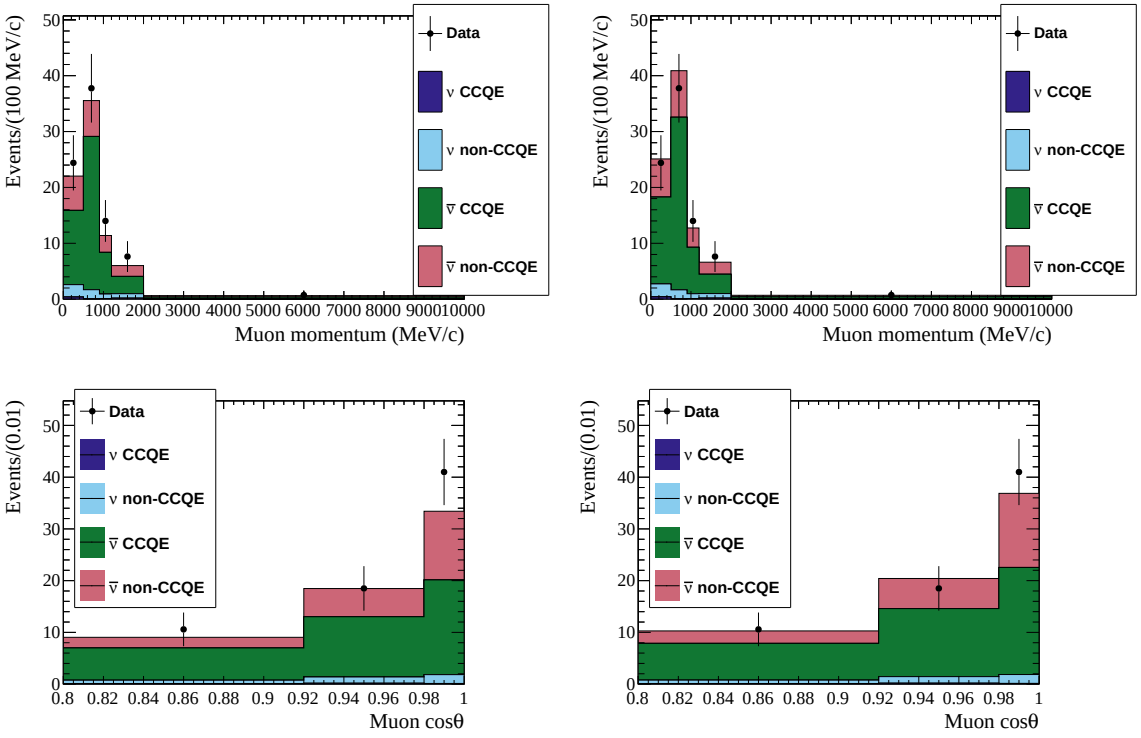

Figure 6.15: Data and simulated event sample momentum and angular projections of the $\bar{\nu}_\mu$ CC-1-Track sample (antineutrino mode), before (left) and after (right) the analysis, with the simulated event sample broken down by interaction channel.

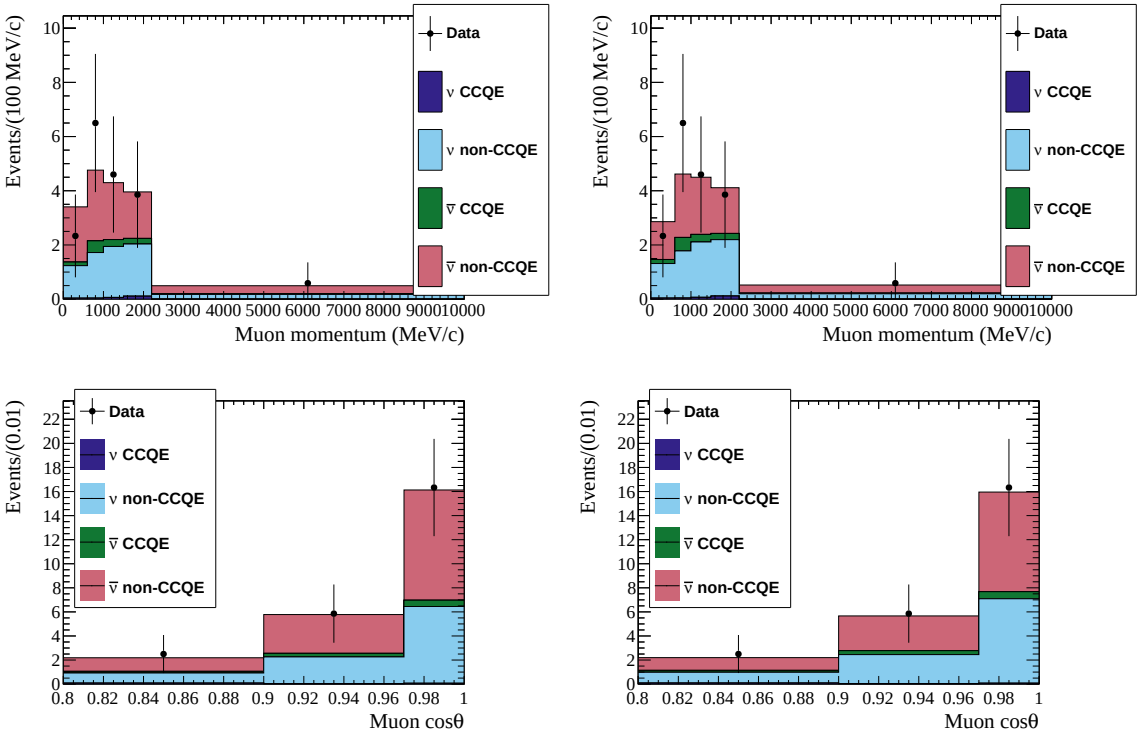

Figure 6.16: Data and simulated event sample momentum and angular projections of the $\bar{\nu}_\mu$ CC-N-Tracks sample (antineutrino mode), before (left) and after (right) the analysis, with the simulated event sample broken down by interaction channel.

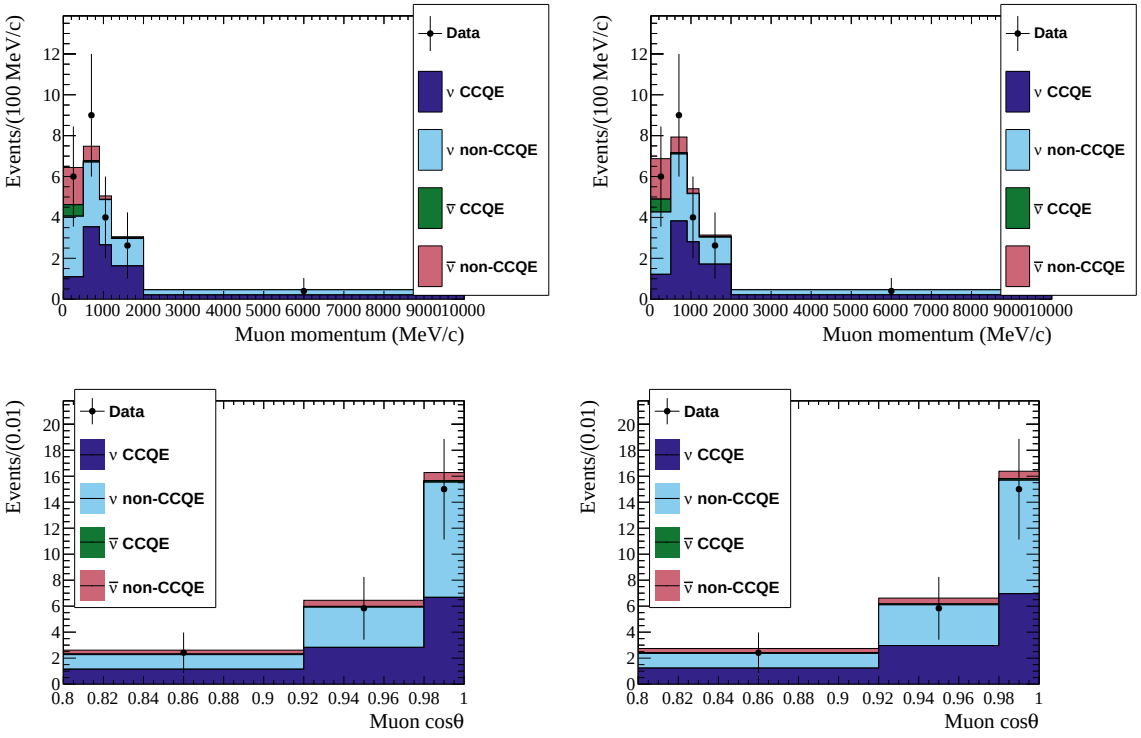

Figure 6.17: Data and simulated event sample momentum and angular projections of the ν_μ CC-1-Track sample (antineutrino mode), before (left) and after (right) the analysis, with the simulated event sample broken down by interaction channel.

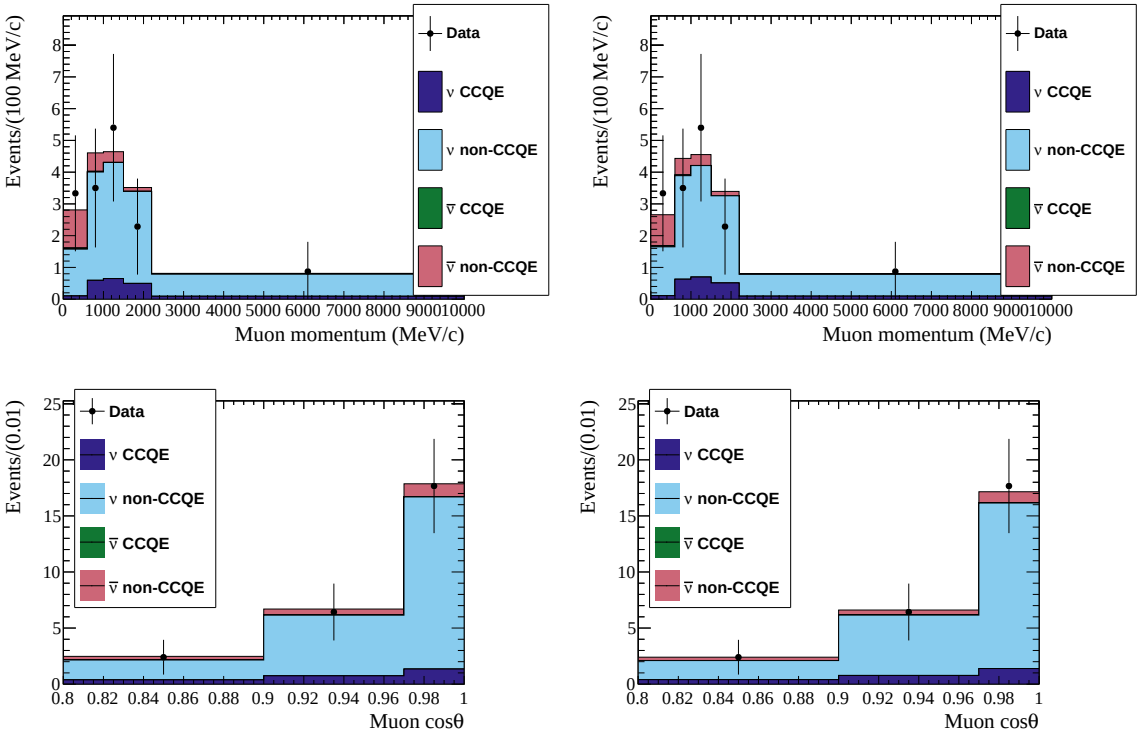

Figure 6.18: Data and simulated event sample momentum and angular projections of the ν_μ CC-N-Tracks sample (antineutrino mode), before (left) and after (right) the analysis, with the simulated event sample broken down by interaction channel.

Parameter	Before analysis	After analysis	Calculation	Used at SK
M_A^{QE} (GeV/c^2)	1.15 ± 0.07	1.14 ± 0.03	Spline	Yes
p_F ^{12}C (MeV/c)	223 ± 12	222.7 ± 8.8	Spline	No
CC 2p-2h ^{12}C	27 ± 29	103 ± 17	Norm	No
E_B ^{12}C (MeV)	25 ± 9	23.9 ± 7.3	Spline	No
p_F ^{16}O (MeV/c)	225 ± 12	224 ± 12	Spline	Yes
CC 2p-2h ^{16}O	27 ± 104	103 ± 101	Norm	Yes
E_B ^{16}O (MeV)	27 ± 9	27.0 ± 8.8	Spline	Yes
CA_5^{RES}	1.01 ± 0.12	0.86 ± 0.07	Spline	Yes
M_A^{RES} (GeV/c^2)	0.95 ± 0.15	0.72 ± 0.05	Spline	Yes
Isospin=$\frac{1}{2}$ Background	1.3 ± 0.2	1.49 ± 0.19	Spline	Yes
ν_e/ν_μ	1.00 ± 0.02	1.00 ± 0.02	Spline	Yes
CC Other Shape	0.0 ± 0.4	0.02 ± 0.19	Spline	Yes
CC Coh ^{12}C	1.0 ± 1.0	0.02 ± 0.16	Norm	No
CC Coh ^{16}O	1.0 ± 1.0	1.08 ± 0.97	Norm	Yes
NC Coh	1.0 ± 0.3	0.98 ± 0.30	Norm	Yes
NC Other	1.0 ± 0.3	1.41 ± 0.19	Norm	Yes
FSI Inel. Low E	0.00 ± 0.41	-0.31 ± 0.15	Spline	No
FSI Inel. High E	0.00 ± 0.34	0.12 ± 0.24	Spline	No
FSI Pion Prod.	0.00 ± 0.50	-0.18 ± 0.35	Spline	No
FSI Pion Abs.	0.00 ± 0.41	-0.07 ± 0.24	Spline	No
FSI Ch. Exch. Low E	0.00 ± 0.57	0.67 ± 0.43	Spline	No
FSI Ch. Exch. High E	0.00 ± 0.28	-0.10 ± 0.19	Spline	No

Table 6.3: Cross section parameter values before and after the ND280 analysis. Parameters used at Super-Kamiokande in the oscillation analysis are identified as such. Whether a parameter is applied as a normalization, or requires calculation of a response function (a cubic spline) is also indicated.

6.4.2 Goodness of fit

As discussed in Section 6.1, the minimized quantity $\Delta\chi^2_{ND280}$ is expected to follow a χ^2 distribution, giving a natural measure of goodness of fit in the p-value of this analysis result. In order to determine the p-value, the value of $\Delta\chi^2_{ND280}$ for 398 toy fake data analysis results (*toy experiments*) are considered. These toy experiments were generated by choosing values for the flux, cross section, and detector systematic parameters according to their covariance, and using these values to tune the simulated event sample. In order to best approximate the expected response of the ND280 detector systematics, instead of tuning the observable normalization ($\vec{d}$) parameters used in this analysis, these toy experiments are generated by tuning the detector systematic parameters dicussed in Section 5.4. In determining the content of each bin of each toy experiment, each event weight was multiplied by the result of a draw from a Poisson distribution of mean 1, in order to account for statistical uncertainty due to the finite size of the simulated event sample. Once the bin content was determined, its value was used as the mean of a Poisson distribution from which the final bin content was drawn, in order to model the statistical uncertainty in each bin.

The fraction of these toy analyses with $\Delta\chi^2_{ND280}$ greater than that found for the analysis of data is the p-value of this analysis result. A p-value of 0.05 was chosen prior to this procedure as the p-value below which the appropriateness of the model would be questioned. The resulting $\Delta\chi^2_{ND280}$ distribution of the toy experiments is shown in Figure 6.19, with the result of the analysis of the data overlaid. The corresponding p-value is just above 0.05, and therefore acceptable.

The astute reader may notice that the distribution shown in Figure 6.19 is flatter with a longer tail to high values than a χ^2 distribution with the same mean would be. This is an artifact of the two different ways of treating the ND280 detector systematic uncertainties. As mentioned earlier in this section, the toy experiments were generated using the treatment of the ND280 detector systematics discussed in Section 5.4, while the analysis uses the observable normalization parameter treatment discussed in Section 6.2.4. This means that the toy experiments more accurately represent the ND280 detector systematics, but any non-Gaussian features in their response, when analyzed under the assumption of the Gaussian observable normalization parameters, results in the distortion of this distribution. For comparison, Figure 6.20 shows that if the toy experiments are generated with the observable normalization parameter treatment of the ND280 detector systematics, the resulting distribution is

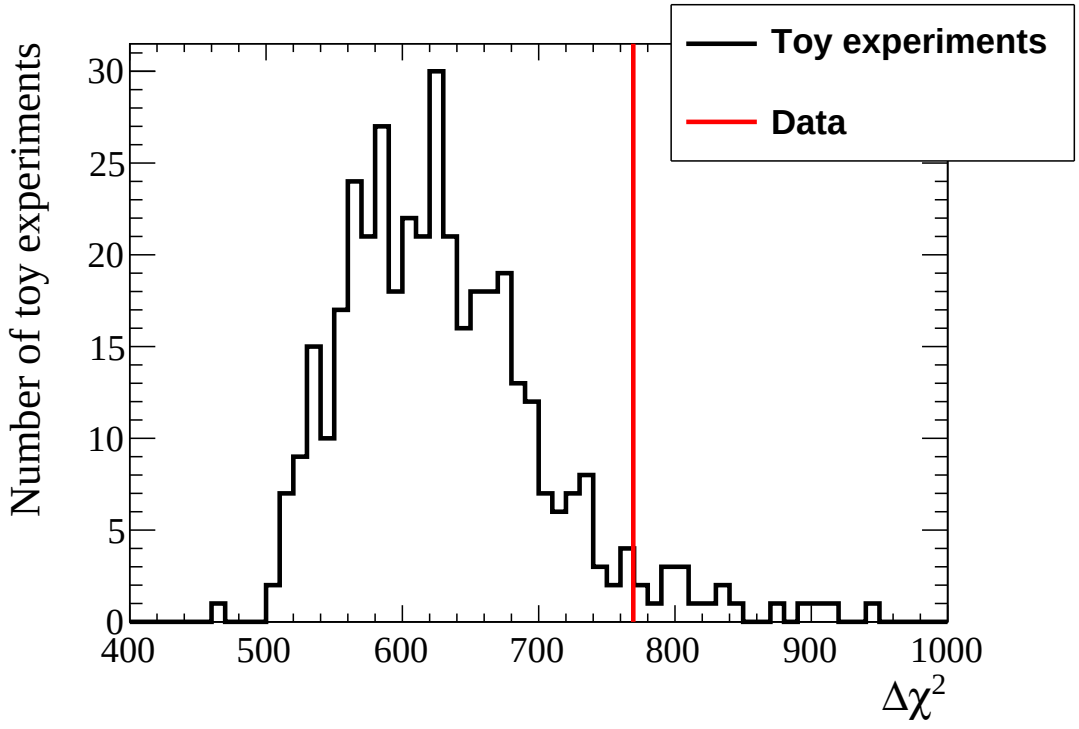

Figure 6.19: The distribution of $\Delta\chi^2_{ND280}$ values from performing the analysis on 398 toy experiments, with the value from the analysis of the data superimposed.

the properly shaped χ^2 that is expected.

6.4.3 Comparison to alternative analysis method

In addition to the analysis described here, there another analysis was performed that uses a Markov Chain Monte Carlo (MCMC) method to measure neutrino oscillation parameters by simultaneously analyzing ND280 and Super-Kamiokande data. The MCMC analysis can be restricted to considering only ND280 data, making it an independent cross-check, albeit using the same inputs (flux, cross section, and detector systematics, and event selection code.) A comparison of the results of the two analyses is shown in Fig. 6.21. There is good agreement between the results of the two analyses, suggesting that neither method is less valid than the other.

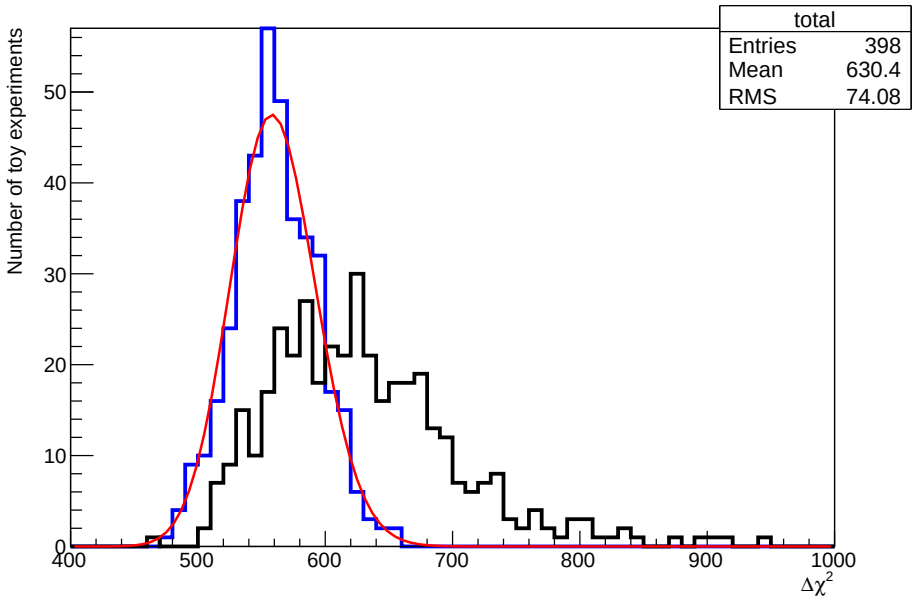

Figure 6.20: A demonstration that the deviations from a χ^2 distribution of the $\Delta\chi^2$ of the toy experiments used in the goodness of fit test (in black, from Figure 6.19) is due to the observable normalization parameters being an imperfect approximation of the response of the detector systematic parameters. When toy experiments are generated using the observable normalization treatment instead, the blue distribution is produced, which is much closer to the expected χ^2 shape, superimposed in red.

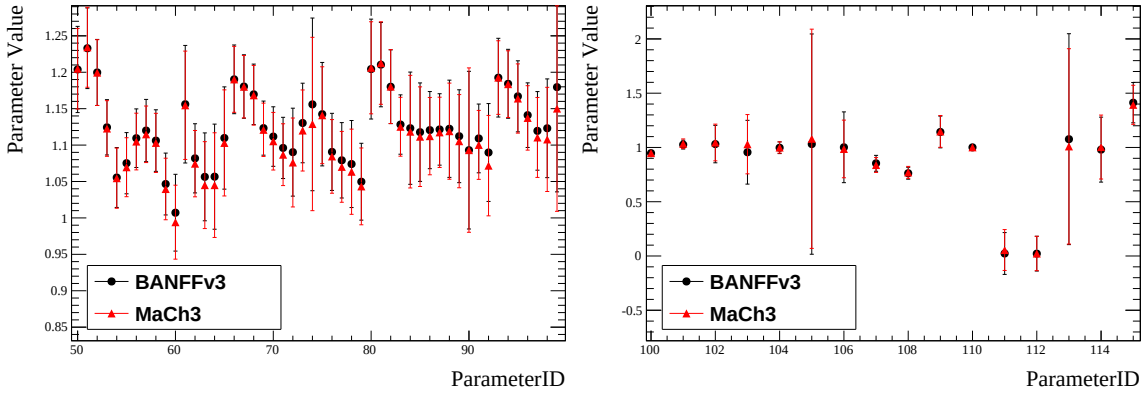

(a) Comparison of SK flux parameter measurements, with same parameter numbering as in Figure 6.1b.

(b) Comparison of cross section parameter measurements (as fractions of the default model value, where appropriate), in the same order as Table 6.3, excluding FSI.

Figure 6.21: Comparison between the results of this analysis (denoted BANFFv3) and the results of an alternate analysis (denoted MaCh3), showing good agreement between the two different analysis methods. From [61].

Chapter 7

Event selection at Super-Kamiokande and the oscillation analysis

As described in Chapter 3, the experiment is setup in order to maximize muon neutrino disappearance at Super-Kamiokande. Muon antineutrino disappearance is revealed by a deficit of muon antineutrinos at Super-Kamiokande, relative to the model prediction (that is to say, the muon antineutrinos are observed to have disappeared). This chapter describes how muon antineutrino events are selected, how systematic uncertainties are treated, and finally, how antineutrino oscillation parameters are estimated, and the results of this measurement [21].

7.1 Event selection

As discussed in Section 3.1, the probability of muon antineutrino disappearance is strongly dependent on the antineutrino energy. Therefore, accurately reconstructing the energy of the muon antineutrinos that interact in the detector is of paramount importance. To this end, the Super-Kamiokande event selection aims to select events where the true interaction type was CCQE, and where the relevant kinematic variables for energy reconstruction can be accurately measured (outgoing muon momentum and angle, as shown in Eq. 2.13).

The event selection begins by requiring that an event be what is referred to as a *Fully Contained Fiducial Volume* or "FCFV" event, that occurs in a window (-2 μs

to 10 μs) around the arrival of the beginning of a J-PARC beam spill at Super-Kamiokande. The definition of the FCFV sample used as the starting point for the T2K selections originates in the Super-Kamiokande atmospheric neutrino analyses. This allows T2K to benefit from the experience of the Super-Kamiokande atmospheric neutrino program.

The first part of the FCFV selection involves selecting events that are *Fully Contained*. As discussed in Section 3.4, Super-Kamiokande is divided into two separate volumes: the Inner Detector (ID), which is heavily instrumented to study the events within it, and the Outer Detector (OD), which helps veto external backgrounds. For an event to be Fully Contained, all of its outgoing particles must remain inside the ID. This is checked by looking for charge deposition in the OD, and requiring that the number of PMTs in the highest charge cluster in the OD is less than 16. A Fully Contained ("FC") event therefore is contained in a region where it can be best measured, and is less likely to be a background event from outside the detector that was mistaken for an event inside the ID.

The second part of the FCFV selection involves restricting consideration to only those FC events that can be accurately reconstructed. Of concern is that a neutrino interaction taking place too close to the PMTs may be difficult to reconstruct properly. So, a *Fiducial Volume* is defined, within which there is confidence in the reconstruction algorithm. The Fiducial Volume ("FV") is defined as a virtual cylinder inside the ID, whose walls are 200 cm from the interior walls of the ID. Therefore, an FC event is in the FV if its vertex is at least 200 cm from the nearest ID wall. Finally, the FCFV sample also requires that the sum of all visible energy from reconstructed Cherenkov rings is greater than 30.0 MeV (that is to say, enough energy is deposited in the PMTs to be confident in what they reconstruct as an event, which excludes low energy backgrounds).

To understand the size of the backgrounds and the effectiveness of the FCFV selection, consider the earlier neutrino mode analysis described in [8]. To summarize its description of backgrounds, events with sufficiently large OD activity (such as cosmic rays) occurred at roughly the same rate as beam events would in a 20 μs time bin after the beam arrival time, and low energy background events in the ID (such as those due to radioactivity) were roughly 10 times more frequent. Nonetheless, of the 377 events that were classified as FCFV in that analysis, only 0.0085 were expected to be due to background events that were not produced by the T2K beam.

Once the FCFV sample has been obtained, a series of additional selection cuts

are applied in order to arrive at a useful event sample. In the case of this analysis, a sample enriched in $\bar{\nu}_\mu$ CCQE interactions is desired.

To start, it is required that only one Cherenkov ring is reconstructed. This cut is meant to remove both Charged Current ("CC") events where a charged particle above Cherenkov threshold was produced in addition to the muon (e.g. CCRES), and Neutral Current events where pions were produced, which decayed into particles producing multiple rings in the detector.

Once in possession of an FCFV sample with one Cherenkov ring, it is required that this Cherenkov ring be identified as muon-like, as described in Section 3.4. This cut is meant to specifically select interactions where a muon was produced (instead of an electron), thus selecting for $\bar{\nu}_\mu$ CC interactions.

The next selection cut that is performed on the sample is to require that the muon candidate's reconstructed momentum (as described in Section 3.4) is greater than 200 MeV/c. This cut is necessary for optimal performance of the particle identification algorithm. It also reduces contamination due to events where the muon was below Cherenkov threshold.

The final selection cut requires that the number of Michel electrons observed is less than or equal to one. As described in Section 3.3.2, a Michel electron is the electron produced by the decay of a muon, which results in delayed charge deposited in the detector. Since the outgoing muon in the sample at this point is indeed supposed to stop within the detector, the one decay electron allowed by this cut is necessary to not cut out good $\bar{\nu}_\mu$ CC events. However, if charged pions were produced in the neutrino interactions and were below Cherenkov threshold, they could decay to muons which would subsequently decay to produce Michel electrons. Therefore, this cut allows true CCQE events to pass the selection, while reducing the contamination from CC events containing additional charged pions that did not produce Cherenkov rings.

In summary, the following sequence of selection cuts is applied in order to preferentially select $\bar{\nu}_\mu$ CCQE events in antineutrino beam mode.

1. Is a Fully Contained Fiducial Volume (FCFV) event.
2. Only one Cherenkov ring is found.
3. The Cherenkov ring is identified as muon-like.
4. The muon candidate's reconstructed momentum is greater than 200 MeV/c.
5. The number of Michel electrons observed is less than or equal to one.

It should be noted that this event selection cannot discriminate between μ^+ (originating from a $\bar{\nu}_\mu$ CC interaction) and μ^- (originating from a ν_μ CC interaction.) The reason that these selection cuts result in selecting mostly $\bar{\nu}_\mu$ CC interactions arises from this selection being performed in antineutrino beam mode. Any ν_μ CC interactions (due to ν_μ in the beam) satisfying these cuts are selected into this sample.

Detector systematic uncertainties are calculated for the event selection. The sizes of these uncertainties are arrived at by comparing data and the model prediction for Super-Kamiokande atmospheric neutrino and cosmic ray muon control samples. How these uncertainties are propagated in the oscillation analysis is discussed in Section 7.3.

7.2 The model

Neutrino interactions within the Super-Kamiokande detector are simulated using NEUT 5.3.2 [62], with input from the beam simulation as to the expected neutrino flux. The response of Super-Kamiokande to the outgoing particles from these interactions is simulated with SKDETSIM v13p90, which is based on GEANT3 [42]. This is then processed by the 14b SuperK software. A sample was generated for each neutrino flavour ($\bar{\nu}_\mu$, $\bar{\nu}_e$, ν_μ, and ν_e) using the nominal flux model (i.e. assuming no neutrino oscillations and nominal systematic parameter values). In addition, the nominal $\bar{\nu}_\mu$ and ν_μ fluxes are used to create samples that represent neutrino oscillation producing $\bar{\nu}_e$ and ν_e, respectively.

Like the ND280 analysis described in Chapter 6, the oscillation analysis requires making a comparison between the observed data and the model prediction, for various model parameter values. In the case of the oscillation analysis, this comparison is done using the distribution of reconstructed neutrino energy, as this is the variable most relevant for estimating neutrino oscillation parameters.

However, in order to properly handle neutrino flux and cross section systematic effects (Section 7.3), more information from the model must be considered in the analysis: the true energy of the neutrino, its true flavour, and the true reaction mode. This is accomplished by performing the event selection described in Section 7.1 on the simulated events, constructing *templates*, which are two dimensional histograms binned in reconstructed neutrino energy and true neutrino energy. One template is generated for each reaction mode (CCQE, CC 2p-2h, CC1π, CC Coherent, CC Other, NC 1$\pi^\pm$, NC 1π^0, NC Coherent, and NC Other) for each of the neutrino flavours mentioned

earlier in this section (unoscillated $\bar{\nu}_\mu$, $\bar{\nu}_e$, ν_μ, ν_e). For oscillated $\bar{\nu}_e$ and oscillated ν_e, only CC templates are included. This is because all flavours will interact similarly under NC processes, so the NC templates would not change under neutrino oscillations. In addition, there are no ν_τ or $\bar{\nu}_\tau$ templates. Although they are similarly included in the NC templates, CC interactions for them would have an energy threshold around 3.5 GeV, which has a negligible effect on this analysis. This provides a total of 46 templates, each divided into 84 true energy bins and 73 reconstructed energy bins. The reconstructed energy binning of the templates is the same as the binning used for the data. As a result, summing over the true energy bins and the templates produces the model prediction for a given reconstructed energy bin, which is compared to the data observation in the analysis discussed in Section 7.4.

Using the oscillation parameter values in Table 7.3, and grouping some related templates together, the model prediction separated into groups of reaction modes is shown in Figure 7.1. Although this distribution is dominated by the signal $\bar{\nu}_\mu$ CCQE, there are indeed large contributions from the other reaction modes, as well as so-called "wrong sign" events due to ν_μ in the antineutrino beam. This underscores the importance of understanding and properly handling the model uncertainties in the beam flux, cross sections, and detector response, which is discussed in the next section.

7.3 Treatment of systematic uncertainties

As described in Section 6.1, uncertainties in the neutrino beam flux model, the cross section model, and in the detector model give rise to uncertainties in the event rate predicted at Super-Kamiokande, and therefore need to be considered in the oscillation analysis.

7.3.1 Flux model uncertainties

As discussed in Section 6.2.2, the beam simulation provides 100 correlated flux parameters, 50 for ND280 and 50 for Super-Kamiokande, that provide a normalization weight for bins of true neutrino energy for ν_μ, ν_e, $\bar{\nu}_\mu$ and $\bar{\nu}_e$ in both beam modes. The beam model also provides constraints on these parameters from external data, and the correlations between them. The ND280 measurement provides a further constraint on these parameters, along with updated correlations between them and with the cross

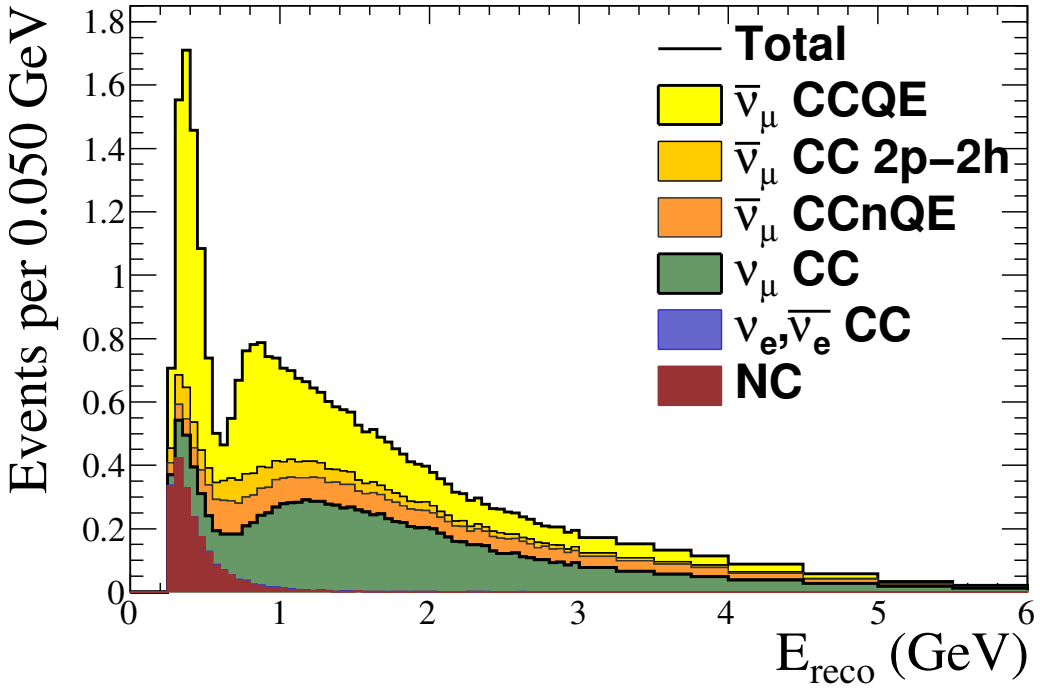

Figure 7.1: The model prediction for the Super-Kamiokande reconstructed neutrino energy spectrum, separated into groups of reaction modes. Neutrino oscillations with parameter values given in Table 7.3 have been applied. From [93] (T2K official plots associated with [21]), with modified legend.

section model parameters. Since the only Super-Kamiokande data being considered in this oscillation analysis is from antineutrino beam mode, only the 25 antineutrino beam mode Super-Kamiokande flux parameters are applicable to the bin contents of the templates. Since the true neutrino energy binning for the templates is much finer than the binning of the flux parameters, the applicable flux parameter for a given true neutrino energy bin is applied as a multiplicative weight to the corresponding bins in the templates.

7.3.2 Cross section model uncertainties

As discussed in Section 6.2.3, the neutrino interaction cross section model provides a number of parameters that can be tweaked, and constraints on them based on external data (including correlations between them). In addition to the external data constraints, the ND280 measurement provides a further constraint on some of these parameters and provides estimates of the correlations between them and with the flux

parameters.

Since Super-Kamiokande only contains oxygen as a neutrino target, only the cross section parameters that are relevant for interactions on oxygen are applicable to the bin contents of the templates. These cross section model parameters are either normalizations for individual reaction modes over all neutrino energies (i.e. apply to one or more specific templates), or have a functional response for a reaction mode as a function of true neutrino energy. Functional responses are computed for each true neutrino energy bin for a representative sample of values, and interpolated between those values with a cubic spline. In both cases, this results in a multiplicative weight for a given template and true neutrino energy bin. In Table 6.3, the parameters that are relevant to the oscillation analysis are labelled as such, and the method of calculating their effect on the oscillation analysis is also listed.

7.3.3 Detector model uncertainties, and FSI+SI

As mentioned in Section 7.1, detector systematic uncertainties are computed using a number of different control samples and comparing the difference between data and the model, which are then parametrized as efficiencies. In order to incorporate these efficiencies into the oscillation analysis, a total of 6 parameters are defined, corresponding to a normalization factor applied to bins of reconstructed energy in various templates (shown in Table 7.1). Toy simulated samples are generated with different values for the efficiency parameters, and used to calculate the covariance of the 6 parameters.

Parameter	Uncertainty
ν_μ and $\bar{\nu}_\mu$ CCQE, $E_{reco} < 0.4$ GeV	0.018
ν_μ and $\bar{\nu}_\mu$ CCQE, 0.4 GeV $\leq E_{reco} \leq$ 1.1 GeV	0.016
ν_μ and $\bar{\nu}_\mu$ CCQE, $E_{reco} >$ 1.1 GeV	0.016
ν_μ and $\bar{\nu}_\mu$ CCnonQE	0.093
ν_e and $\bar{\nu}_e$ CC	1.003
All NC	0.597

Table 7.1: The parametrization of the Super-Kamiokande detector and FSI+SI systematic parameters, including their 1σ uncertainty from their covariance matrix. The 6 parameters are defined by the templates they scale, and may be restricted to a range of reconstructed neutrino energy. From [21].

In addition, uncertainties associated with interactions of the particles produced in the neutrino interaction with the nucleus ("FSI", described in Section 2.2) and sec-

ondary interactions of the particles that have left the nucleus with detector materials ("SI", described in Section 5.4.16 as reinteractions) must be considered separately for Super-Kamiokande and ND280. This is both because the nuclear target is different (oxygen at Super-Kamiokande and carbon at ND280), and because the same model used for FSI in NEUT is also used for SI in Super-Kamiokande (instead of the Geant4 model used in ND280.) As with the detector model uncertainties, toy simulated samples were generated with different values of the FSI+SI model parameters, which were used to determine the additional uncertainty on the 6 parameters for the different modes and reconstructed energy bins. The resulting covariance matrix is added linearly to that arising from the selection criteria. The result is shown in Table 7.1. The resulting weight for these parameters is therefore a function of the mode and reconstructed energy bin, which is used to scale the corresponding templates.

There is one additional detector model uncertainty parameter that is treated differently: the energy scale uncertainty. This is a source of uncertainty stemming from differences between the reconstructed neutrino energy in the model and in data, estimated by control samples to be 2.4%. Its effect on the predicted number of events in a reconstructed neutrino energy bin in data is calculated by scaling the bin edges of the MC templates, and calculating the number of events that are gained from or lost to neighbouring bins (assuming that the events are uniformly distributed within the bins.) The content of the reconstructed energy bin it applies to is thus weighted accordingly.

7.3.4 Effect of uncertainties

The size of the uncertainties in the model spectrum can be seen by drawing sets of correlated parameters (as was done for the ND280 analysis described in Chapter 6) with which to generate toy simulated samples. If any parameter value that was drawn results in a negative number of events predicted in any reconstructed energy bin in any template, that set of parameters is rejected, and another set of parameters drawn. This procedure is used to create 100000 toy simulated experiments, from which the 1σ spread of each bin's content was calculated. The result of doing this (assuming neutrino and antineutrino oscillation with the parameters from Table 7.3) is shown in Figure 7.2, both without using the results of the ND280 measurement, and after applying the results of the ND280 measurement. The uncertainty is not significantly reduced because the model parameters that are most responsible for

the rate uncertainty are not constrained by the ND280 measurements. However, an overall increase is seen in the predicted rate. A breakdown of the contributions to the uncertainty in the predicted event rate of different types of systematic parameters is shown in Table 7.2, with the effect of the ND280 analysis noted.

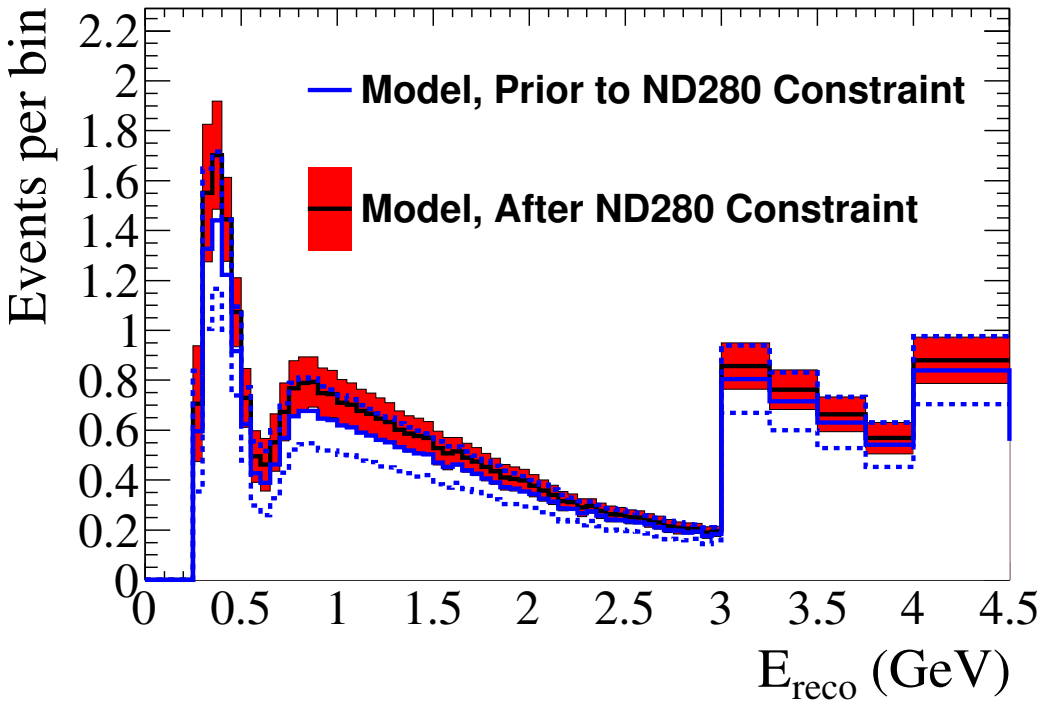

Figure 7.2: The reconstructed neutrino energy spectrum at SK under the model prior to application of the ND280 constraint, and after application of the ND280 constraint (in both cases, corresponding to 4.011×10^{20} POT). The effect of neutrino oscillations as also been applied, using the parameter values in Table 7.3. From [93] (T2K official plots associated with [21]), with modified legend.

7.4 Oscillation analysis method

As discussed in Section 2.3, the neutrino oscillation parameters of the PMNS matrix should apply to neutrinos and antineutrinos alike. Given that $\sin^2\theta_{23}$ and $|\Delta m^2|$ ($|\Delta m^2_{32}|$ for Normal Hierarchy and $|\Delta m^2_{31}|$ for Inverted Hierarchy) have been precisesly measured by T2K in neutrino beam mode [7], a measurement in antineutrino beam mode provides an opportunity to check whether this is true. As was discussed in Section 2.3, this also provides a test of the CPT Theorem. So, this analysis sets

Source of uncertainty	Uncertainty in event rate (%)	
	without ND280	with ND280
Flux and cross section (common with ND280)	9.2	3.4
Cross section (oxygen-only)	10	
Super-Kamiokande FSI + SI	2.1	
Super-Kamiokande detector	3.8	
Total	**14.4**	**11.6**

Table 7.2: Contribution of different sources of systematic uncertainty to the uncertainty in the number of events predicted at Super-Kamiokande, with the effect of the ND280 measurement shown. Table data from [94].

out to measure a separate set of antineutrino parameters, $\sin^2\bar{\theta}_{23}$ and $|\Delta\bar{m}^2|$, and uses separate parameters for neutrinos and antineutrinos for all other oscillation parameters, as shown in Table 7.3.

Parameter	NH analysis value	IH analysis value
$\sin^2\theta_{23}$	0.527	0.533
$\sin^2\bar{\theta}_{13}$ and $\sin^2\theta_{13}$	0.0248	0.0252
$\sin^2\bar{\theta}_{12}$ and $\sin^2\theta_{12}$	0.304	0.304
$\lvert\Delta m^2_{32}\rvert$	2.51×10^{-3} eV^2/c^4	–
$\lvert\Delta m^2_{31}\rvert$	–	2.48×10^{-3} eV^2/c^4
$\Delta\bar{m}^2_{21}$ and Δm^2_{21}	7.53×10^{-5} eV^2/c^4	7.53×10^{-5} eV^2/c^4
δ_{CP}	-1.55	-1.56

Table 7.3: Oscillation parameter values that are fixed, for both Normal Hierarchy (NH) and Inverted Hierarchy (IH) analyses. Their values come from an earlier T2K frequentist analysis with reactor constraint [8] where available, and otherwise from [79]. From [21].

The oscillation probabilities for each template are calculated using the three-flavour framework as described in Section 2.3, with separate oscillation parameters for neutrinos and antineutrinos, and including matter effects due to the MSW effect (described in Section 2.3.2), where a constant density of 2.6 g/cm^3 for the Earth's crust has been assumed.

The oscillation analysis is performed using a binned likelihood-ratio method, similar to that used for the ND280 analysis described in Chapter 6. The observed data and the model prediction are compared for various values of $\sin^2\bar{\theta}_{23}$ and $|\Delta\bar{m}^2|$ and the systematic parameters, including a term that considers the prior values and prior covariance of the systematic parameters. The values of the parameters that minimize

Equation 7.1 [21] are the point estimates resulting from this analysis.

$$
\begin{aligned}
&-2\ln\lambda(\sin^2\bar{\theta}_{23},\,|\Delta\bar{m}^2|;\mathbf{a}) \\
&\quad = 2\cdot\sum_{i=0}^{N-1}\left(n_i^{obs}\cdot\ln(n_i^{obs}/n_i^{exp})+(n_i^{exp}-n_i^{obs})\right)+(\mathbf{a}-\mathbf{a_0})^T\cdot\mathbf{C}^{-1}\cdot(\mathbf{a}-\mathbf{a_0}) \quad (7.1)
\end{aligned}
$$

The variables in Equation 7.1 are defined as follows:

- N is the number of reconstructed neutrino energy bins.
- $\mathbf{a}$ is a vector of the current values of the 44 systematic parameters, described in Section 7.3. It is varied during the minimization of Equation 7.1, with each of the systematic parameters restricted to the range $[-3\sigma, +3\sigma]$ about their prior value.
- $\mathbf{a_0}$ is a vector of the prior values of the systematic parameters.
- $\mathbf{C}$ is the prior covariance matrix of the systematic parameters.
- n_i^{obs} is the number of events observed in the data in reconstructed neutrino energy bin i.
- $n_i^{exp} = n_i^{exp}(\sin^2\bar{\theta}_{23},\,|\Delta\bar{m}^2|;\mathbf{a})$ is the model prediction for reconstructed energy bin i. It varies with the oscillation parameters and systematic parameters during the analysis, as described in Section 7.2.

As was the case with the similar quantity used in the ND280 analysis described in Chapter 6, $-2\ln\lambda(\sin^2\bar{\theta}_{23},\,|\Delta\bar{m}^2|;\mathbf{a})$ has a χ^2 distribution in the large sample limit, and can therefore be used as a goodness of fit test (which is discussed more in Section 7.5). Because of this, we also define Equation 7.2, and use the two notations interchangeably.

$$
\chi^2(\sin^2\bar{\theta}_{23},\,|\Delta\bar{m}^2|;\mathbf{a}) \equiv -2\ln\lambda(\sin^2\bar{\theta}_{23},\,|\Delta\bar{m}^2|;\mathbf{a}) \quad (7.2)
$$

Equation 7.1 is minimized using the Minuit [66] MIGRAD algorithm. This is done separately for each mass hierarchy. For each mass hierarchy, two initial seeds are considered. The first seed values for the oscillation parameters are $\sin^2\bar{\theta}_{23} = 0.6$ and $|\Delta\bar{m}^2| = 2.4\times10^{-3}$ eV^2/c^4. For the second seed values, the mirror point in

the other octant for the result for $\sin^2\bar{\theta}_{23}$ found using the first seed is used, and the result from the first seed is used for $|\Delta\bar{m}^2|$. After the analysis has been successfully performed, the HESSE algorithm (described in Section 6.2) is also used to improve the estimate of the uncertainties on the parameters determined by Minuit.

The uncertainties of $\sin^2\bar{\theta}_{23}$ and $|\Delta\bar{m}^2|$ are determined using the method of constant-$\Delta\chi^2$ [37] (p. 390-401). Specifically, in order to construct the 2D confidence contours, the following procedure [21] is followed.

1. Construct a 2-dimensional grid of points in $\sin^2\bar{\theta}_{23}$ and $|\Delta\bar{m}^2|$, with grid spacing $\delta(\sin^2\bar{\theta}_{23}) = 5\times10^{-3}$ and $\delta|\Delta\bar{m}^2| = 5\times10^{-5}$.

2. For each grid point, minimize Equation 7.1 with both $\sin^2\bar{\theta}_{23}$ and $|\Delta\bar{m}^2|$ fixed at their value at the grid point, but allowing all other parameters to float.

3. The 2D region bounded by the contours contains all grid points where:

$$\Delta\chi^2(\sin^2\bar{\theta}_{23},\,|\Delta\bar{m}^2|) = \chi^2(\sin^2\bar{\theta}_{23},\,|\Delta\bar{m}^2|;\mathbf{a}) - \chi^2_{min} < \Delta\chi^2_{critical} \tag{7.3}$$

   where χ^2_{min} is the minimum value of $\chi^2(\sin^2\bar{\theta}_{23},\,|\Delta\bar{m}^2|;\mathbf{a})$ obtained in the analysis, and $\Delta\chi^2_{critical}$ is 2.30 (68% CL), 4.61 (90% CL), 5.99 (95% CL), or 9.21 (99% CL).

In order to obtain 1D confidence intervals on $\sin^2\bar{\theta}_{23}$ and $|\Delta\bar{m}^2|$, a similar procedure is followed, but the value of the 2nd oscillation parameter is allowed to float along with the other nuisance parameters, and the $\Delta\chi^2_{critical}$ values are 1.00 (68% CL), 2.71 (90% CL), 3.84 (95% CL), and 6.63 (99% CL).

As was done for the ND280 analysis described in Chapter 6, this analysis was validated by performing it on the Asimov data set and additional fake data sets. The results of this analysis were also compared to those of two different analysis methods, and all three analyses were found to be consistent.

7.5 Oscillation analysis results

Using the method described in Section 7.4, the analysis was performed on the T2K antineutrino beam mode data taken in June 2014 and from November 2014-June 2015, totalling 4.011×10^{20} POT. For the analysis assuming Normal Hierarchy, the data and the best-fit model prediction are shown in Figure 7.3.

For the Normal Hierarchy analysis, the oscillation parameter values found are [21]:

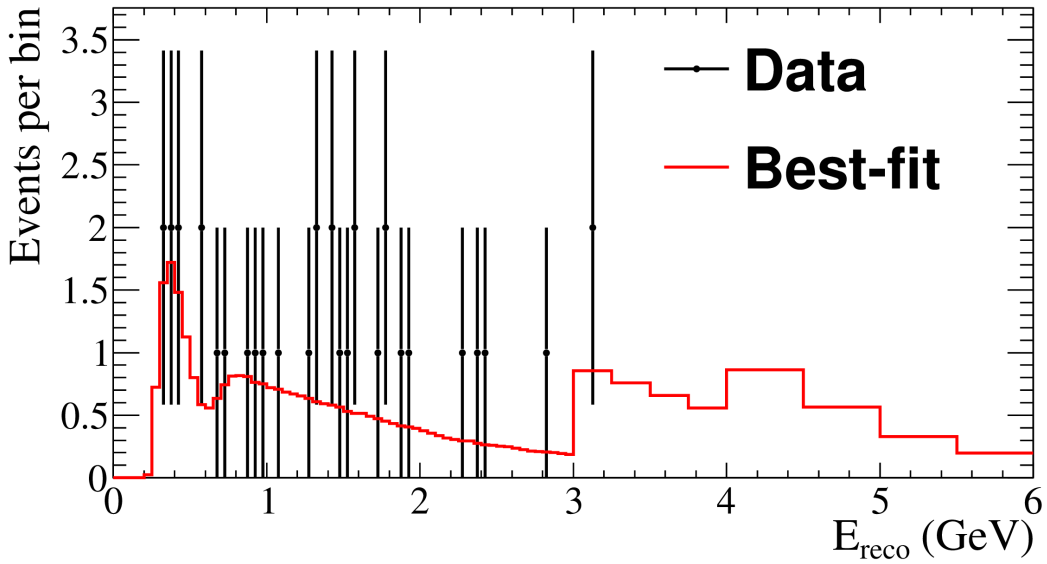

Figure 7.3: The data at Super-Kamiokande and the best-fit (NH) model prediction. From [93] (T2K official plots associated with [21]).

$\sin^2\bar{\theta}_{23} = 0.450$, with $0.327 < \sin^2\bar{\theta}_{23} < 0.692$ at the 90% confidence level and $|\Delta\bar{m}^2_{32}| = 2.518\times10^{-3}$ eV^2/c^4, with 2.03×10^{-3} eV^2/c^4 $< |\Delta\bar{m}^2_{32}| < 2.92\times10^{-3}$ eV^2/c^4 at the 90% confidence level.

For the Inverted Hierarchy analysis, the oscillation parameter values found are [21]:

$\sin^2\bar{\theta}_{23} = 0.453$, with $0.332 < \sin^2\bar{\theta}_{23} < 0.697$ at the 90% confidence level and $|\Delta\bar{m}^2_{31}| = 2.490\times10^{-3}$ eV^2/c^4, with 2.03×10^{-3} eV^2/c^4 $< |\Delta\bar{m}^2_{31}| < 2.92\times10^{-3}$ eV^2/c^4 at the 90% confidence level.

The small number of events in each reconstructed neutrino energy bin in the analysis is problematic for performing a meaningful goodness of fit test. Therefore, a coarser binning is chosen with only 5 bins (as opposed to the 73 used in the analysis.) The reconstructed energy bin boundaries are (GeV): 0.0, 0.4, 0.7, 1.0, 2.0, 30.0.

Then, using the parameter values found in the analysis to make a model prediction with this new binning, $\chi^2(\sin^2\bar{\theta}_{23}, |\Delta\bar{m}^2|; \mathbf{a})$ is calculated. Finally, 1000 toy experiments are generated for both mass hierarchies, fixing the oscillation parameters at their best fit values, but choosing different values of all 44 systematic parameters according to their prior covariance, along with statistical variations. The analysis is then performed on each of the toy experiments, and the resulting values of $\chi^2(\sin^2\bar{\theta}_{23}, |\Delta\bar{m}^2|; \mathbf{a})$ for each toy make up a χ^2 distribution used to determine the goodness of fit by counting the fraction of toys with χ^2 greater than that of the

analysis of the data. The resulting p-values [21] are 0.34 (NH) and 0.38 (IH), which are acceptable. For Normal Hierarchy, the best-fit model prediction in this coarser binning is shown with the observed data in Figure 7.4. Also included is the model prediction in the absence of oscillations, demonstrating the large deficit of muon antineutrinos that is the characteristic of muon antineutrino disappearance.

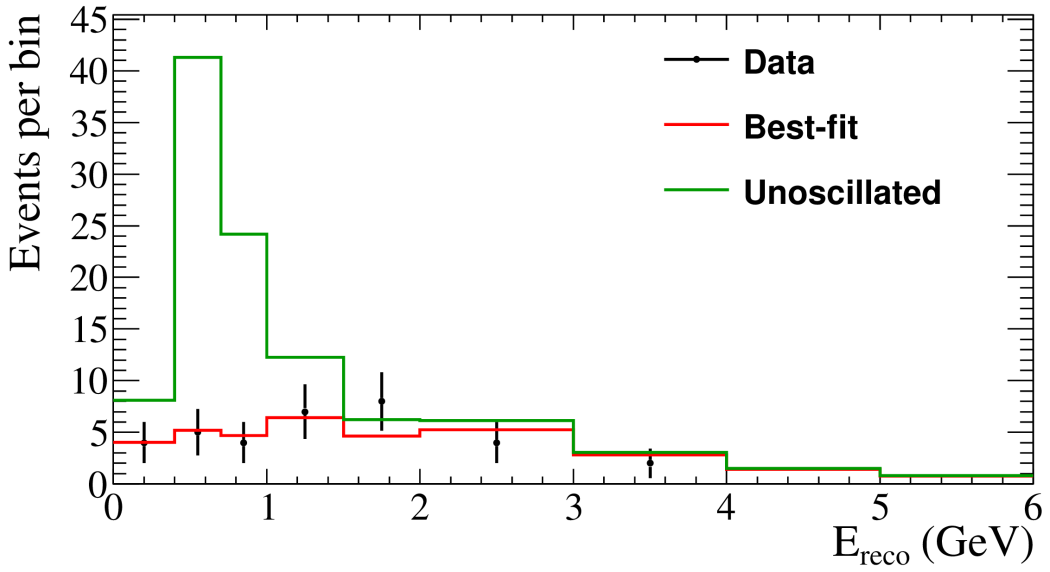

Figure 7.4: The Super-Kamiokande data shown with the best-fit (NH) model prediction, and the model prediction in the absence of neutrino oscillations. The coarser binning of the goodness of fit test is used. From [93] (T2K official plots associated with [21]).

As discussed in Section 7.4, 2D confidence regions can be constructed. A number of comparisons can be made with them. In Figure 7.5, two sets of contours are generated: one with statistical uncertainties alone (i.e. the systematic parameters are fixed at their best-fit value), and one with statistical and systematic uncertainties (both for Normal Hierarchy). The lack of significant difference between the two contours suggests that this analysis is statistics limited (which is to say, more data is required before any reduction of the systematic uncertainties would result in significantly decreasing the size of these contours).

In Figure 7.6, this result (NH and IH) is compared to that from the MINOS experiment [11]. The shape of the MINOS contour and the two best-fit points shown are due to the MINOS result being reported in $\sin^2(2\bar{\theta}_{23})$, which has thus been converted to $\sin^2\bar{\theta}_{23}$ to be shown with the T2K result. The T2K result is consistent with the

MINOS result, and provides a tighter constraint on $\sin^2\bar{\theta}_{23}$.

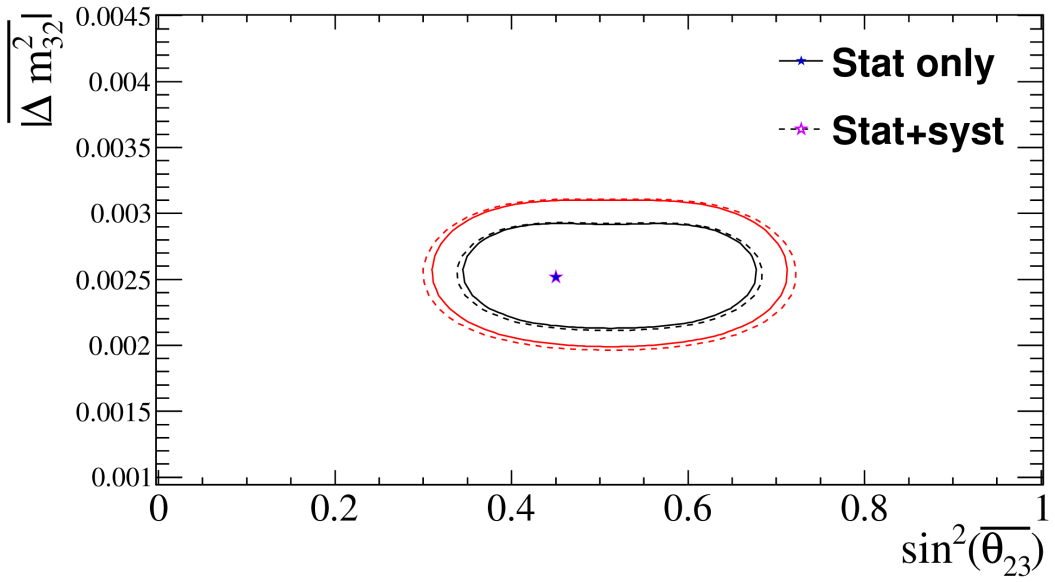

Figure 7.5: Confidence regions generated from the (NH) analysis result (Stat+syst), and using the result but without varying the systematic uncertainties (Stat only). The 68% confidence regions are in black, and the 90% confidence regions are in red. From [93] (T2K official plots associated with [21]).

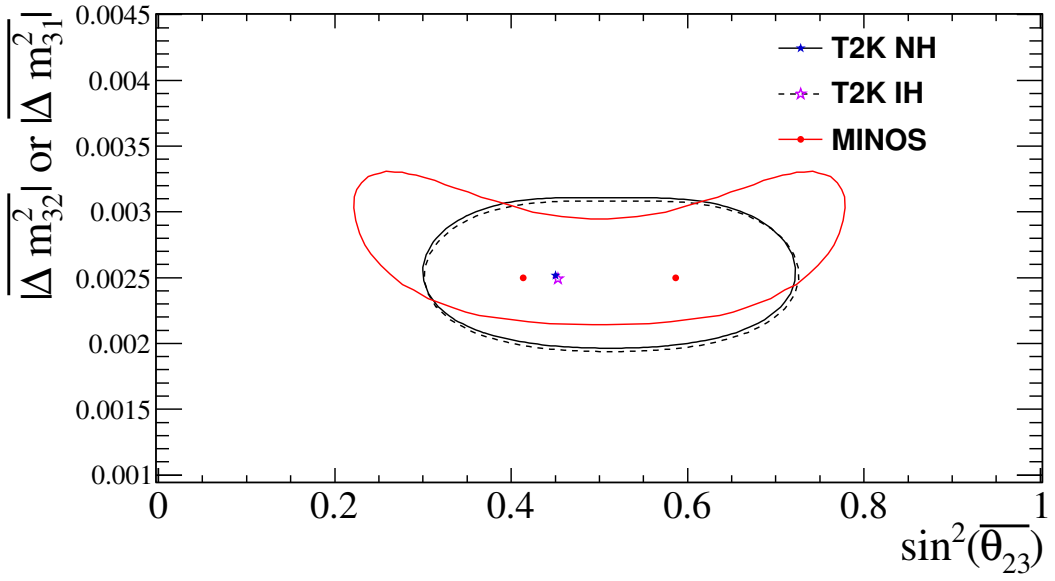

Figure 7.6: The 90% confidence regions generated from the analysis result (NH and IH) compared to the result from MINOS. From [93] (T2K official plots associated with [21]), with modified colour scheme.

Finally, the T2K muon antineutrino disappearance result is compared to the previous T2K muon disappearance result [7] in Figure 7.7 (both Normal Hierarchy). Both results are consistent with each other, as is the expectation from neutrino oscillation theory, and is consistent with the combined CPT symmetry being conserved.

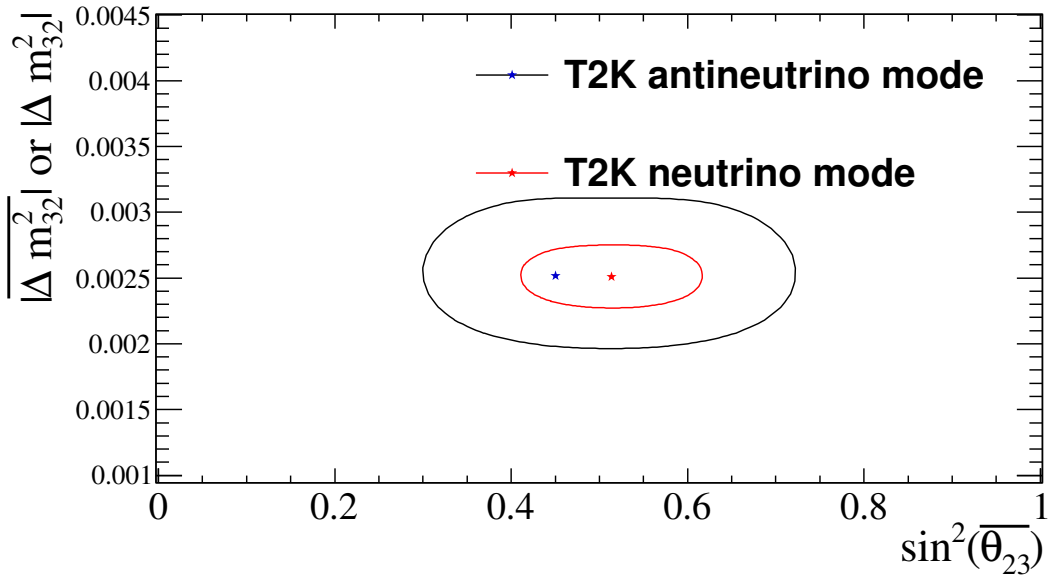

Figure 7.7: The 90% confidence regions generated from the analysis result (NH, muon antineutrino disappearance in antineutrino mode) compared to those from the earlier T2K muon neutrino disappearance analysis in neutrino mode. From [93] (T2K official plots associated with [21]), with modified colour scheme.

Chapter 8

Conclusions

A measurement of muon antineutrino disappearance has been made. Under the assumption of Normal Hierarchy, this analysis determined oscillation parameter values of

$$\sin^2(\bar{\theta}_{23}) = 0.450 \tag{8.1}$$

$$|\Delta\bar{m}^2_{32}| = 2.518 \times 10^{-3}\ \mathrm{eV}^2/\mathrm{c}^4 \tag{8.2}$$

with 90% 1D confidence intervals

$$0.327 < \sin^2(\bar{\theta}_{23}) < 0.692 \tag{8.3}$$

$$2.03 \times 10^{-3}\ \mathrm{eV}^2/\mathrm{c}^4 < |\Delta\bar{m}^2_{32}| < 2.92 \times 10^{-3}\ \mathrm{eV}^2/\mathrm{c}^4 \tag{8.4}$$

Under the assumption of Inverted Hierarchy, this analysis determined oscillation parameter values of

$$\sin^2(\bar{\theta}_{23}) = 0.453 \tag{8.5}$$

$$|\Delta\bar{m}^2_{31}| = 2.490 \times 10^{-3}\ \mathrm{eV}^2/\mathrm{c}^4 \tag{8.6}$$

with 90% 1D confidence intervals

$$0.332 < \sin^2(\bar{\theta}_{23}) < 0.697 \tag{8.7}$$

$$2.03 \times 10^{-3}\ \mathrm{eV}^2/\mathrm{c}^4 < |\Delta\bar{m}^2_{31}| < 2.92 \times 10^{-3}\ \mathrm{eV}^2/\mathrm{c}^4 \tag{8.8}$$

These results are consistent with the previous MINOS measurement of muon an-

tineutrino oscillation. In addition, they are consistent with the previous T2K measurement of muon neutrino disappearance, and therefore with conservation of CPT symmetry.

This measurement was performed by analyzing $\bar{\nu}_\mu$ Super-Kamiokande data from the T2K antineutrino beam mode running periods. T2K models for the neutrino beam flux and neutrino interaction cross sections played an important role in this measurement. Some of these model parameters were measured in a separate analysis of ND280 ν_μ and $\bar{\nu}_\mu$ data from both neutrino and antineutrino beam modes, and the results used as an input to the oscillation analysis.

Future ND280 analyses making use of more subdetectors (in particular those containing water) will be more sensitive to cross section model parameters used at Super-Kamiokande in the oscillation analysis. In combination with more antineutrino beam mode data, the uncertainty on future antineutrino oscillation parameter measurements will be significantly reduced.

Bibliography

[1] A. I. Abazov et al. Search for Neutrinos from the Sun Using the Reaction ^{71}Ga(ν_e,e^-)^{71}Ge. *Phys. Rev. Lett.*, 67:3332–3335, 1991.

[2] K. Abe et al. (T2K Collaboration). Indication of Electron Neutrino Appearance from an Accelerator-produced Off-axis Muon Neutrino Beam. *Phys. Rev. Lett.*, 107:041801, 2011.

[3] K. Abe et al. (T2K Collaboration). The T2K Experiment. *Nucl. Instrum. Meth.*, A659:106–135, 2011.

[4] K. Abe et al. (T2K Collaboration). Evidence of Electron Neutrino Appearance in a Muon Neutrino Beam. *Phys. Rev.*, D88(3):032002, 2013.

[5] K. Abe et al. (T2K Collaboration). Measurement of Neutrino Oscillation Parameters from Muon Neutrino Disappearance with an Off-axis Beam. *Phys.Rev.Lett.*, 111(21):211803, 2013.

[6] K. Abe et al. (T2K Collaboration). T2K neutrino flux prediction. *Phys. Rev.*, D87(1):012001, 2013. [Addendum: Phys. Rev.D87,no.1,019902(2013)].

[7] K. Abe et al. (T2K Collaboration). Precise Measurement of the Neutrino Mixing Parameter θ_{23} from Muon Neutrino Disappearance in an Off-Axis Beam. *Phys.Rev.Lett.*, 112(18):181801, 2014.

[8] K. Abe et al. (T2K Collaboration). Measurements of neutrino oscillation in appearance and disappearance channels by the T2K experiment with 6.6×10^{20} protons on target. *Phys. Rev.*, D91(7):072010, 2015.

[9] Y. Abe et al. (Double Chooz Collaboration). Reactor electron antineutrino disappearance in the Double Chooz experiment. *Phys. Rev.*, D86:052008, 2012.

[10] N. Abgrall et al. (T2K ND280 TPC Collaboration). Time Projection Chambers for the T2K Near Detectors. *Nucl. Instrum. Meth.*, A637:25–46, 2011.

[11] P. Adamson et al. (MINOS Collaboration). Measurement of Neutrino and Antineutrino Oscillations Using Beam and Atmospheric Data in MINOS. *Phys. Rev. Lett.*, 110:251801, Jun 2013.

[12] S. Agostinelli et al. (GEANT4 Collaboration). GEANT4: A Simulation toolkit. *Nucl. Instrum. Meth.*, A506:250–303, 2003.

[13] A. A. Aguilar-Arevalo et al. (MiniBooNE Collaboration). First Measurement of the Muon Neutrino Charged Current Quasielastic Double Differential Cross Section. *Phys. Rev.*, D81:092005, 2010.

[14] A. A. Aguilar-Arevalo et al. (MiniBooNE Collaboration). First Measurement of the Muon Anti-Neutrino Double-Differential Charged Current Quasi-Elastic Cross Section. *Phys. Rev.*, D88:032001, 2013.

[15] Q. R. Ahmad et al. (SNO Collaboration). Measurement of the rate of $\nu_e + d \rightarrow p + p + e^-$ interactions produced by ^8B solar neutrinos at the Sudbury Neutrino Observatory. *Phys. Rev. Lett.*, 87:071301, 2001.

[16] Q. R. Ahmad et al. (SNO Collaboration). Direct evidence for neutrino flavor transformation from neutral current interactions in the Sudbury Neutrino Observatory. *Phys. Rev. Lett.*, 89:011301, 2002.

[17] M. Ahmadi et al. An improved limit on the charge of antihydrogen from stochastic acceleration. *Nature*, 529(7586):373–376, 2016.

[18] J. K. Ahn et al. (RENO Collaboration). Observation of Reactor Electron Antineutrino Disappearance in the RENO Experiment. *Phys. Rev. Lett.*, 108:191802, 2012.

[19] Edoardo Amaldi. From the discovery of the neutron to the discovery of nuclear fission. *Physics Reports*, 111(1–4):1 – 331, 1984.

[20] F. P. An et al. (Daya Bay Collaboration). Observation of electron-antineutrino disappearance at Daya Bay. *Phys. Rev. Lett.*, 108:171803, 2012.

[21] C. Andreopoulos et al. T2K 4.011×10^{20}-POT 3-Flavour Muon-Antineutrino Disappearance Analysis. Technical Report T2K-TN-243, version 5.0, T2K, 2015.

[22] P. Anselmann et al. (GALLEX Collaboration). Solar neutrinos observed by GALLEX at Gran Sasso. *Phys. Lett.*, B285:376–389, 1992.

[23] S. Anvar et al. Large bulk Micromegas detectors for TPC applications. *Nucl. Instrum. Meth.*, A602:415–420, 2009.

[24] M. Apollonio et al. (CHOOZ Collaboration). Search for neutrino oscillations on a long baseline at the CHOOZ nuclear power station. *Eur. Phys. J.*, C27:331–374, 2003.

[25] D. Ashery, I. Navon, G. Azuelos, H. K. Walter, H. J. Pfeiffer, and F. W. Schleputz. True Absorption and Scattering of Pions on Nuclei. *Phys. Rev.*, C23:2173–2185, 1981.

[26] Isaac Asimov. *Robot Dreams*. Masterworks of Science Fiction and Fantasy. The Berkley Publishing Group, Second Ace trade paperback edition, June 2004.

[27] B. Aubert et al. (BABAR Collaboration). Search for CPT and Lorentz Violation in B^0-$\overline{B}^0$ Oscillations with Dilepton Events. *Phys. Rev. Lett.*, 100:131802, Apr 2008.

[28] G. Backenstoss, B. D. Hyams, G. Knop, P. C. Marin, and U. Stierlin. Helicity of μ^- mesons from π-meson decay. *Phys. Rev. Lett.*, 6:415–416, Apr 1961.

[29] John N. Bahcall, Neta A. Bahcall, and Giora Shaviv. Present status of the theoretical predictions for the ^{37}Cl solar-neutrino experiment. *Phys. Rev. Lett.*, 20:1209–1212, May 1968.

[30] John N. Bahcall and Plamen I. Krastev. Do hep neutrinos affect the solar neutrino energy spectrum? *Physics Letters B*, 436(3–4):243 – 250, 1998.

[31] Marcel Bardon, Paolo Franzini, and Juliet Lee. Helicity of μ^- Mesons; Mott Scattering of Polarized Muons. *Phys. Rev. Lett.*, 7:23–25, Jul 1961.

[32] P. Bartet et al. ν_μ CC event selections in the ND280 tracker using Run 2+3+4 data. Technical Report T2K-TN-212, version 1.0, T2K, 2015.

[33] G. Battistoni, F. Cerutti, A. Fassò, A. Ferrari, S. Muraro, J. Ranft, S. Roesler, and P. R. Sala. The FLUKA code: description and benchmarking. *AIP Conference Proceedings*, 896(1):31–49, 2007.

[34] Sheldon Bennett, David Nygren, Harry Saal, Jack Steinberger, and John Sunderland. Measurement of the charge asymmetry in the decay ${K_L}^0 \to \pi^{\pm} + e^{\mp} + \nu$. *Phys. Rev. Lett.*, 19:993–997, Oct 1967.

[35] V. Berardi et al. CC $\bar{\nu}_{\mu}$ event selection in the ND280 tracker using Run 5c antineutrino beam data. Technical Report T2K-TN-224, version 5.2, T2K, 2015.

[36] V. Berardi et al. ND280 Tracker analysis of ν_{μ} Contamination In AntiNu Beam in Run5c data. Technical Report T2K-TN-227, version 3.8, T2K, 2015.

[37] J. Beringer et al. (Particle Data Group Collaboration). Review of Particle Physics (RPP). *Phys. Rev.*, D86:010001, 2012.

[38] S. Bhadra et al. Optical Transition Radiation Monitor for the T2K Experiment. *Nucl. Instrum. Meth.*, A703:45–58, 2013.

[39] J. Bouchez et al. Bulk micromegas detectors for large TPC applications. *Nucl. Instrum. Meth.*, A574:425–432, 2007.

[40] G. C. Branco, R. Gonzalez Felipe, and F. R. Joaquim. Leptonic CP Violation. *Rev. Mod. Phys.*, 84:515–565, 2012.

[41] R. Brun and F. Rademakers. ROOT: An object oriented data analysis framework. *Nucl. Instrum. Meth.*, A389:81–86, 1997.

[42] René Brun, F. Bruyant, Federico Carminati, Simone Giani, M. Maire, A. McPherson, G. Patrick, and L. Urban. GEANT Detector Description and Simulation Tool. *Report No. CERN-W5013*, 1994.

[43] T.T. Böhlen, F. Cerutti, M.P.W. Chin, A. Fassò, A. Ferrari, P.G. Ortega, A. Mairani, P.R. Sala, G. Smirnov, and V. Vlachoudis. The FLUKA Code: Developments and Challenges for High Energy and Medical Applications. *Nuclear Data Sheets*, 120:211 – 214, 2014.

[44] B. T. Cleveland, Timothy Daily, Raymond Davis, Jr., James R. Distel, Kenneth Lande, C. K. Lee, Paul S. Wildenhain, and Jack Ullman. Measurement of the

solar electron neutrino flux with the Homestake chlorine detector. *Astrophys. J.*, 496:505–526, 1998.

[45] Hamamatsu Photonics K.K. Editorial Committee. *PHOTOMULTIPLIER TUBES*. Hamamatsu Photonics K.K. Electron Tube Division, 3a edition, August 2007.

[46] C. L. Cowan, F. Reines, F. B. Harrison, H. W. Kruse, and A. D. McGuire. Detection of the Free Neutrino: a Confirmation. *Science*, 124(3212):103–104, 1956.

[47] Glen Cowan. *Statistical Data Analysis*. Oxford University Press, Oxford, 1998 (reprinted 2004).

[48] Glen Cowan, Kyle Cranmer, Eilam Gross, and Ofer Vitells. Asymptotic formulae for likelihood-based tests of new physics. *Eur. Phys. J.*, C71:1554, 2011. [Erratum: Eur. Phys. J.C73,2501(2013)].

[49] G. Danby, J-M. Gaillard, K. Goulianos, L. M. Lederman, N. Mistry, M. Schwartz, and J. Steinberger. Observation of high-energy neutrino reactions and the existence of two kinds of neutrinos. *Phys. Rev. Lett.*, 9:36–44, Jul 1962.

[50] Raymond Davis, Don S. Harmer, and Kenneth C. Hoffman. Search for neutrinos from the sun. *Phys. Rev. Lett.*, 20:1205–1209, May 1968.

[51] Patrick de Perio. NEUT pion FSI. *AIP Conf. Proc.*, 1405:223–228, 2011.

[52] A. Ferrari, P. R. Sala, A. Fasso, and J. Ranft. FLUKA: A multi-particle transport code, Report Nos. CERN-2005-010, SLAC-R-773, INFN-TC-05-11. 2005.

[53] L. Fields et al. (MINERvA Collaboration). Measurement of Muon Antineutrino Quasi-Elastic Scattering on a Hydrocarbon Target at $E_\nu \sim 3.5$ GeV. *Phys. Rev. Lett.*, 111:022501, 2013.

[54] G.A. Fiorentini et al. (MINERvA Collaboration). Measurement of Muon Neutrino Quasi-Elastic Scattering on a Hydrocarbon Target at $E_\nu \sim 3.5$ GeV. *Phys. Rev. Lett.*, 111:022502, 2013.

[55] Martin Freund. Analytic approximations for three neutrino oscillation parameters and probabilities in matter. *Phys. Rev.*, D64:053003, 2001.

[56] Y. Fukuda et al. (Super-Kamiokande Collaboration). Evidence for oscillation of atmospheric neutrinos. *Phys. Rev. Lett.*, 81:1562–1567, 1998.

[57] Y. Fukuda et al. (Super-Kamiokande Collaboration). The Super-Kamiokande detector. *Nucl. Instrum. Meth.*, A501:418–462, 2003.

[58] M. Gell-Mann. The interpretation of the new particles as displaced charge multiplets. *Il Nuovo Cimento (1955-1965)*, 4(2):848–866, 1956.

[59] R. A. Giannelli et al. Multiproton final states in positive pion absorption below the Delta (1232) resonance. *Phys. Rev.*, C61:054615, 2000.

[60] David J. Griffiths. *INTRODUCTION TO ELEMENTARY PARTICLES*. John Wiley & Sons, Inc., 1987.

[61] M. Hartz et al. Constraining the Flux and Cross Section Models with Data from the ND280 Detector for the 2014/15 Oscillation Analysis. Technical Report T2K-TN-220, version 4.0, T2K, 2015.

[62] Yoshinari Hayato. A neutrino interaction simulation program library NEUT. *Acta Phys. Polon.*, B40:2477–2489, 2009.

[63] Aatos Heikkinen, Nikita Stepanov, and Johannes Peter Wellisch. Bertini intranuclear cascade implementation in GEANT4. *eConf*, C0303241:MOMT008, 2003.

[64] K. S. Hirata et al. (Kamiokande-II Collaboration). Results from one thousand days of real time directional solar neutrino data. *Phys. Rev. Lett.*, 65:1297–1300, 1990.

[65] K. S. Hirata et al. (Kamiokande-II Collaboration). Observation of a small atmospheric muon-neutrino / electron-neutrino ratio in Kamiokande. *Phys. Lett.*, B280:146–152, 1992.

[66] F. James and M. Roos. Minuit: A System for Function Minimization and Analysis of the Parameter Errors and Correlations. *Comput. Phys. Commun.*, 10:343–367, 1975.

[67] Nick Jelley, Arthur B. McDonald, and R. G. Hamish Robertson. The Sudbury Neutrino Observatory. *Ann. Rev. Nucl. Part. Sci.*, 59:431–465, 2009.

[68] M. K. Jones et al. Pion absorption above the Delta (1232) resonance. *Phys. Rev.*, C48:2800–2817, 1993.

[69] Edward Kearns. Experimental measurements of atmospheric neutrinos. *Nucl. Phys. Proc. Suppl.*, 70:315–323, 1999.

[70] K. Kodama et al. (DONUT Collaboration). Observation of tau neutrino interactions. *Phys. Lett.*, B504:218–224, 2001.

[71] E. J. Konopinski and H. M. Mahmoud. The Universal Fermi Interaction. *Phys. Rev.*, 92:1045–1049, Nov 1953.

[72] Emil Jan Konopinski. Beta-Decay. *Rev. Mod. Phys.*, 15:209–245, Oct 1943.

[73] Sacha E. Kopp. Accelerator-based neutrino beams. *Phys. Rept.*, 439:101–159, 2007.

[74] Chris Loken, Daniel Gruner, Leslie Groer, Richard Peltier, Neil Bunn, Michael Craig, Teresa Henriques, Jillian Dempsey, Ching-Hsing Yu, Joseph Chen, L Jonathan Dursi, Jason Chong, Scott Northrup, Jaime Pinto, Neil Knecht, and Ramses Van Zon. Scinet: Lessons learned from building a power-efficient top-20 system and data centre. *Journal of Physics: Conference Series*, 256(1):012026, 2010.

[75] Z. Maki, M. Nakagawa, and S. Sakata. Remarks on the unified model of elementary particles. *Prog. Theor. Phys.*, 28:870, 1962.

[76] S. P. Mikheyev and A. Yu. Smirnov. Resonance Amplification of Oscillations in Matter and Spectroscopy of Solar Neutrinos. *Sov. J. Nucl. Phys.*, 42:913–917, 1985. [Yad. Fiz.42,1441(1985)].

[77] S. P. Mikheyev and A. Yu. Smirnov. Resonant amplification of neutrino oscillations in matter and solar neutrino spectroscopy. *Nuovo Cim.*, C9:17–26, 1986.

[78] I. Navon, D. Ashery, J. Alster, G. Azuelos, B. M. Barnett, W. Gyles, R. R. Johnson, D. R. Gill, and T. G. Masterson. True Absorption and Scattering of 50-MeV Pions. *Phys. Rev.*, C28:2548, 1983.

[79] K. A. Olive et al. (Particle Data Group Collaboration). Review of Particle Physics. *Chin. Phys.*, C38:090001, 2014.

[80] Martin L. Perl et al. Evidence for Anomalous Lepton Production in $e^+ - e^-$ Annihilation. *Phys. Rev. Lett.*, 35:1489–1492, 1975.

[81] B. Pontecorvo. Neutrino experiments and the question of leptonic-charge conservation. *Sov. Phys. JETP*, 26:984–988, 1968.

[82] C.R. Praharaj. *Contemporary Nuclear Physics*. Taylor & Francis Group, 2003.

[83] J.E. Purcell and C.G. Sheu. Nuclear Data Sheets for A = 3. *Nuclear Data Sheets*, 130:1 – 20, 2015.

[84] R. D. Ransome et al. Pion absorption in heavy nuclei. *Phys. Rev.*, C45:509–513, 1992.

[85] F. Reines. The neutrino: from poltergeist to particle. *Rev. Mod. Phys.*, 68:317–327, Apr 1996.

[86] Frederick Reines and Clyde L. Cowan. The neutrino. *Nature*, 178:446–449, 1956.

[87] D. Rowntree et al. (LADS Collaboration). π^+ absorption on N and Ar. *Phys. Rev.*, C60:054610, 1999.

[88] Gregory F. Strouse. Standard Reference Material 1751: Gallium Melting-Point Standard. *National Institute of Standards and Technology Special Publication 260-157*, August 2004.

[89] T2K Collaboration official plots collection. General plots/Beam, 2014.

[90] T2K Collaboration official plots collection. T2K-PLOT-033: Analyses for Run5-6 antinu data/ND280 anti-NuMu measurement/ND280 anti-NuMu run5c plots, 2015.

[91] T2K Collaboration official plots collection. T2K-PLOT-033: Analyses for Run5-6 antinu data/ND280 NuMu Bkg in anti-nu beam measurement/ND280 NuMu Bkg in anti-nu beam plots without NIWG Tuning, 2015.

[92] T2K Collaboration official plots collection. T2K-PLOT-033: Analyses for Run5-6 antinu data/ND280 NuMu plots (TN-212), 2015.

[93] T2K Collaboration official plots collection. T2K-PLOT-033: Analyses for Run5-6 antinu data/numubar disappearance results with full Run5-6 data/VALOR Plots, 2015.

[94] T2K Collaboration official plots collection. T2K-PLOT-033: Analyses for Run5-6 antinu data/Table of systematics error size on the number of (anti-)numu and (anti-)nue sample, 2015.

[95] Callum Wilkinson, Philip Rodrigues, Susan Cartwright, Lee Thompson, and Kevin McFarland. Reanalysis of bubble chamber measurements of muon-neutrino induced single pion production. *Phys. Rev.*, D90(11):112017, 2014.

[96] L. Wolfenstein. Neutrino Oscillations in Matter. *Phys. Rev.*, D17:2369–2374, 1978.

[97] Y. Yamazaki, K. Hasegawa, M. Ikegami, Y. Irie, T. Kato, H. Kobayashi, S. Machida, Y. Mori, F. Noda, H. Suzuki, et al. Accelerator technical design report for J-PARC. 2003. Report Nos. KEK-REPORT-2002-13, JAERI-TECH-2003-044, J-PARC-03-01.

[98] C. Zeitnitz and T. A. Gabriel. In *Proceedings of International Conference on Calorimetry in High Energy Physics, Tallahassee, FL, USA, February 1993.* (World Scientific, Singapore, 2014).